Micromegas Vertex Tracker Feasibility

Saclay May 2009

S. Aune, D. Calvet, M. Combet, E. Delagnes, C. Lahonde-Hamdoun, S. Lhenoret, O. Meunier
SEDI/Irfu CEA Saclay

J. Ball, M. El Yakoubi, P. Konczykowski, S. Procureur, F. Sabatié
SPhN/Irfu CEA Saclay

S. Cazaux, P. Daniel-Thomas, A. Mohamed
SIS/Irfu CEA Saclay

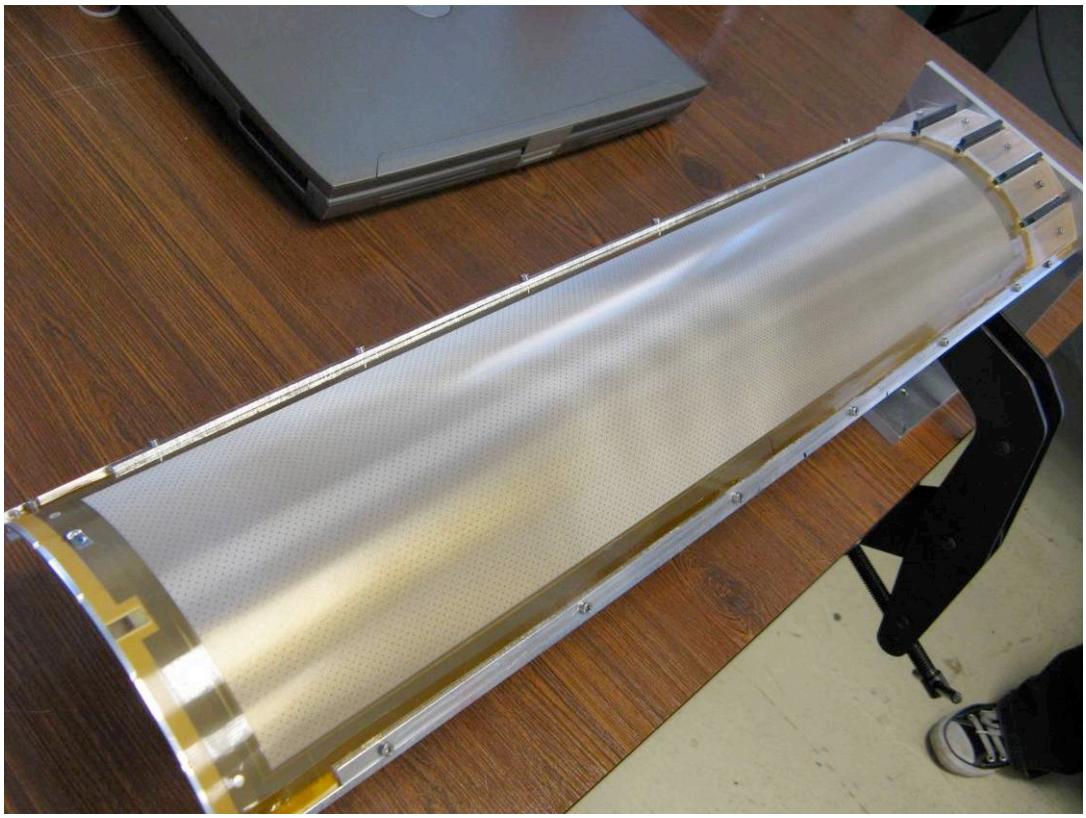

Figure 0-1: 600 mm long micromegas bulk curved prototype

Table of contents

Introduction

Jefferson Lab future upgrade in energy from 6 to12 GeV has initiated different projects concerning the Halls equipment as they should fit the new requirements of the higher energy range. In Hall B, the Cebaf Large Acceptance Spectrometer (CLAS) [1], designed to study multi-particle, exclusive reactions, will be upgraded to CLAS12, a new version of the spectrometer, optimized to study high-energy exclusive and semi-inclusive reactions and able to deal with higher momentum tracks and smaller cross-sections. It should be able to cope with a luminosity of $L = 10^{35}cm^{-2}\ s^{-1}$ and have a good vertex resolution.CLAS12 [2] is composed of a Forward Detector covering the 5 - 40° angular range and a Central Detector covering 35 -125°.
The Central Detector is confined inside the warm bore of a 5 T solenoid around the target and consists in addition to the solenoid of a Central Tracker, Central Time of Flight and possibly a neutron counter. The Central tracker has to occupy a cylindrical volume, 600 mm in length with a minimal radius of 50 mm and a maximal radius of 240 mm. It is completed with a Forward Central Tracker at the outlet of the solenoid and covering the 5 - 40° angular range.

In 2006, the Saclay group expressed interest in getting involved in CLAS12. Previous experiences with Micromegas detectors used in high energy experiments like COMPASS at CERN, plus the newly found "bulk" Micromegas concept, developed for T2K, made it possible to consider using this type of detectors in the Central Tracker part of CLAS12. The bulk Micromegas (MM) being flexible could be mounted on cylindrical tiles around the target, in double layers (X and Y coordinates).

Initial simulations hinted that the best compromise was to use a mixed solution of Silicon detectors plus Micromegas as displayed in Table 1 for 0.6 GeV/c pions and $\theta = 90°$.

	4x2 MM	**4x2 Si**	**2x2 Si + 3x2 MM**	**Requirements**
Momentum resolution dp/p (%)	2.9	2.1	1.6	5
θ resolution (mrad)	1.3	15.1	1.4	10
φ resolution (mrad)	10.9	2.9	2.6	5
Spatial resolution (μm)	212	1522	267	n/a

Table 1 : Simulation predictions for different Central Trackers options

The considered design consists in 3 double layers (X and Y) of 3 cylindrical MM tile detectors with cylinder radii ranging from 110 to 240 mm for the central "barrel" part and 3 double layers divided in 6 disk sectors for the forward part. This corresponds to about 30,000 electronics channels.

After having recalled what are Micromegas and bulk Micromegas, the section 2 will display the design for the tracker and its different components. Characterization process of the

detectors and simulation predictions with Garfield will follow in section 3 and 4. One of the main issues we had to explore was the behaviour of the MM in a harsh magnetic environment. The second part of this report will depict the tests which were performed on prototypes in magnetic field and their results as well as tests using cosmic rays to measure spatial resolution and efficiency in sections 5 and 6.
Tracking simulations are shown in section 7 and some design for the dedicated electronics are discussed in section 8. The foreseen schedule and resources needed for production close this report.

1. Micromegas Detectors

1.1. Principles

A Micromegas [3] (MICROMEsh GAseous Structure) is a gaseous detector based on a parallel plate electrode structure and a set of micro-strips for readout, see Fig.1.1. The presence of a mesh between the strips and the drift electrode allows for separating the conversion gap, where particles create primary electrons by interacting with the gas, from the amplification gap, where the primary electrons will create an avalanche in the presence of a high electric field. If this field is high enough compared to the field in the conversion gap, the micromesh is transparent for the electrons, but not for the ions coming from the avalanche.

This special feature allows a very fast collection of the ions created in the amplification gap (around 100 ns, compared to several microseconds for a drift chamber). For this reason, Micromegas detectors have a very high-rate capability. It has been used, in particular, in the COMPASS experiment at CERN, where the 12 40x40 cm² layers are installed downstream of the target, and detect particles with an efficiency larger than 95%, in spite of a 30 MHz rate (mainly concentrated on a few centimeters around the beam) [4].

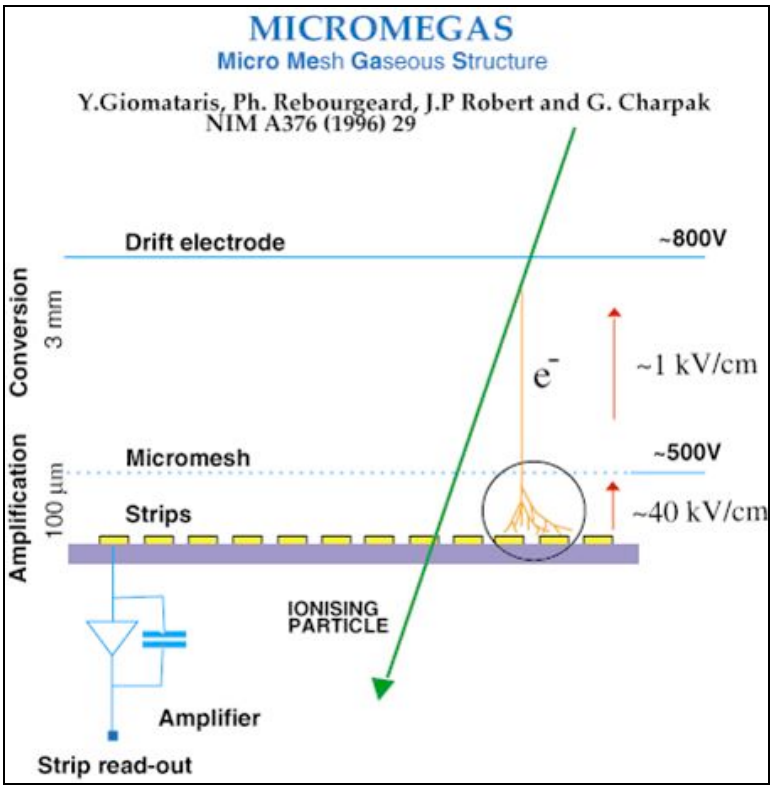

Figure 1-1 : Principle of the Micromegas detector. An incident particle ionizes the gas in the conversion region, and the resulting electrons drift down to the mesh and produce avalanches in the amplification region. The mesh allows a very fast collection of the ions created in the avalanche.

1.2. The “bulk” micromegas detector

A new detector has been developed by a collaboration between CERN/TS-DEM and IRFU (CEA-Saclay), which is an upgrade of the standard Micromegas: the “bulk” Micromegas [5]. The principle of bulk MM is to embed a metallic woven mesh on a PCB. For CLAS12, the foreseen detectors will use thin PCB boards (100 µm) with 5 µm thick copper strips, typically 300 µm wide, as the anode plane. A photo-resistive film having the right thickness, and the 18 µm thick, 403 lines per inch (LPI), stainless steel woven mesh cathode are then laminated together with the board at high temperature, forming a single object. By photolithographic method the photo resistive material is etched producing the pillars in which the mesh is embedded. The whole detector is nearly built in one process as the drift plane has eventually to be glued above the mesh to determine the conversion gap.

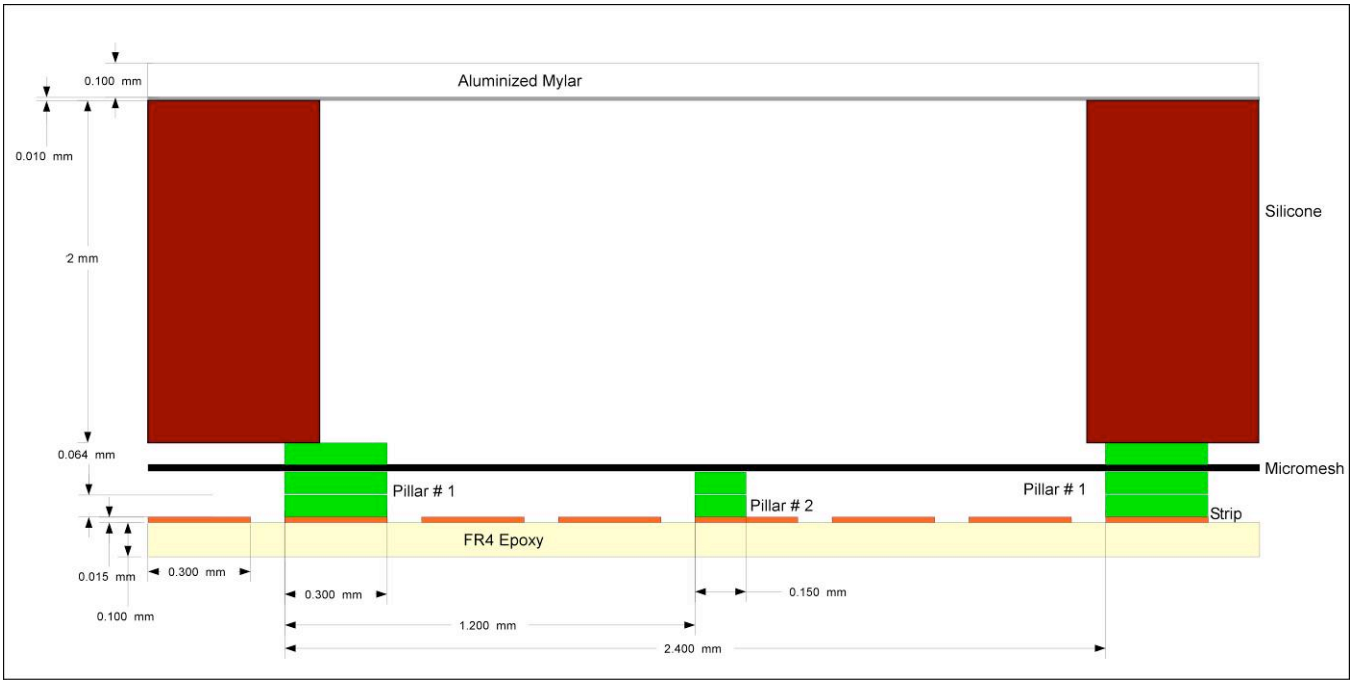

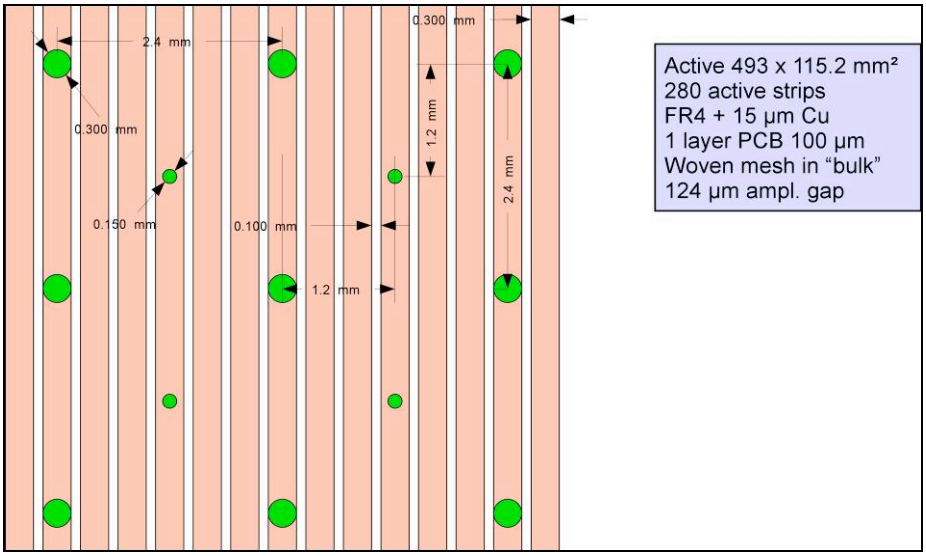

Figure 1-2 : Bulk Micromegas, from top section, details of the strips plane.

The micromesh is encapsulated inside 3 layers of Coverlay. In order to keep the distance between the micromesh and the strips constant when the detector is curved, some little pillars are placed between the thick ones. For a design like the one presented in Figure 1-2, the fraction of active area covered by the pillars is around 3 %.This area is not a dead zone as the electrons are collected by the neighbor strips, even though it may be locally less efficient.

1.2.1. The cathode and the drift space

The detector is designed in a way to reduce the transverse drift of the electrons in the conversion gap. Therefore, the drift space is 2 mm wide, delimited by a 2 mm thick silicon joint which provides also the gas tightness. The drift electrode is an aluminized Mylar polyester PET (Poly Ethylene Terephtalate) film (100 µm of Mylar for 400 nm of aluminum).

1.2.2. The anode PCB

The Micromegas detector is built on a Printed Circuit Board (PCB) which acts as the anode. It routes the electrical signal from the strips to the connectors and brings the first mechanical rigidity to the detector.
Our design is based on previous experiments (T2K, Compass units produced at CERN/EST laboratory). Concerning our prototypes, for the basic tile of the barrel detector, the PCB is 100 µm thick to reduce the radiation length and to make the curvature easier. The drawing of the PCB is shown on figure 1.3. It has 288 strips, (0.300 * 493 * 0.015) mm^3, with a 100 µm insulation gap between them. One pad at the top of the detector is reserved for the micromesh high voltage supply connection. A 1 mm wide guard ring runs around the active area for electrical grounding. The total mesh capacitance is around 300 pF. The connectors are soldered onto the top of the detector after the production of the bulk MM.

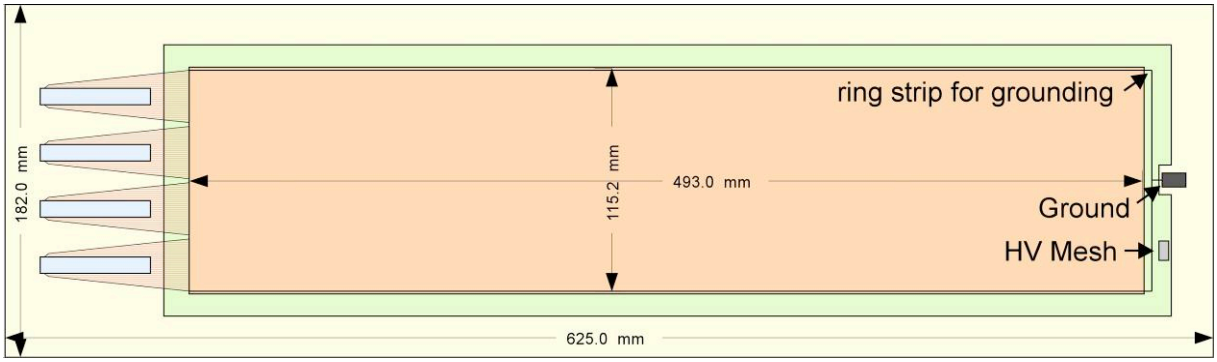

Figure 1-3 : PCB for bulk Micromegas CLAS12 demonstrator.

1.2.3. The bulk Micromegas production

The process begins with the described anode PCB. At this stage, the (493 * 115) mm^2 active area of the detector is placed on a larger and thicker FR4 circuit for handling and manufacturing purposes. We also asked the Bopp Company to deliver clean, controlled and individually packed woven meshes. The Seritec Company then stretches the mesh at around 6 N/cm on a frame using tools dedicated to serigraphy.
A special oxidation of the top copper layer of the PCB allows for a better adherence of the Micromegas pillars. The photo-imageable polyamide film is a Coverlay (DuPont Pyralux PC).

This film yields more robust and stiff pillars enabling a better, complete and effective cleaning and drying of the detector at the end of the bulk MM production.
The main steps of the manufacturing process for bulk Micromegas are summarized below (see Figure 1-4) [6] :

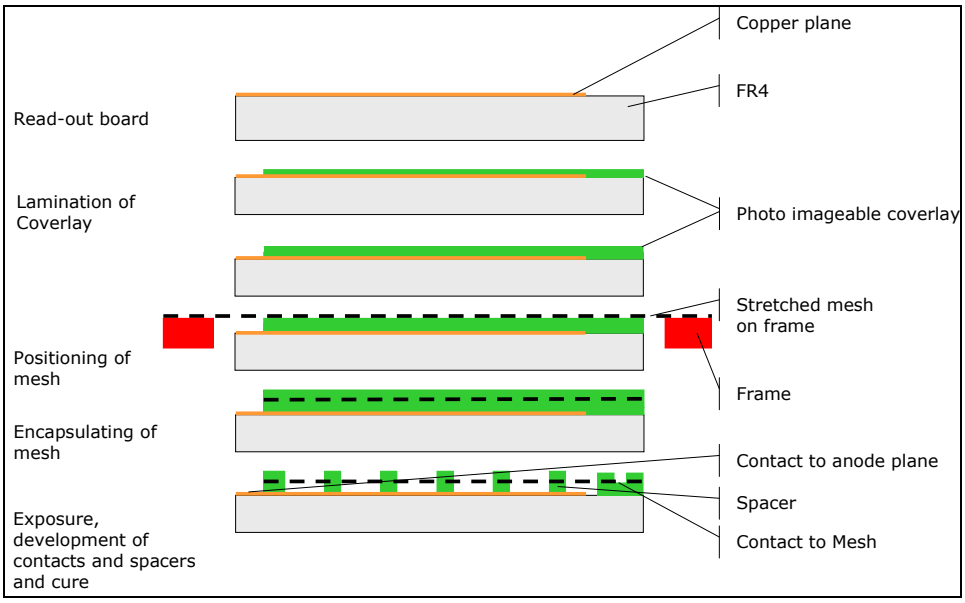

Figure 1-4 : Schematics of the Bulk fabrication

1. Preparation of the PCB image (with the strips, etc.)
2. Thermal stress of the PCB to fix the dimensions
3. Lamination of Coverlay (2 times, 128 microns thick)
4. UV exposure of the first coat
5. Positioning and encapsulating of the mesh by a third lamination
6. Development, cleaning and drying
7. Stabilization of the Coverlay

The radiation length associated to this type of detector is around $2.4.10^{-3}$ $g.cm^{-2}$ as illustrated in Figure 1-5.

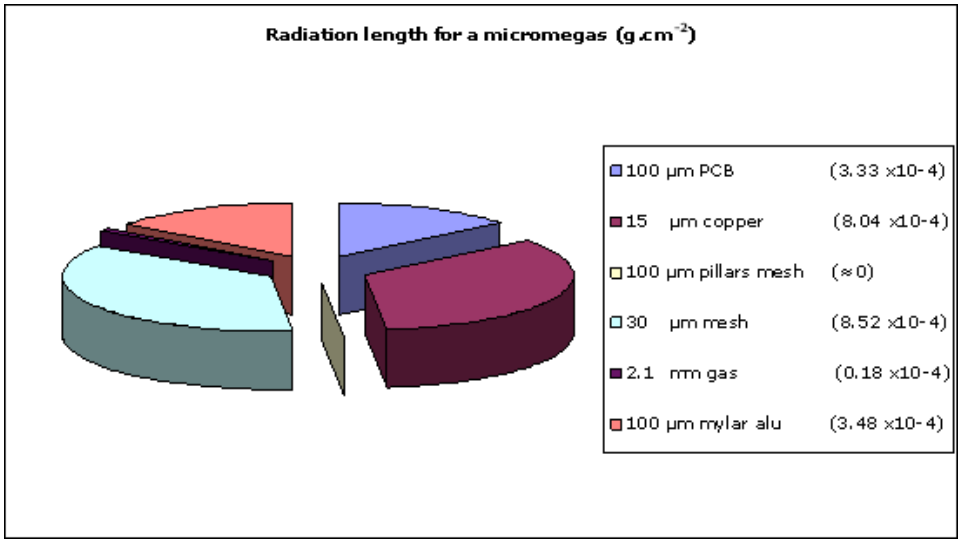

Figure 1-5 : Radiation length budget

2. The Design: CAD Study

The CAD study done in 2007 should be considered as a feasibility study of a MM tracker but not as a definitive solution since the requirements were not fully defined. The study was based on successful technical solutions validated by experiments before 2007. The goal was not to finalize the design but to look for possible show-stoppers and initiate R&D to solve them
Two options were explored maximizing the length of the strips and the length of the connection to the front end electronics (FE). The first solution, with 400 mm long strips and 300 mm connection length (COMPASS experiment) appeared to be complicated for the forward tracker electronics implantation downstream the solenoid. The second one, with 600 mm long strips and 800 mm connection length, allowed a much easier implantation with all electronics located upstream.
The R&D done in 2008 proved the possible use of long flex cables and confirmed the upstream option for FE. This R&D on flex cables initiated the As-Far-As-Possible (AFAP) philosophy for the front end without significant S/N losses (see section 5.3.2). The AFAP leads to higher cost in flex cables but simplifies the tracker implantation by separating the detectors and the electronics.

2.1. Silicon and Micromegas mixed solution

This study was done on a mixed solution for the central tracker with two silicon tracker layers at low radius and three Micromegas layers at higher radius.
The proved benefit of the mixed solution (see simulation Table 1) should lead towards a symbiosis between the two types of detectors rather than a simple addition of two different layers of detection.
The topics that should be examined are:

- Mechanics
  - Common tracker structure
  - Common alignment system
  - Localisation in space for minimum dead zone and maximum spatial resolution
  - Common connectors and/or flex cables

- Electronics
  - Common ASIC
  - Common Concentrator
  - Common DAQ

- Collaboration on various topics mentioned above during the development phase.

2.2. CAD 2007: Central Tracker

In this study the barrel tracker consists in two silicon layers and three Micromegas layers. The forward tracker is composed of three Micromegas layers.

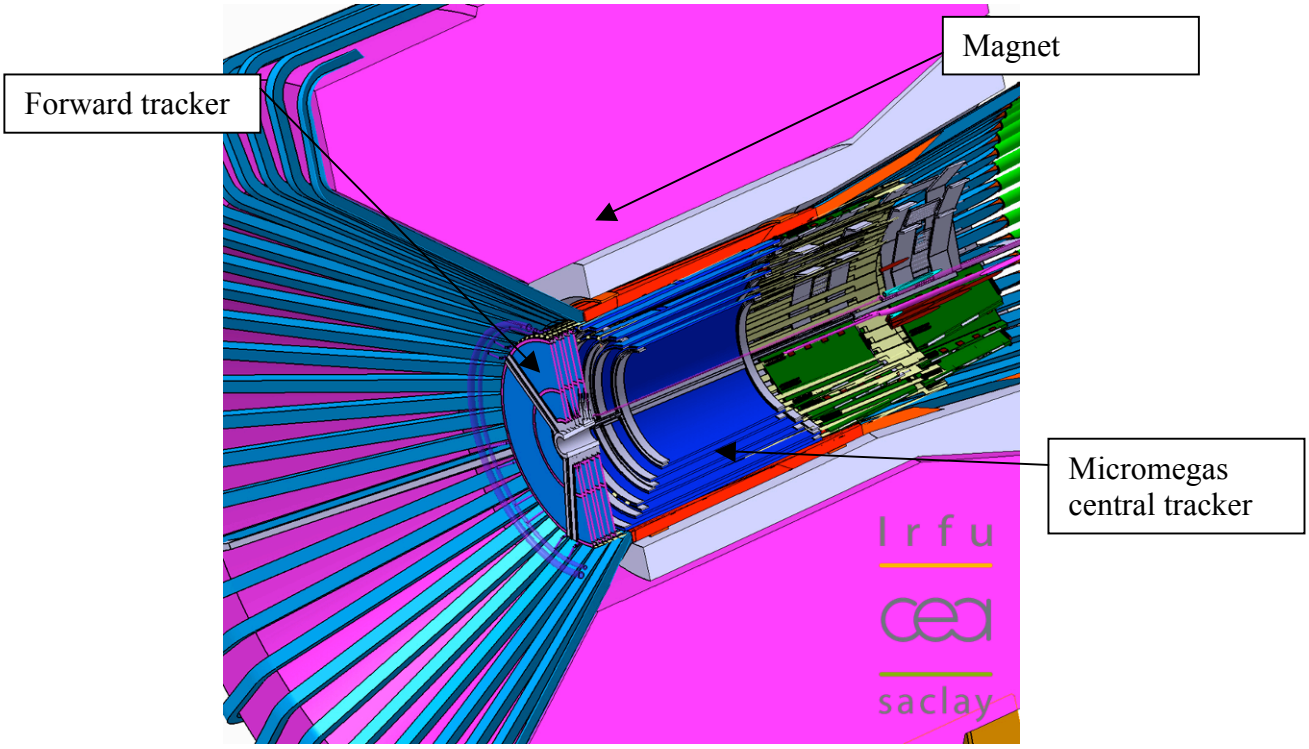

Figure 2-1 : Micromegas implantation, section view.

Each layer of detection is composed of two MM detectors with X and Y strips at 90°. The usability of a single X-Y detection PCB board, to reduce by a factor of two the number of detectors, will be studied in 2009.

2.2.1. X and Y tiles for the cylindrical detectors

The X detectors have their strips parallel to the beam while Y detectors have their strips along the circumference. The strips distribution leads to two different types of shape for X and Y detectors. The X detectors have the same length as the cylinders on which they are mounted and their numbers can be adjusted for each diameter according to an angular cut. For the Y detectors the strips are the longest, up to 1.5 m, and their numbers should be minimized to reduce the number of FE channels.
In this study we chose to divide the circumference in 3 in order to keep the surfaces of the detectors similar to that of detectors which had already been working on other experiments. The maximum size of the detector PCB active area is related to the PCB manufacture tool used to bulk the PCB. This size is now 600 mm in one dimension and at least 800 mm in the other dimension. The size of the different tiles composing the tracker has to be studied to define several standard PCB sizes to be curved at different radii with different lengths. Our basic design considers 230 µm wide strips separated by 70 µm gaps.

Detector	Radius (mm)	length (mm)	Circumference (mm)	Surface (m^2)	X strips number	Y strips number
d1X	110	255.6	691	0.18	2082	
d1Y	120	255.6	754	0.19		2556
d2X	170	383.2	1068	0.41	3330	
d2Y	180	383.2	1131	0.43		3831
d3X	230	509	1445	0.74	4575	
d3Y	240	509	1508	0.77		5088
			Total surface :	**2.72**	9987	11475

Table 2 : Barrel tracker dimensions.

2.2.2. Central detector structure

Each PCB is mechanically fixed to a light structure called Detector Structure (DS) which sets its curvature. This DS has still to be optimized with regards to material budget. The drift Mylar window with its silicon join is glued to the curved PCB.

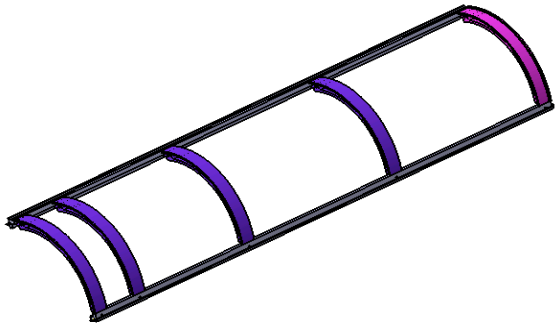

Figure 2-2 : Central detector elementary structure.

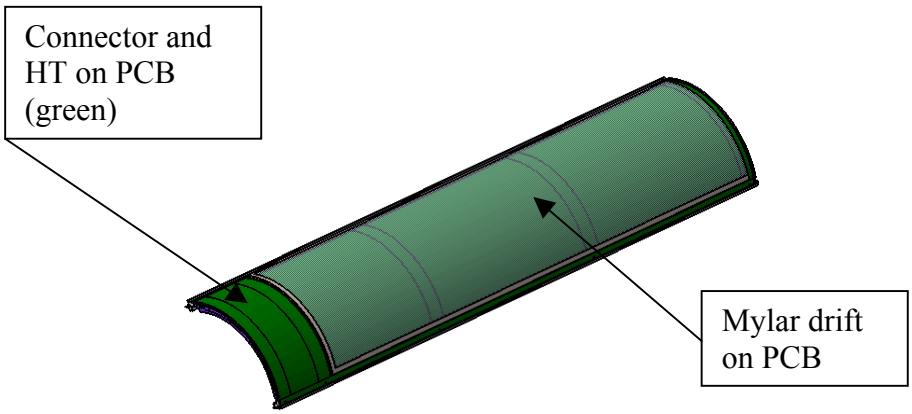

Figure 2-3 : Bulk Micromegas tile.

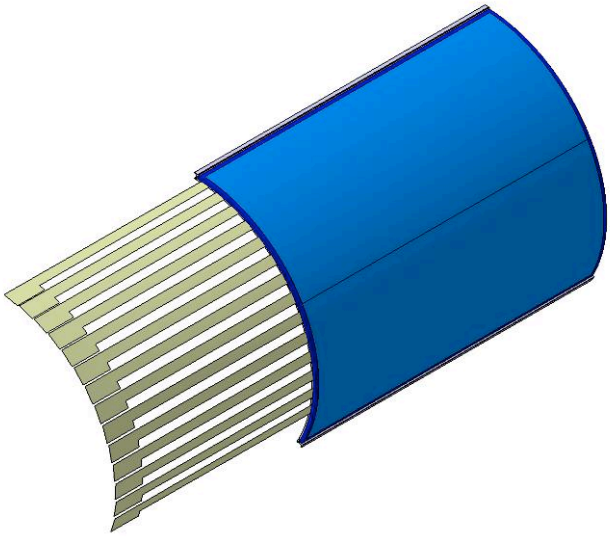

Figure 2-4 : Large tile (X) with flex cables.

Figure 2-5 : Detail of rail shape for fixation.

2.2.3. Central structure

The central structure will hold the bulk tiles on several radii for the barrel and at several positions for the forward disk. The dead zone generated by the DS will have to be adjusted with the neighbour detectors. Each tile will be extractable from the structure independently from the others. The whole DS with its detectors and electronics will be extractable from the magnet through a slide rail system to be designed.

The electronics box will be hooked to the DS allowing:

- Box dismounting
- Single flex disconnection
- FE and concentrator card access.

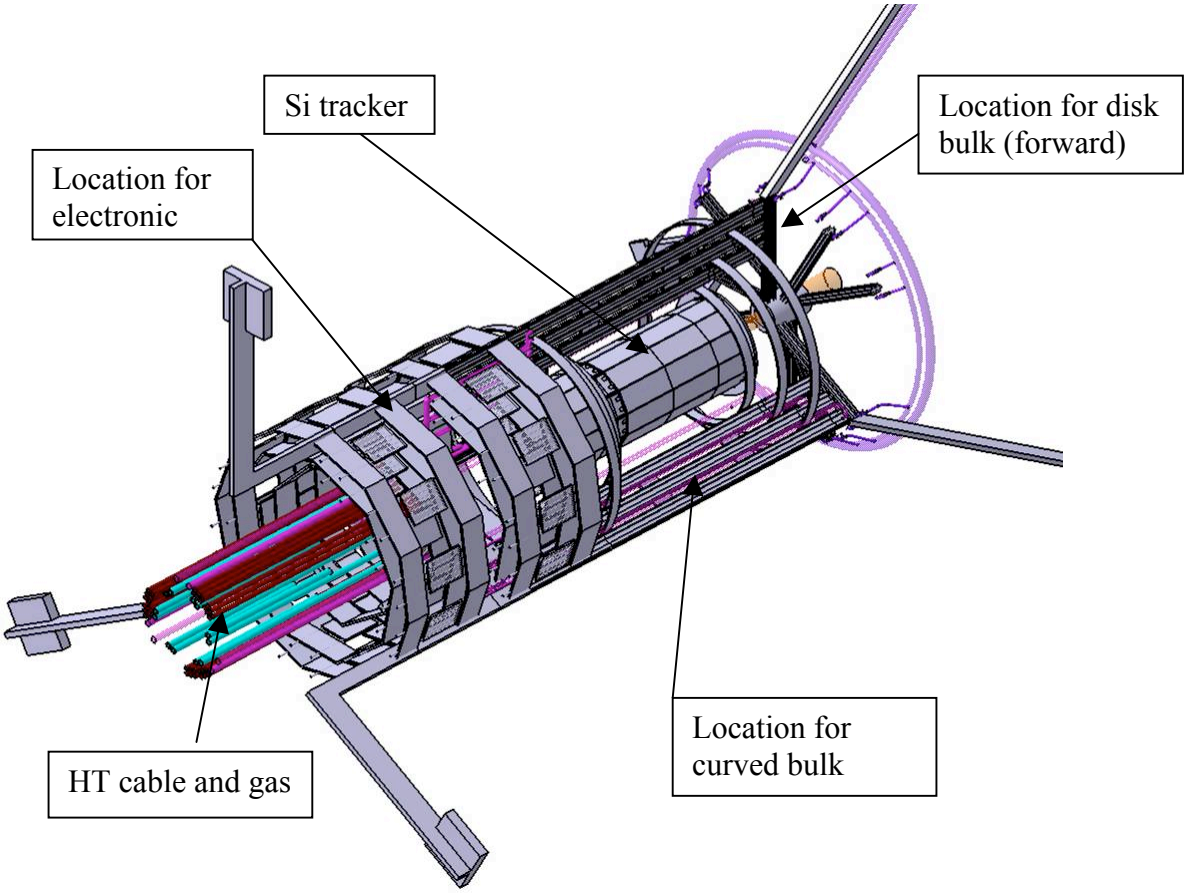

Figure 2-6 : Central structure.

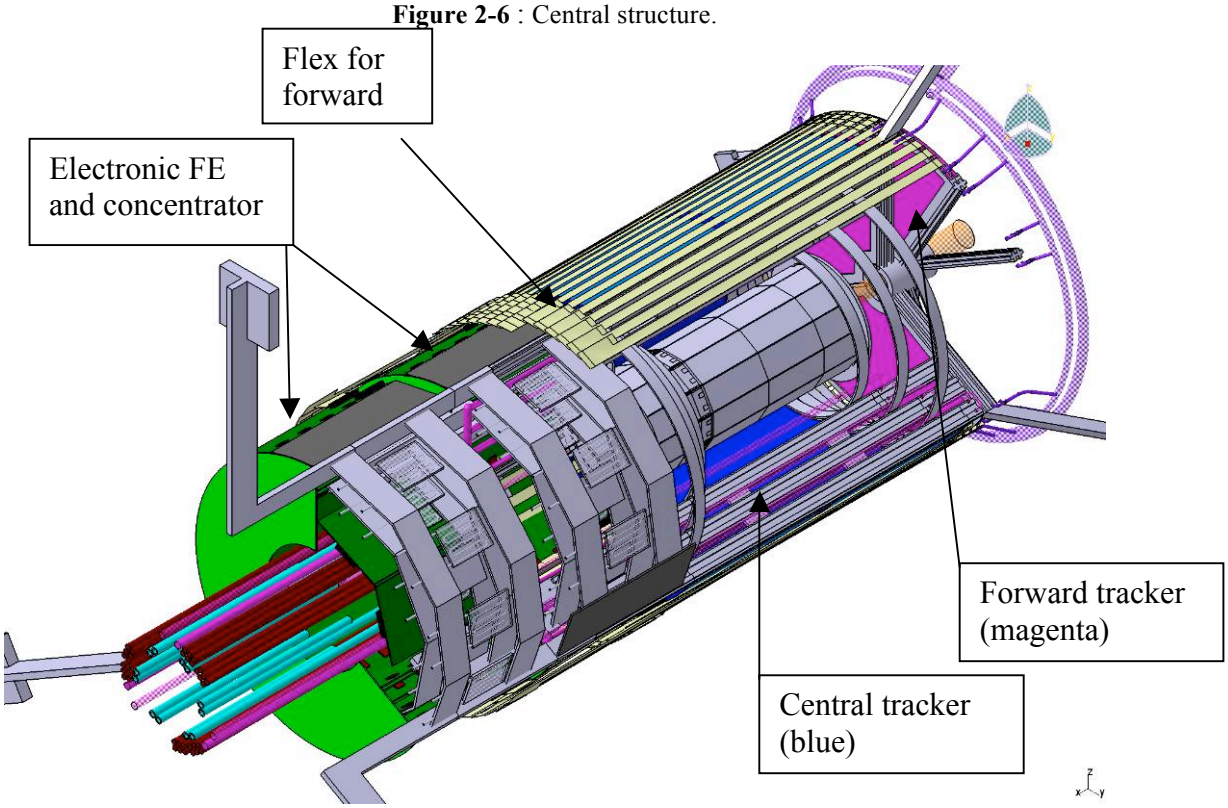

Figure 2-7 : Central structure half equipped.

Barrel tracker
(blue)

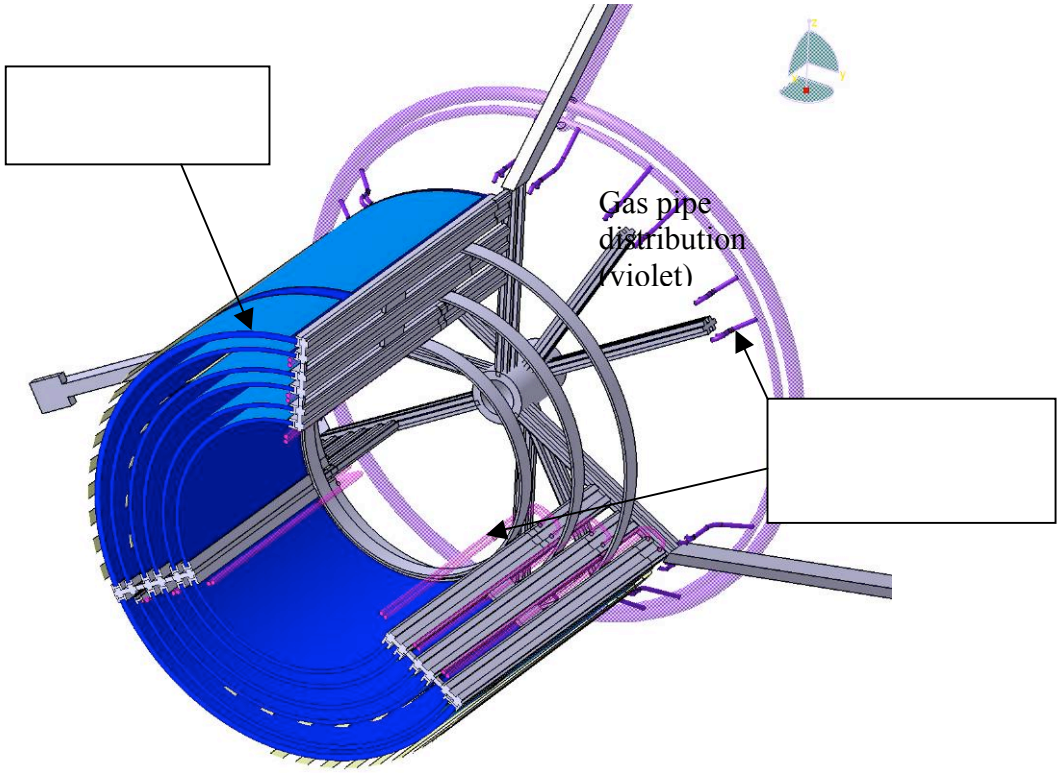

Figure 2-8 : Section view of structure equipped with 2/3 barrel Micromegas.

In this first study we have a rather large dead zone of 30 mm which can be minimized and another kind of structure has to be worked out.

2.3. *Forward Micromegas Tracker*

2.3.1. Forward tracker set up

In the 2007 study, the forward tracker consisted in three layers of flat disks. Each disk is two faced with U strips on one side and V strips at 60° on the other side. Each disk side is divided into 3 sectors (6 in the most recent simulation).
The disks are located just after the cylindrical tracker every 15 mm. The sectors of each twin disk are not aligned to avoid dead zones.

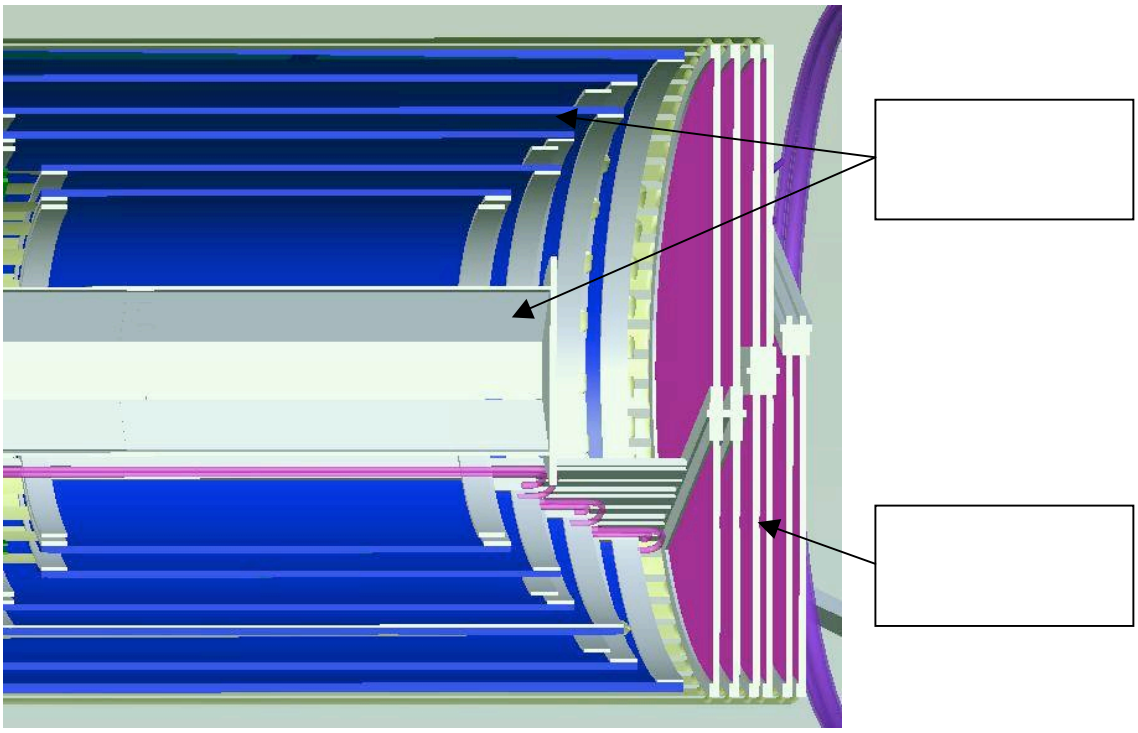

Figure 2.9: Cut view of FMT.

	Internal diameter (mm)	External diameter (mm)	Surface (m^2)	pitch (micron)	Number of strips
Disk	25	250	0.19	300	1500
Total			1.17		9000

Table 3: Forward tracker dimensions.

To obtain a thin flat Micromegas, the PCB has to be set on a support, in contrast with a barrel type tile that stays curved when constrained. We first considered to use the COMPASS technique [7] using a 3 mm thick Nomex honeycomb panel on which the 100 µm thick PCB is glued and the detector stays flat.

Mesh segmentation

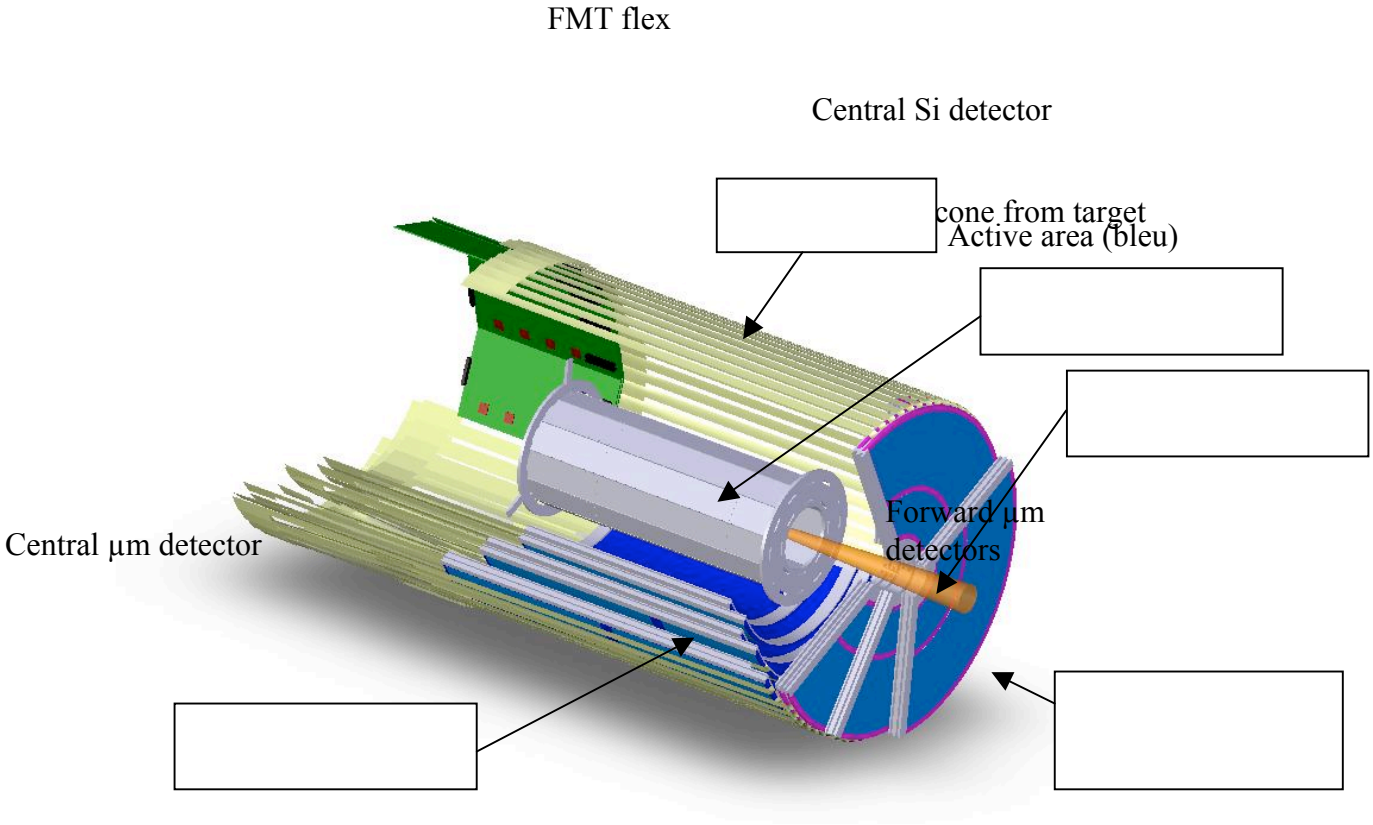

Figure 2-9: Mounting of the forward tracker.

The two faced MM disk sectors (U and V) are mounted on a sector structure equipped with their aluminized Mylar drift window.

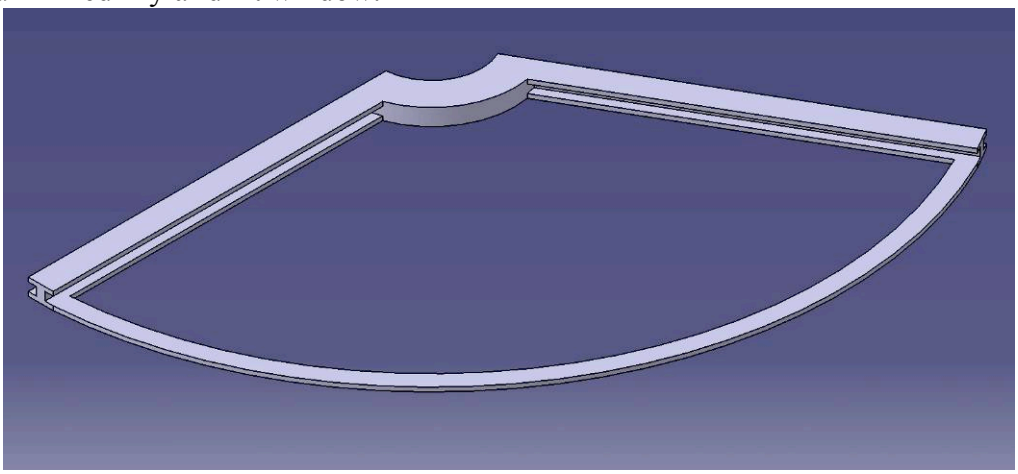

Figure 2-10 : Forward sector structure.

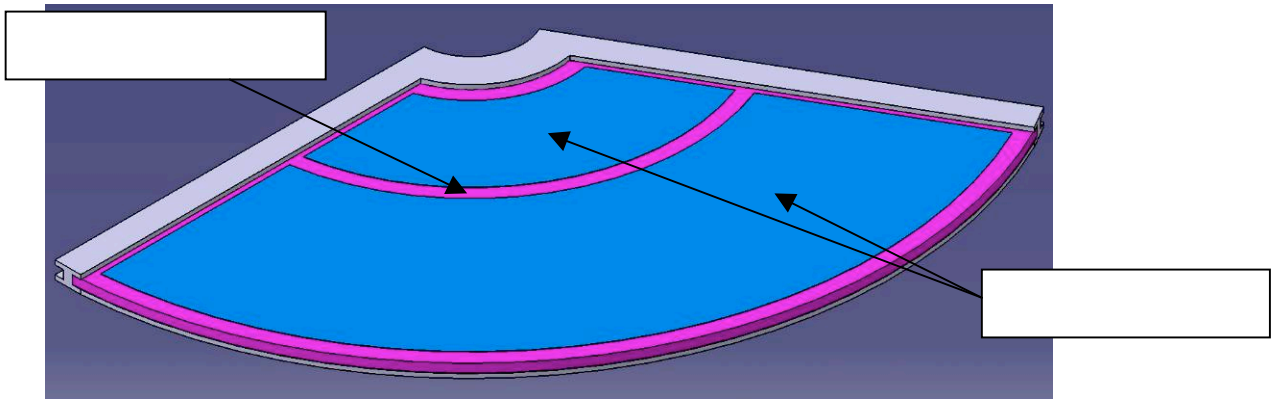

Figure 2-11 : Disk sector in the structure.

The 2007 option considered several disks with identical diameters. This option simplifies the fabrication for the 6 disks (3 twin X and Y) are the same (rotate at 90° for X and Y). Another option, not studied yet, is to bring the disks in the cylinder at the end of each cylindrical layer using disks with 3 different diameters. This In-Cylinder option does not help for readout, HV and gas connections but will need to be considered since the high threshold Cerenkov might come in the way in the first implantation option.

2.3.2. Mesh segmentation

In order to reduce dead time due to discharges when there is high occupancy at low radii, the mesh will be divided in several (2 in this study) independents areas. While sparking in inner region, the detector will still be operating in the outer region. An R&D on mesh segmentation will be done in 2009-2010 to study the minimization of the dead area between the two mesh surfaces and to validate the concept on a prototype in beam.
The connection to FE is done on the periphery by flex cables going between the CTOF and the last central tracker layer (see Figure 2-9 and 2.13).

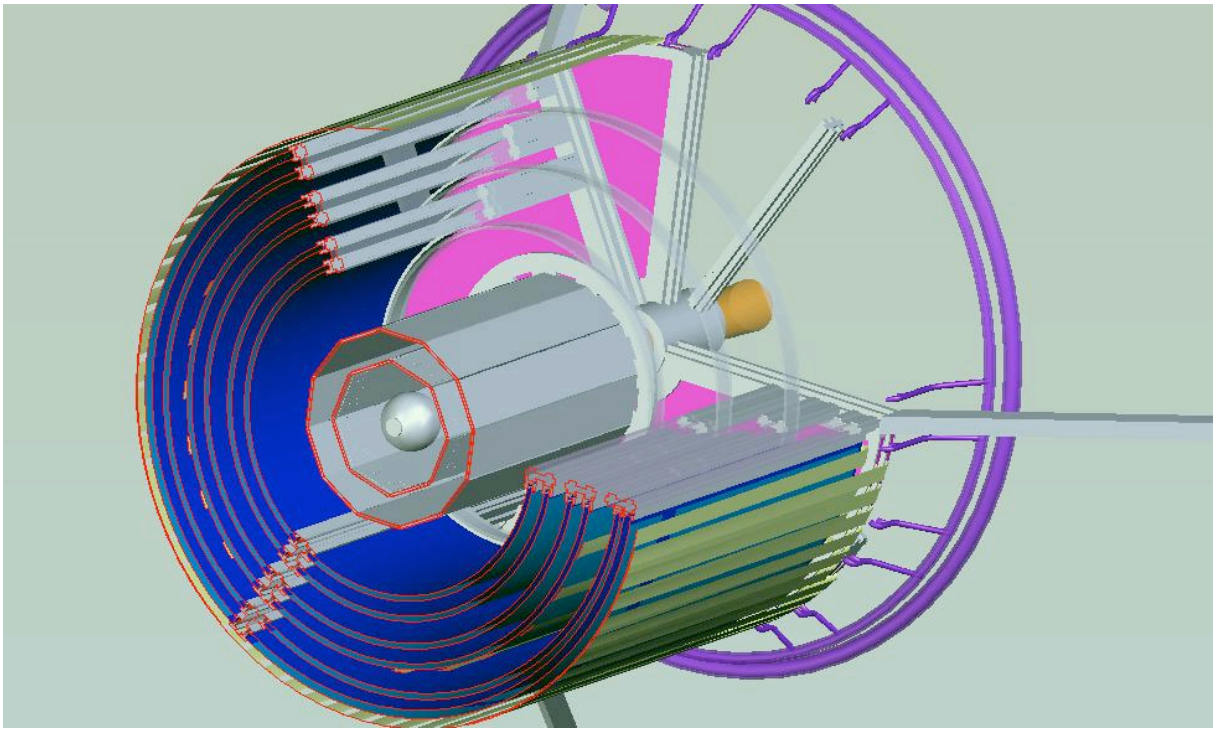

Figure 2-12: Section view of forward and central tracker.

3. Initial characterization of the detectors

Raw detectors bulked at CERN/EST lab are finalized at Saclay, where the drift electrodes are prepared and glued, and the electrical connections added. The detector has then to go through a standard quality test to check its characteristics, mainly gain homogeneity, energy resolution. This protocol is considered as the lab calibration of the detector. During this first characterization, only the mesh is read.

3.1. The setup

The whole calibration is realized using X-rays from a ^{55}Fe source (5.9 keV) interacting with the Ar 95 % - iC_4H_{10} 5 % gas mixture which is feeding the detector. The source is placed above a section of the detector, measurements are performed and then another section of the detector is investigated.

To measure the gain and calibrate the detector, all the strips are grounded together. The HV power supply used is a CAEN 471A for HV1 (drift voltage) and HV2 (micromesh voltage). A filter is placed between the power supply and the drift electrode. As for the mesh, an ORTEC 142B preamplifier is used to filter the power supply and to provide the signal readout coming from the micromesh. The signal is amplified and shaped by an ORTEC 472A amplifier. The signal is monitored online on an oscilloscope and recorded and analyzed using a multichannel analyzer (MCA).

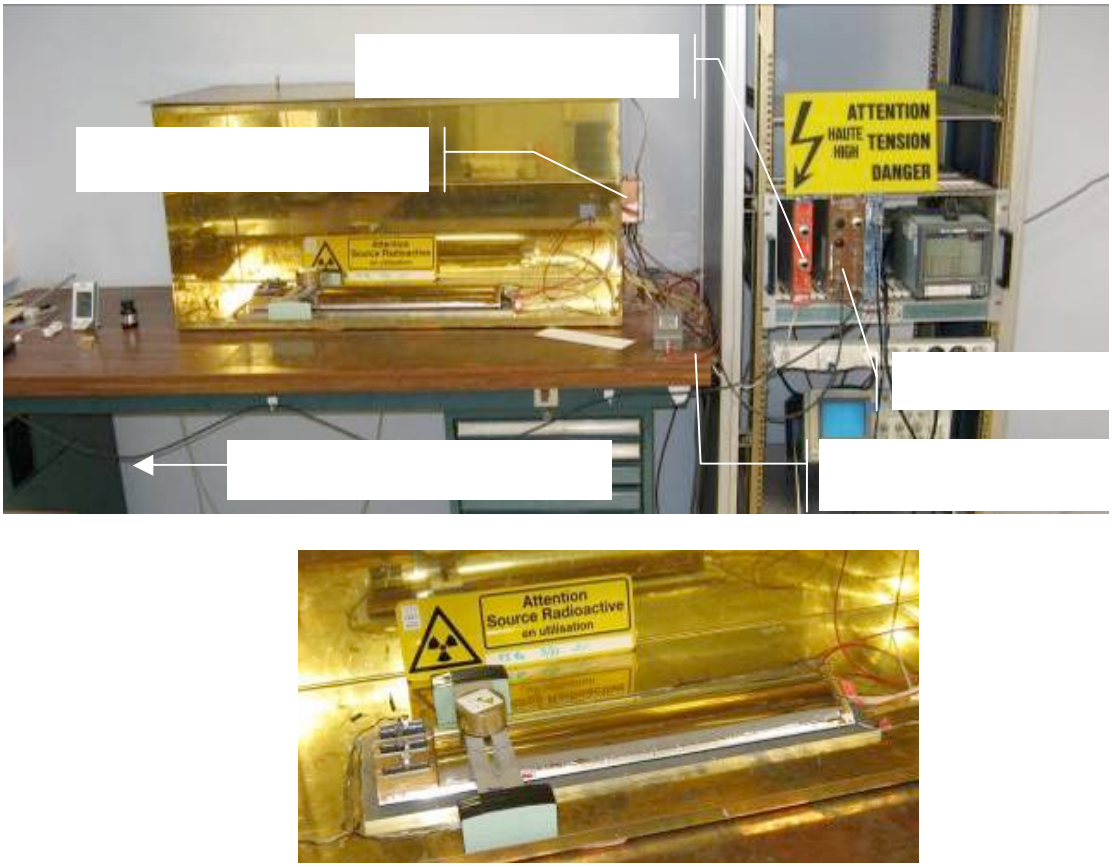

Figure 3-1: (up) Test setup of the CLAS12 demonstrator. (down) zoom of the setup.

For each detector, the gain homogeneity and the energy resolution are tested as well as the evolution of the gain vs. the micromesh voltage and the transparency (gain vs. Ea/Ed, ratio of the amplification gap to conversion gap electric fields). Finally, to check the effect of the bending of the detectors, they are fully characterized flat first then curved (see Figure 3-2 and Figure 3-3).

3.2. Results

3.2.1. The homogeneity

The detector is virtually divided in 15 sections. The gain and the energy resolution are measured for each section (grids). On the grids the data divisions are arranged as if one is looking at the detector from above with the connectors on the left hand side.

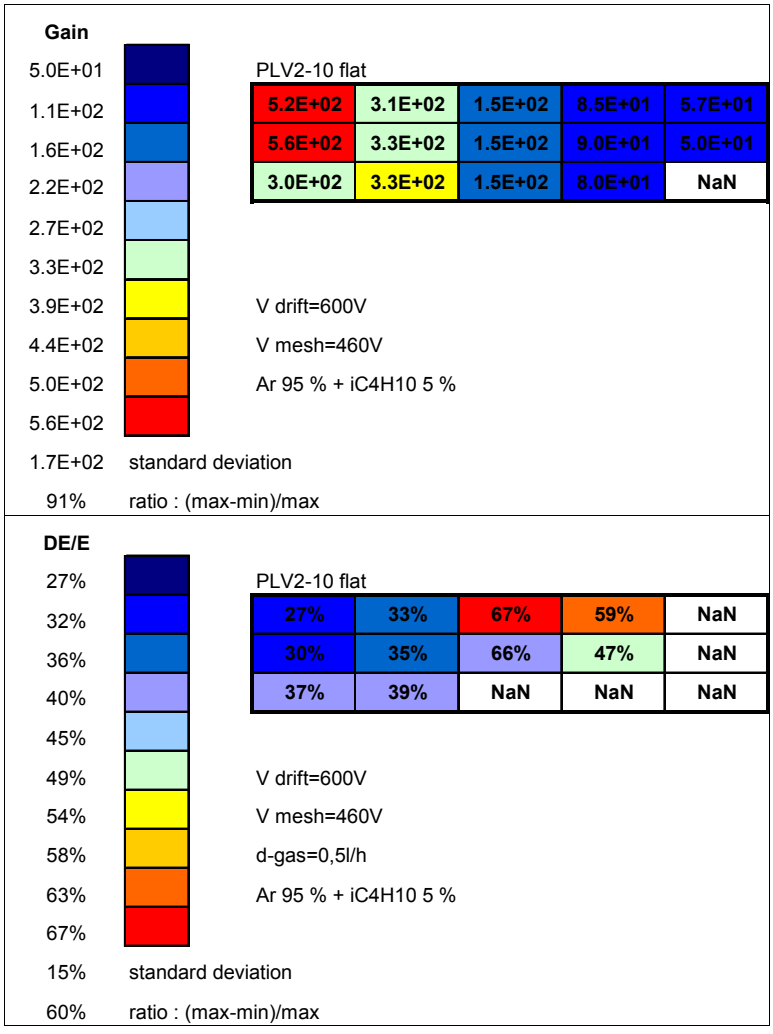

Figure 3-2: Gain (up) and Energy Resolution (down) maps for flat detector PLV2-10. Na/N areas were too noisy to reliably extract gain or energy resolutions. Note that this situation improved once the detector was curved, as shown in the next Figure.

The mechanical stress applied to the mesh during fabrication creates differences in the gap height in the region between pillars when the detector is flat. The detector is then rather

inhomogeneous as can be seen on Figure 3-2. In thick detector, (PCB thickness > 3.2 mm) the mesh is stretched up to 12 N/cm to obtain a homogeneity better than 1% on energy resolution (T2K data). On thin PCBs the mesh is stretched to less than 6 N/cm.

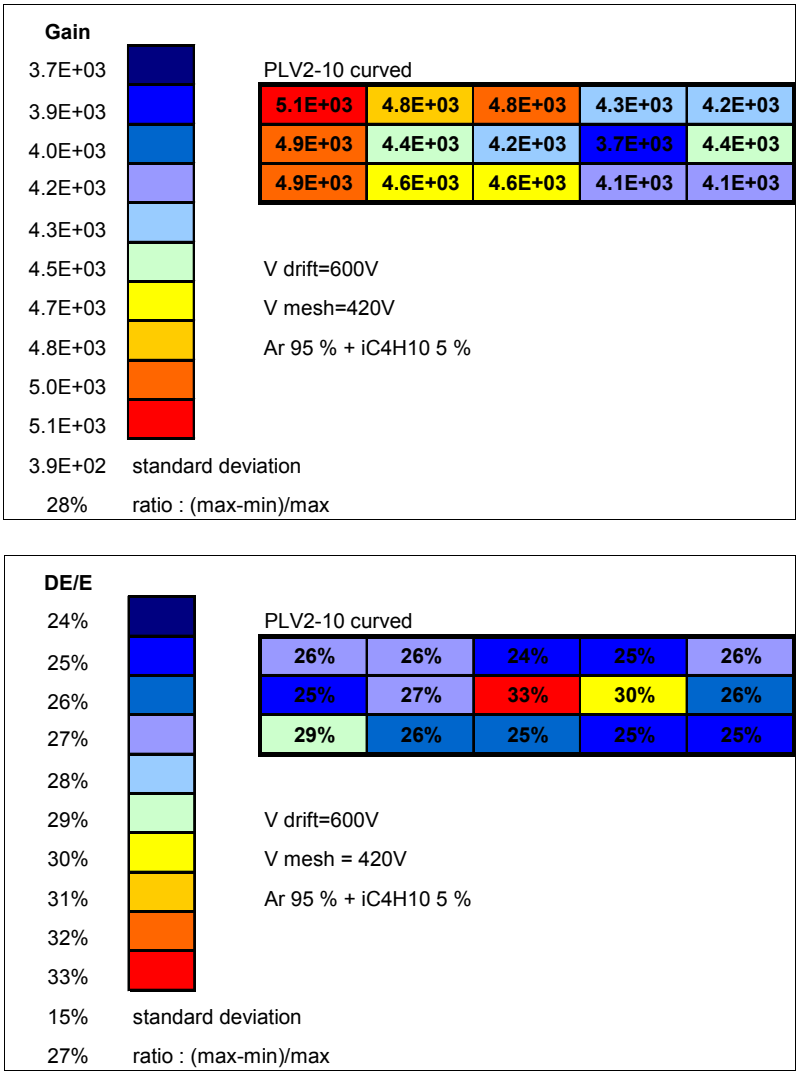

Figure 3-3: Gain (up) and Energy Resolution (down) maps for detector PLV2-10, once curved.

3.2.2. The gain

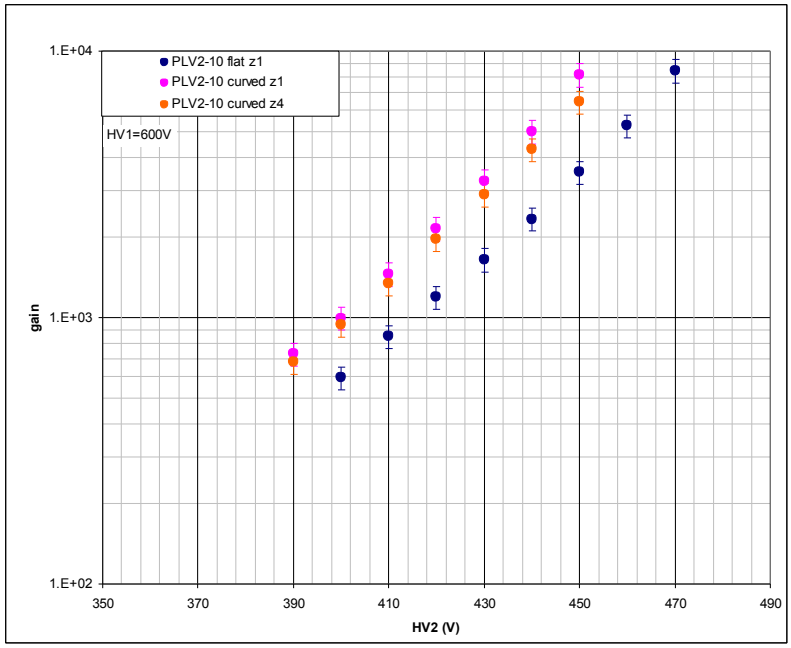

Figure 3-4: Gain versus micromesh HV for detector PLV2-10 flat and curved; z1 and z4 stand for different sections.

Curving the detector creates a new stress of the mesh between the pillars and the gap height becomes constant (the detector is homogeneous). Moreover, the gap height is set to the height of the small pillars and the gain is higher compared to the gain obtained when the detector is flat (see Figure 3-4). Tests were also done applying different radii to tiles but their behaviour was not affected. The capability to reproduce performances when curved and un-curved several time as been tested. After more than 10 bending/un-bending in a gas chamber no significant changes where noticed.

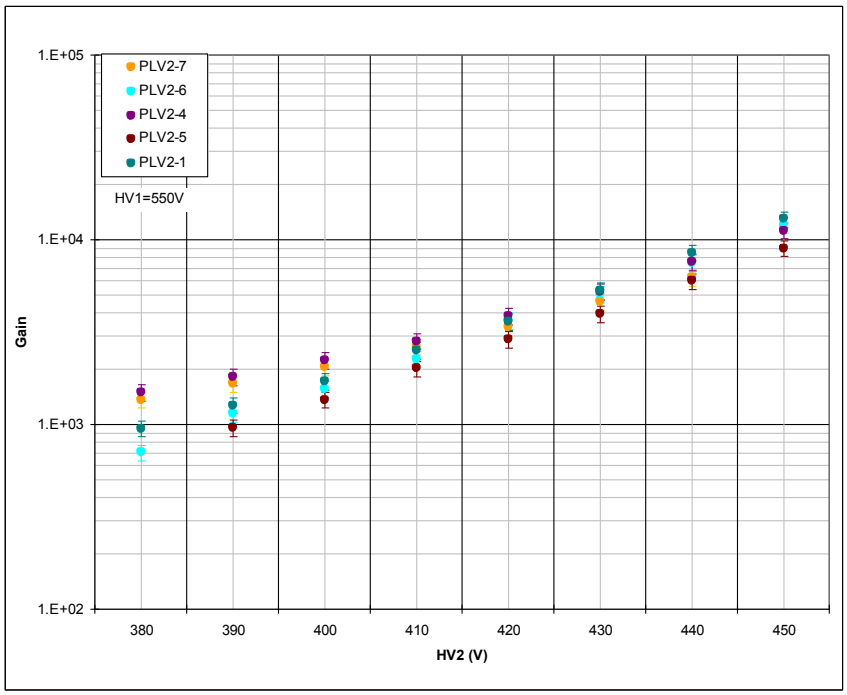

Figure 3-5 : Gain plots for different detectors.

The behaviour of the bulk detectors is rather stable, as far as gain is concerned, as shown on Figure 3-5. Tests were also done applying different radii to tiles but their behaviour was rather stable in the radius range we are considering for CLAS12 (r > 100mm) as seen on Figure 3-6 for energy resolution.

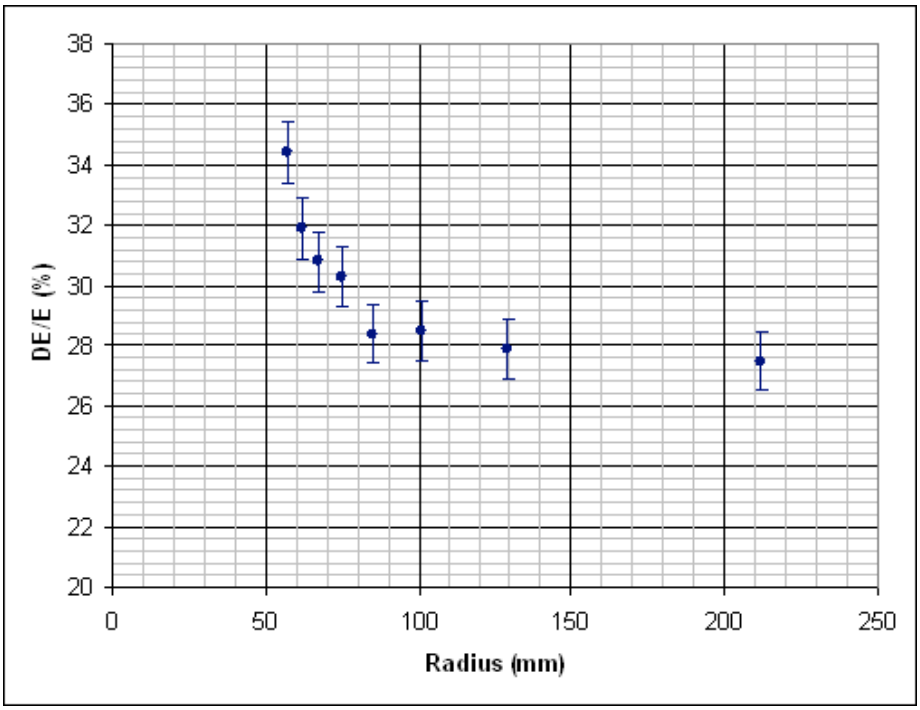

Figure 3-6 : Energy resolution versus different curvatures of the detector.

3.2.3. The electronic transparency

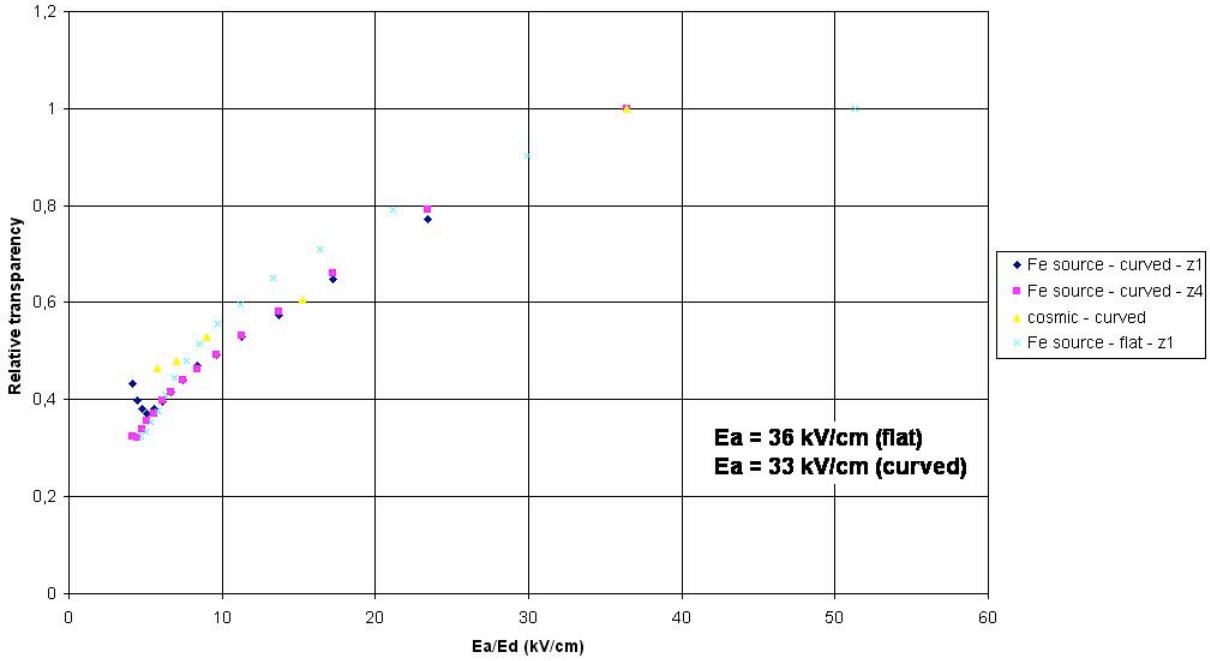

Figure 3-7 : Transparency plot for flat and curved PLV2-10.

On Figure 3-7, one can see that the transparency decreases with the ratio Ea/Ed as the high voltage applied to the drift electrode increases (which is one condition to limit the transverse electron drift, see section 4). The rise of the curved PLV2-10 transparency (blue markers) at low values of Ea/Ed is an indication of pre-amplification process occurring in the conversion gap as is foreseen for large Ed. It also yields a higher gain but may generate sparks. We also see that transparency measurements using cosmic rays give similar results.

4. Micromegas for CLAS12 simulations

In addition to its excellent performance, a Micromegas detector has three major advantages over a Silicon detector:

- Its price: all the components of a Micromegas are rather cheap compared to the price of Silicon wafers. For large area trackers, this price becomes rapidly prohibitive;
- The low material budget: as a gaseous detector, the material introduced in the spectrometer is very limited. A preliminary estimate gave around 0.16% of radiation length for a Micromegas layer, to be compared with 0.33% for a 300 microns Silicon wafer (that does not include the support structure and a possible cooling system).
- Ability to use a 90° angle between X and Y strips which improves the polar angle resolution.

Because the cost and the amount of Silicon are important issues for CLAS12, simulations based on Garfield [8] have been made to study the possibility to use Micromegas in the future vertex tracker.

4.1. Optimization of the detector with Garfield simulations (Barrel Tracker)

The first goal of these simulations was to find optimal characteristics of the detector so that it can work in the 5 T magnetic field of the solenoid. This high B field – transverse to the electric field E for a Barrel Tracker – indeed affects the motion of electrons that drift in the gas with a Lorentz angle θ, approximately given by:

$$\tan\theta = \frac{v(E)\times B}{E},$$

where v is the drift velocity of electrons. With a standard Micromegas, θ is around 75°, as shown in Fig. 4.1 (left), and makes the detector unusable. The strategy is therefore to:

- choose a gas in which the electron velocity is low, and the number of primary ionizations is large;
- increase the E field, e.g. the high voltage applied on the drift electrode, as illustrated in Fig. 4.1 (right);
- use a small conversion gap, so that the transverse drift of electrons is also small.

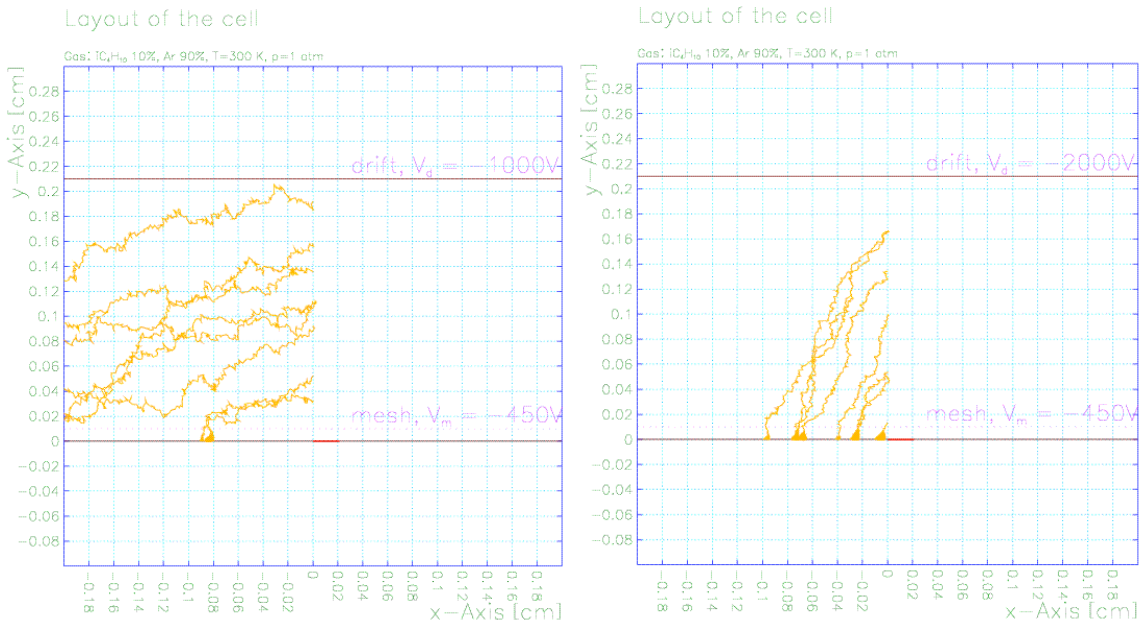

Figure 4-1 : Drift of electrons in the conversion region, in the presence of a 5 T magnetic field and a standard (left) or increased (right) electric field.

4.1.1. Choice of gas

The drift velocity can be reduced with a heavy gas, as illustrated in Figure 4-2 for Neon and Argon mixtures [9]. A heavy gas also has the advantage to produce more primary ionizations: 4.2 /cm for Helium (Z=2), 12 /cm for Neon (Z=10), 23 /cm for Argon (Z=18), and 44 /cm for Xenon (Z=54) [4]. On the other hand, heavy gases increase the probability of sparks due to highly ionizing particles, and the price of Xenon is relatively prohibitive.

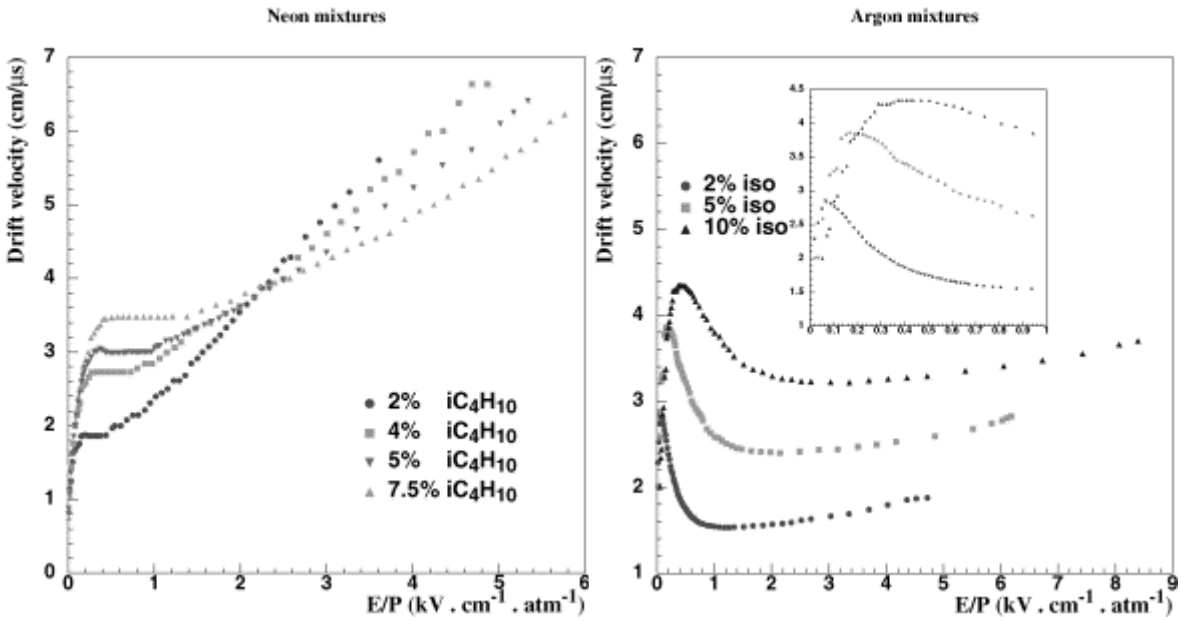

Figure 4-2 : Drift velocity of electrons in Neon (left) and Argon (right) gas. At fields above 5 kV/cm, the drift velocity is significantly larger in the lighter gas.

We therefore based our simulations on Argon mixtures, and studied the influence of different quenchers, as shown in Figure 4-3. Apart from CO_2, all of them give similar performances; we chose isobutane (iC_4H_{10}), the most commonly used quencher. Note that the gain, and then the spark probability, increases rapidly with the Argon concentration: this concentration should not exceed 95%.

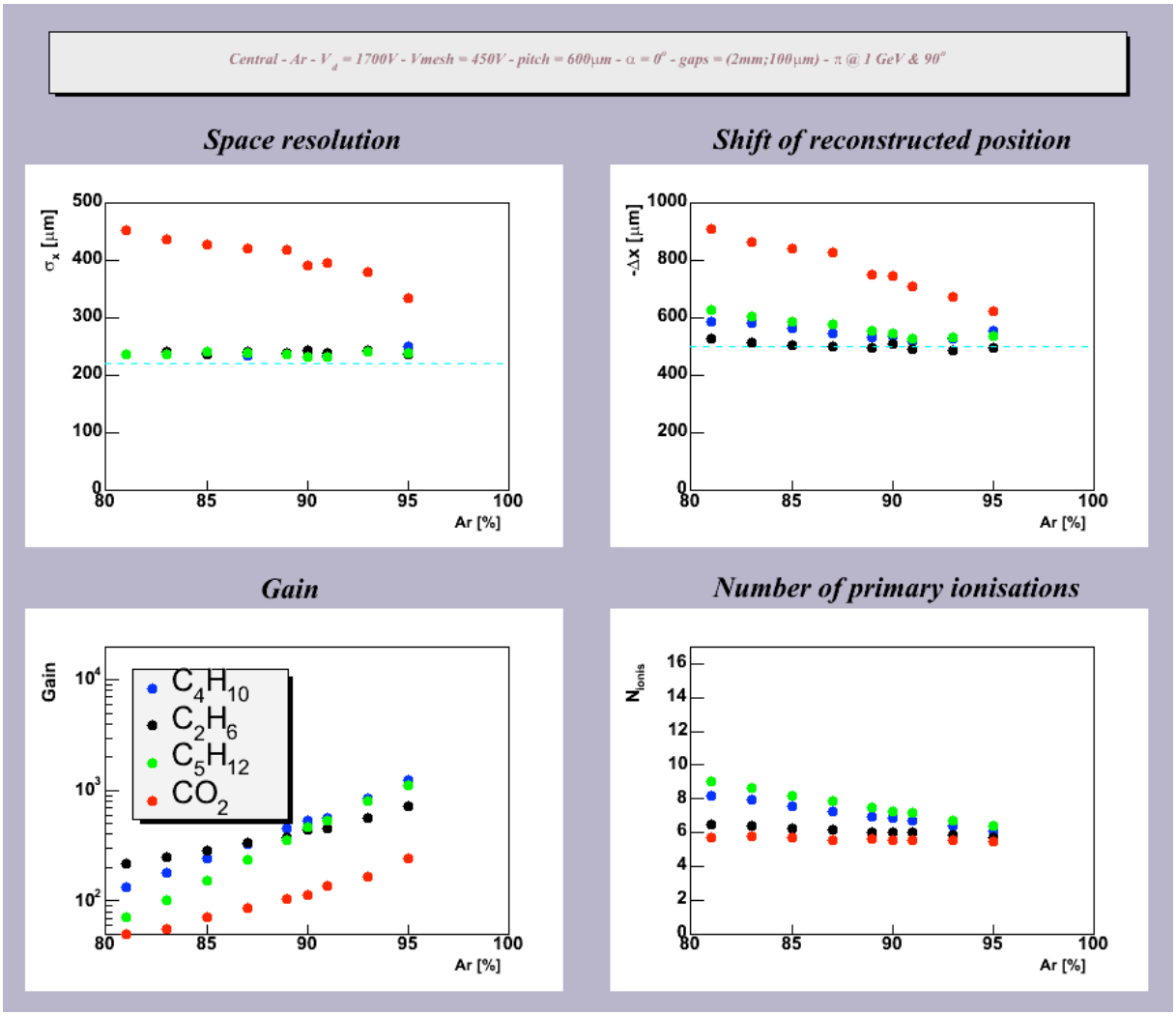

Figure 4-3 : Effect, with a 5 T magnetic field, of Argon concentration and quencher gas on the spatial resolution (upper left), the shift of reconstructed position due to Lorentz angle (upper right), the relative gain (bottom left), and the number of primary ionizations (bottom right).

4.1.2. Electric field in the conversion gap

In practice, it is not possible to increase the E field too much, as a decrease of the mesh transparency occurs, as well as a multiplication of sparks and instabilities if the regime of pre-amplification is reached. We see in Figure 4-4 that this regime starts for E fields around 10 kV/cm in Ar + 10% isobutane gas. Concerning the transparency, we already explained that the ability of the mesh to collect almost all the ions produced during the avalanche allows a Micromegas to have a much smaller dead time than classical gaseous detectors. This feature requires a ratio between the fields in amplification and conversion gaps larger than 8. In our case, this ratio is around 5.5 only, and the simulations showed that more than 20% of ions are

not collected by the mesh (without the magnetic field), whereas only 9% escape the mesh in standard configuration. However, the presence of the magnetic field modifies the drift lines of electrons in the amplification region, and it turns out that a large part of the avalanche takes place closer to the wires of the mesh, as illustrated on Figure 4-5, so that only 11% of ions escape in the conversion region. We can therefore obtain small enough ion transparency.

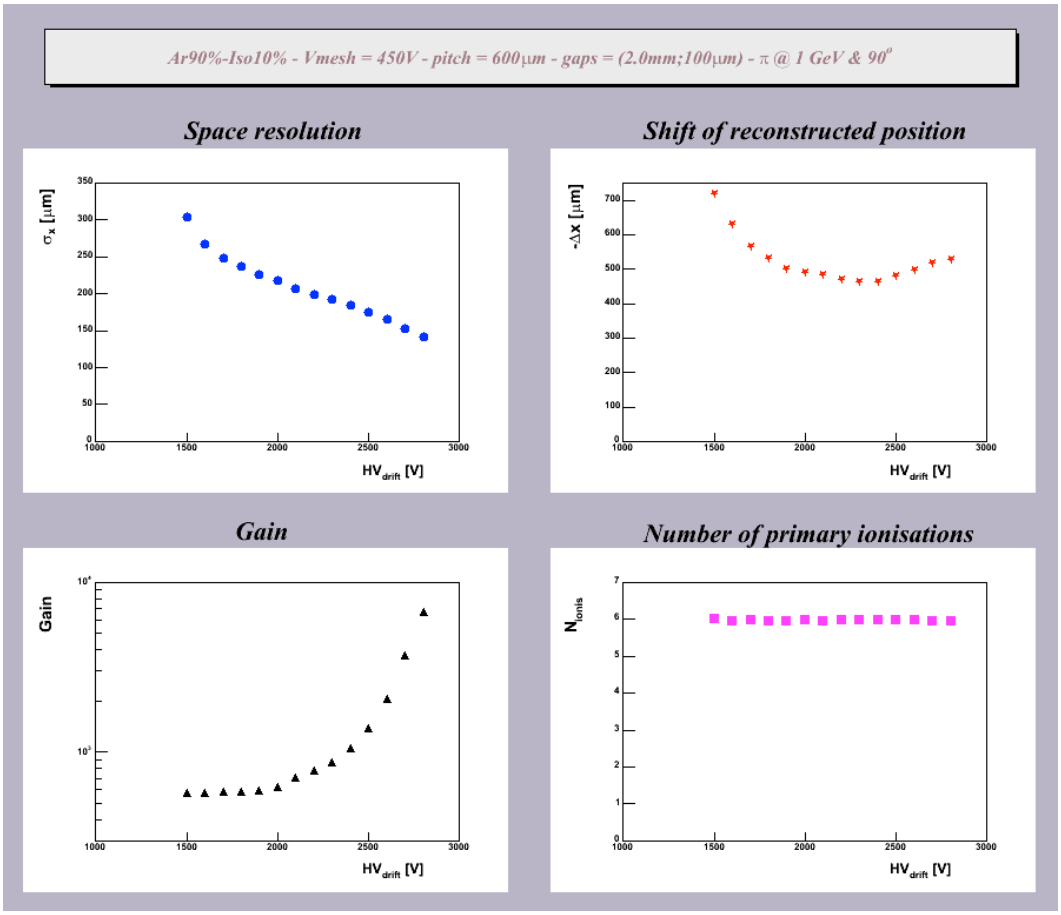

Figure 4-4 : Effect, with a 5 T magnetic field, of the electric field in the conversion region. The pre-amplification regime produces a rapid increase of the gain for high voltage above 2000 V, that makes the detector quite unstable.

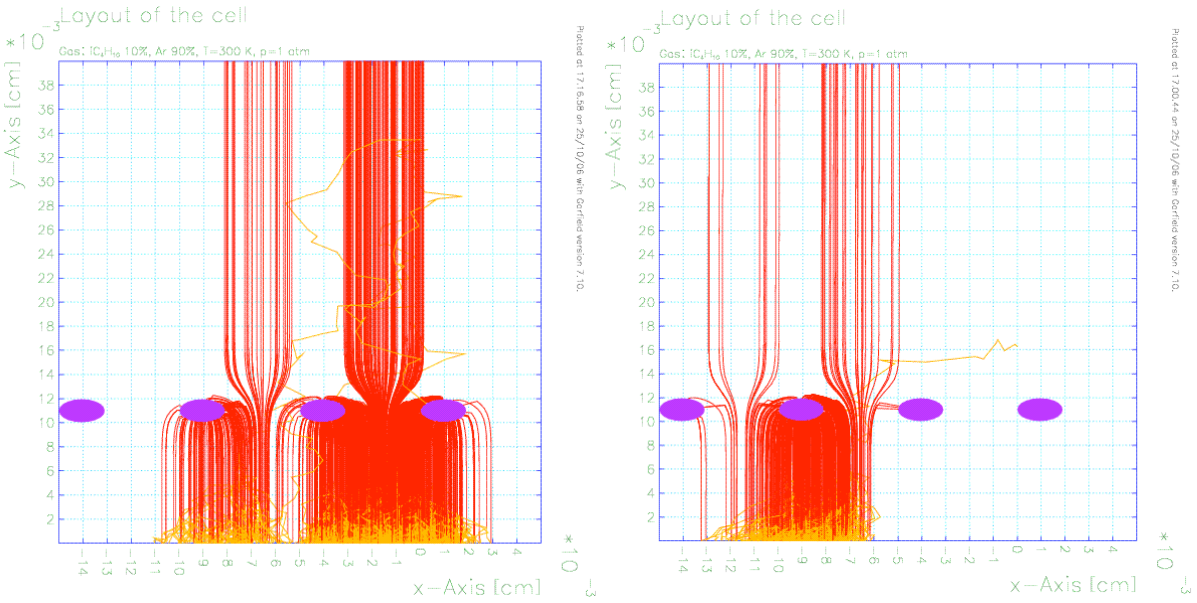

Figure 4-5 : Drift lines of electrons (yellow) and ions (red) close to the mesh, with increased electric field in the conversion region, at 0 T (left) and 5 T (right). In the first case, many ions produced in the avalanche escape in the conversion region, increasing the dead time of the detector. In the second case, the ions are produced closer to the wires of the mesh (in purple), and are therefore collected.

4.1.3. Conversion gap

Finally, the conversion gap should not be too thin, as the average number of primary electrons N is directly proportional to its size. As the number of ionizations follows a Poisson distribution, N too small would lead to detector inefficiencies (given by e^{-N}), corresponding to cases where no primary ionizations occur. In practice, a safe value for N is around 6 (e^{-6}<0.3%), which is reached with a 2 mm gap in Argon +10% isobutane mixture.

4.1.4. Pitch

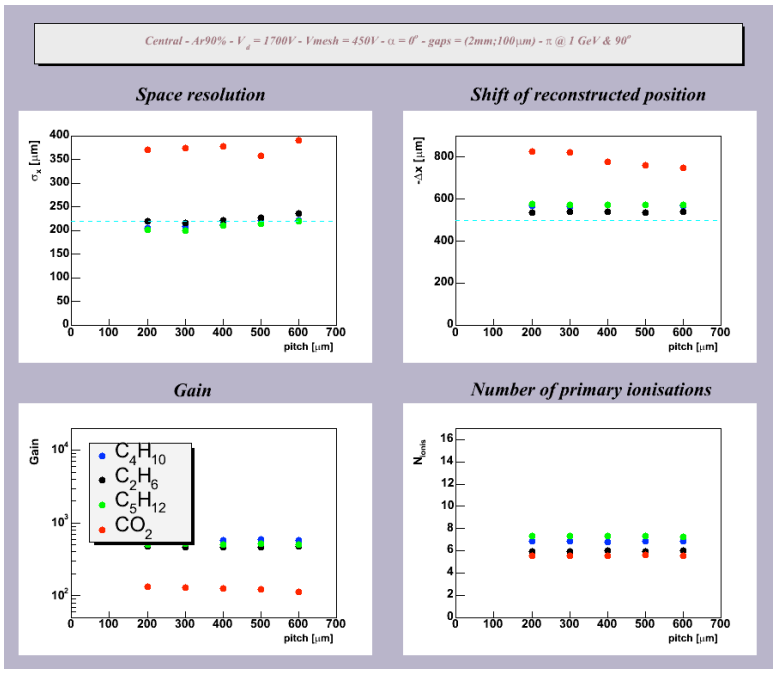

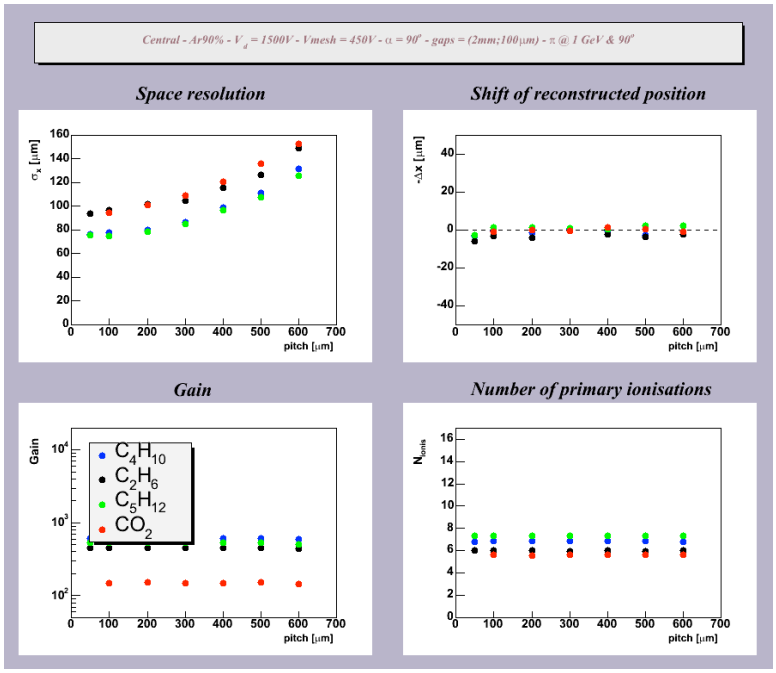

Figure 4-6 : Effect of the pitch on the performance of the Micromegas with strips parallel (top) or perpendicular (bottom) to the magnetic field. A too small pitch is unnecessary, as the spatial resolution reaches a plateau.

Now that the main characteristics of the detectors have been determined, mainly by the CLAS12 environment, we can study the effect of the pitch on the resolution of the Micromegas. This effect is shown in Figure 4-6, both for strips parallel (X) and perpendicular (Y) to the magnetic field. In both cases a plateau appears, telling us smaller pitches are useless. A good compromise between the resolution and the number of channels is therefore at the beginning of this plateau, *i.e.* with a pitch around 300 µm.

4.2. Performance of the barrel tracker

To compare various barrel setups (Silicon only, Micromegas only, or a combination of these detectors), we now have to estimate the performance of the Micromegas as a function of the track parameters. It turns out that the energy of the particles (MIPs or close to) has almost no effect, so only the angles of the particles will affect the performance.

4.2.1. X detectors (strips along the magnetic field)

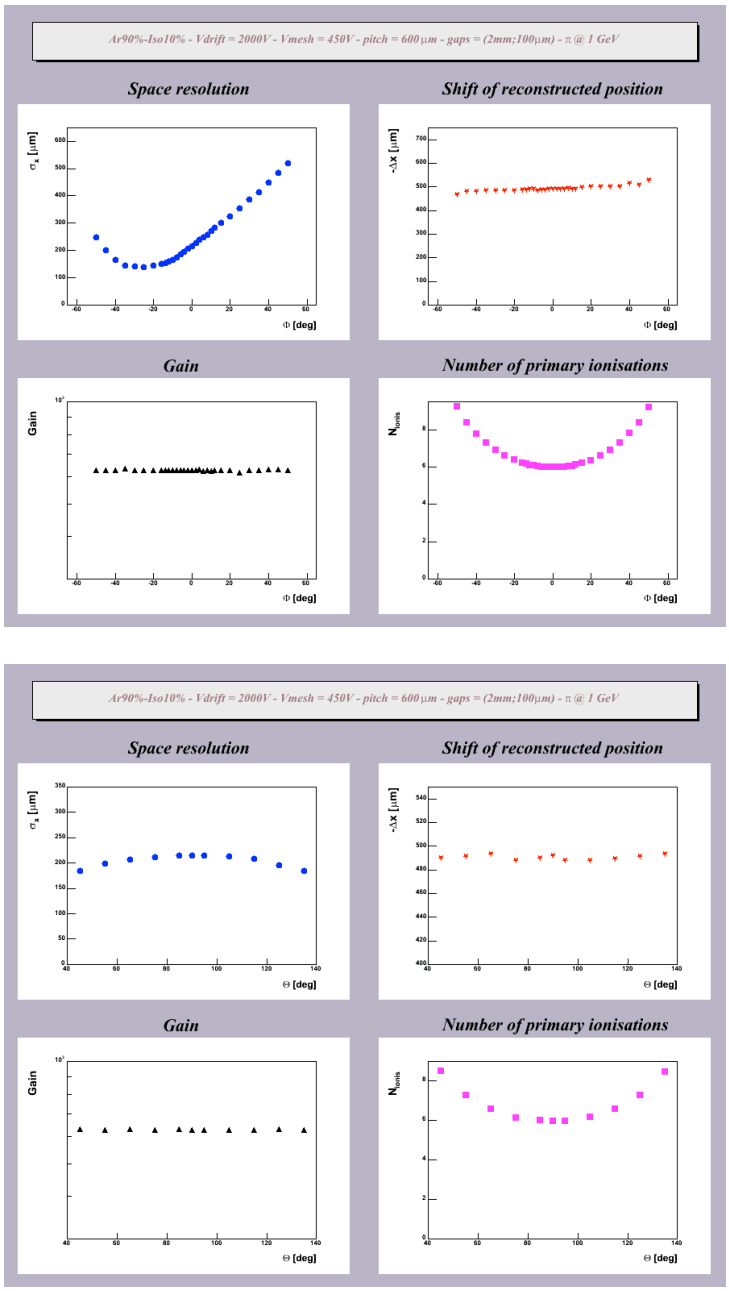

Figure 4-7 : Effect of the local azimuthal (top) and polar (bottom) angles of the incident particle for a detector with strips parallel to the magnetic field.

The performance of the detector as a function of the *local* azimuthal (φ) and polar (θ) angles of the particles is shown in Figure 4-7. As expected, the effect of θ is small, and comes only from an increase of the path in the gas, leading to an increase of primary ionizations. The effect of φ, however, is quite strong, and leads to a significantly worse resolution for positive particles (that have a local φ > 0) than for negative particles. We finally obtain the following parameterization for the resolution of X detectors:

$$\sigma_X(\varphi,\theta) = (220 + 5.0\times\varphi + 0.041\times\varphi^2 - 0.00092\times\varphi^3 + 0.000011\times\varphi^4)\times\sqrt{\sin(\theta)}\,,$$

A similar expression can be achieved for the transverse shift of the position (due to the Lorentz angle).

4.2.2. Y detectors (strips perpendicular to the magnetic field)

In this case, the strongest effect comes from the polar angle (see Figure 4-8, Figure 4-9), as particles with $\theta \neq 90°$ will cross the gas perpendicularly to the strips. We finally get:

$$\sigma_Y(\varphi,\theta) = (920 - 17.4 \times \theta + 0.097 \times \theta^2) \times \sqrt{\cos(\theta)}$$

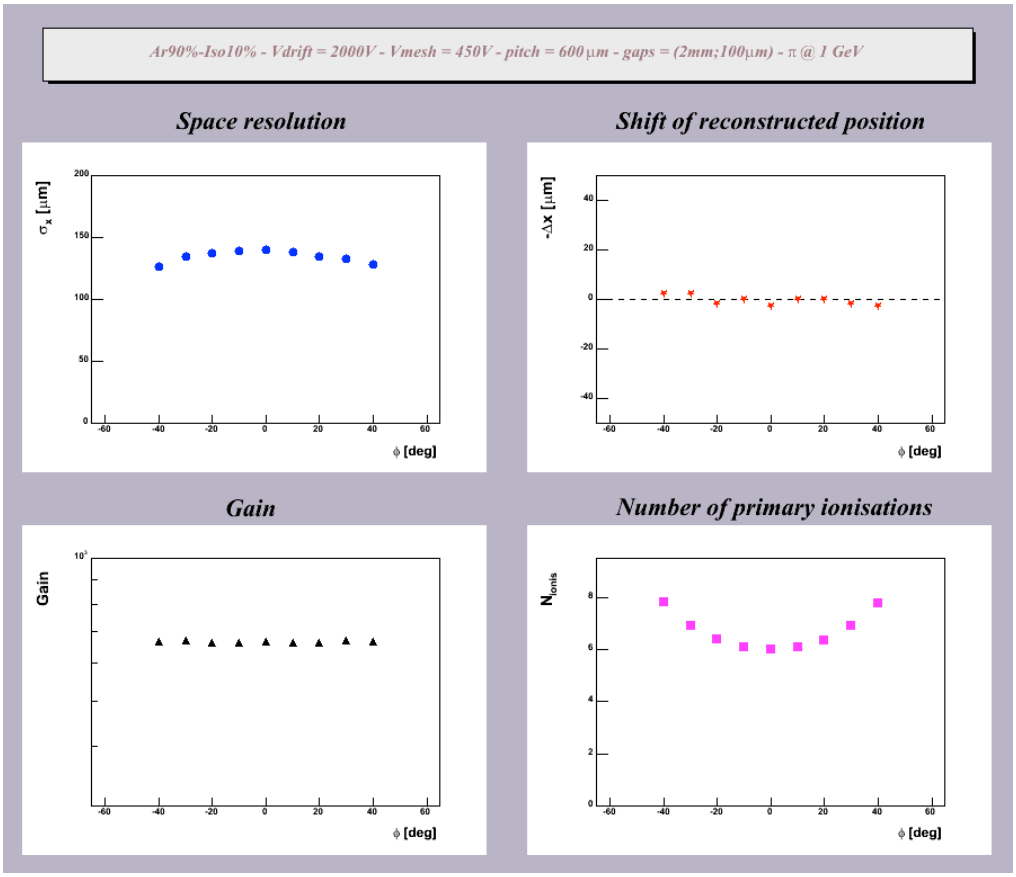

Figure 4-8 : Effect of the local azimuthal angle of the incident particle for a detector with strips parallel to the magnetic field.

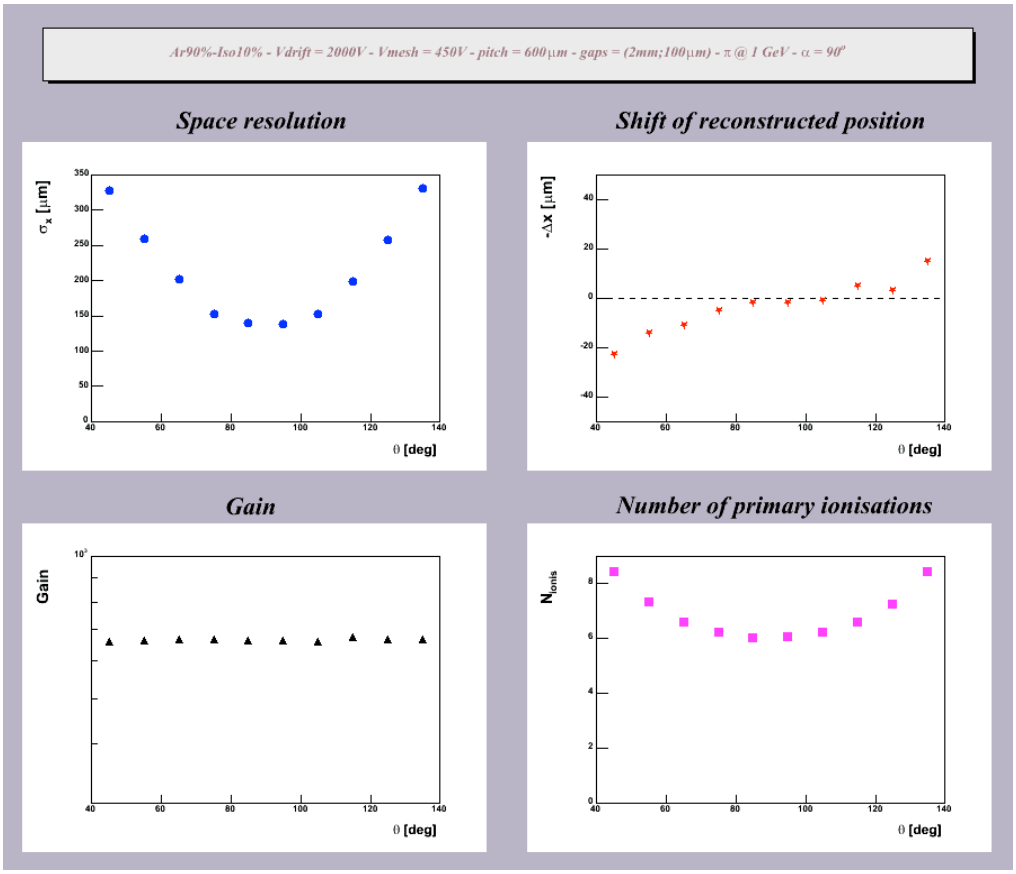

Figure 4-9 : Effect of the local polar angle of the incident particle for a detector with strips parallel to the magnetic field.

4.3. Performance of the detector for the forward tracker

We also made Garfield simulations for detectors in the forward tracker, studying the effect of the gas mixture, the pitch, the conversion gap, etc., but in this configuration, the magnetic and electric fields are parallel, and electrons drift in the gas with negligible transverse diffusion. In most cases, a particle will therefore hit only one strip (unless we use pitch below 100 μm, which seems unrealistic), leading to a resolution given by $pitch/\sqrt{12}$.

5. Micromegas detectors in a transverse magnetic field

As pointed out previously, one of the main difficulties in the proposed Micromegas setup in CLAS12 is the presence for the barrel of a strong magnetic field parallel to the strips and therefore transverse to the electric fields in the detectors. In such a setup, the drift electrons in the conversion region are deflected by a Lorentz force, which induces a systematic shift of the observed signal on the strips, but also a geometrical smearing of the electrons in drift region which reflects directly in a smearing of the total charge on more strips than without this magnetic field. This smearing effect directly affects the performance of the detector in terms of position resolution, which is an essential characteristic for a tracker.

The magnitude of the Lorentz deflection depends on the electron drift velocity in the gas, the value of the electric and magnetic fields as well as the distance between the drift and the mesh electrodes. In order to reduce this deflection as much as possible, one can change the gas mixture (*i.e.* the drift velocity), the electric field as well as the drift distance. In practice, all three variables can be optimized to run the detector in a reasonable configuration (see section 4.1)

The GARFIELD simulation provided us with an estimate of the Lorentz deflections for our detectors. Using these estimates, a nominal configuration using a small drift distance (about 2mm) and a large electric field on the drift electrode (around 2kV) seemed to provide a satisfactory position resolution despite the 5T transverse magnetic field inside the central detector of CLAS12 as explained in section 4. However, Lorentz deflections were never measured at such high fields and it has never been demonstrated that Micromegas detectors could perform adequately in such harsh conditions. It was therefore decided to perform direct measurements of this Lorentz deflection as a function of electric and magnetic fields, for a gas mixture of 90-95% Argon, 5-10% iC_4H_{10}. In a first stage, a warm dipole capable of reaching 1.5T field was used in Saclay. A second series of measurements were taken using the DVCS solenoid magnet at Jefferson Lab, capable of reaching 4.5T.

5.1. Measurement Principle

The main idea was suggested by I. Giomataris and first implemented in [9]. In order to simulate particles travelling through a detector in a controlled fashion, a UV Laser hitting the drift electrode (composed of an Aluminized Mylar) extracted electrons from the Aluminium in a very small area (typically a few tens of microns). These primary electrons drift just like the primary electrons from a particle, reach the mesh, and avalanche onto the strips as usual, giving us a “drift signal”. Figure 5.1 shows a transverse view of our experimental setup and electrons drifting in the problematic field setup: B collinear with the strips, and transverse to E. The quantity we extract is the so-called Lorentz angle, which is simply calculated from the shift observed on the strips and the distance between the drift and mesh electrodes. In our experiment, the Laser beam was strong enough to also extract electrons directly from the mesh, and therefore giving us a direct “mesh signal”. One could calculate event by event the distance between the mesh and the drift signal, but the mesh signal is usually contained in one strip only and its position accuracy is very limited. A better way to do this is to use a run with no B field to estimate the accurate position of the laser beam instead of the mesh signal event by event.

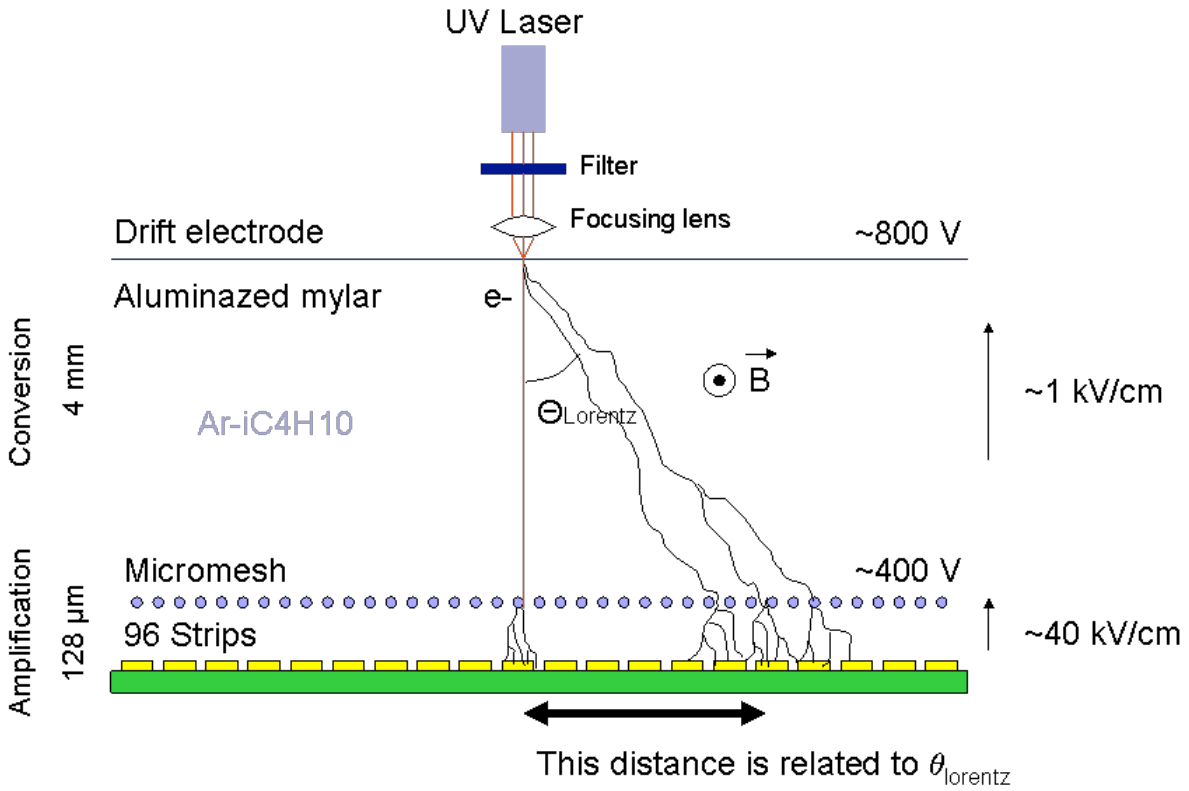

Figure 5-1 : Transversal view of the Micromegas in the magnetic field.

5.2. Experimental setup at Saclay

The detector we tested was the third version of the Micromegas bulk made at Saclay. Its active area is 30*30mm² and the strip pitch was 300µm. The stainless steel mesh was located at 128µm from the strips. The drift electrode is an aluminized Mylar foil located at either 1.88mm or 5.25mm from the mesh electrode, depending on the measurement which was performed. The detector was filled with a gas mixture of Argon 95% and iC_4H_{10} 5%. The magnetic field was generated by a warm dipole delivering up to 1.5T.

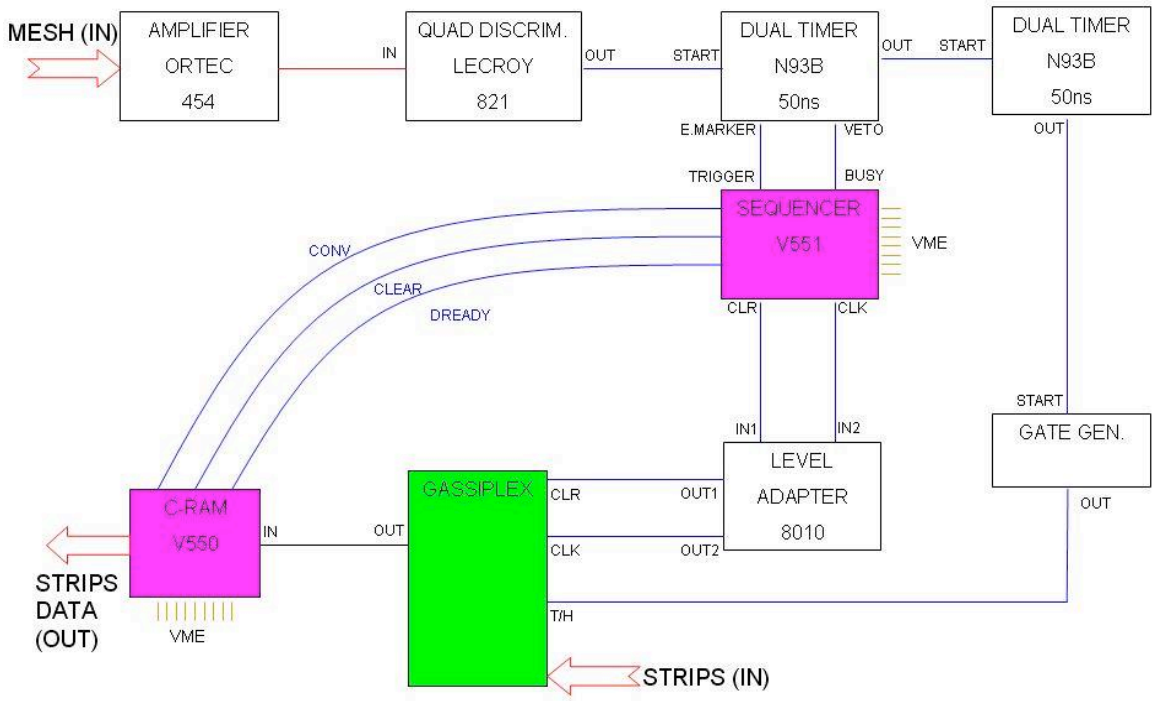

Figure 5-2 : Electronics schematic.

The front-end electronics used for the tests used Gassiplex cards, read-out by VME C-RAMS and Sequencer cards V550 and V551 (see Figure 5-2 for details). The mesh signal, once shaped and amplified, was used as a trigger for the electronics chain. The Data Acquisition software (DAQ) was a home-made Labview VI (front-end shown on Figure 5-3). The output was a simple ASCII file which we used in a ROOT-based analysis tool offline.

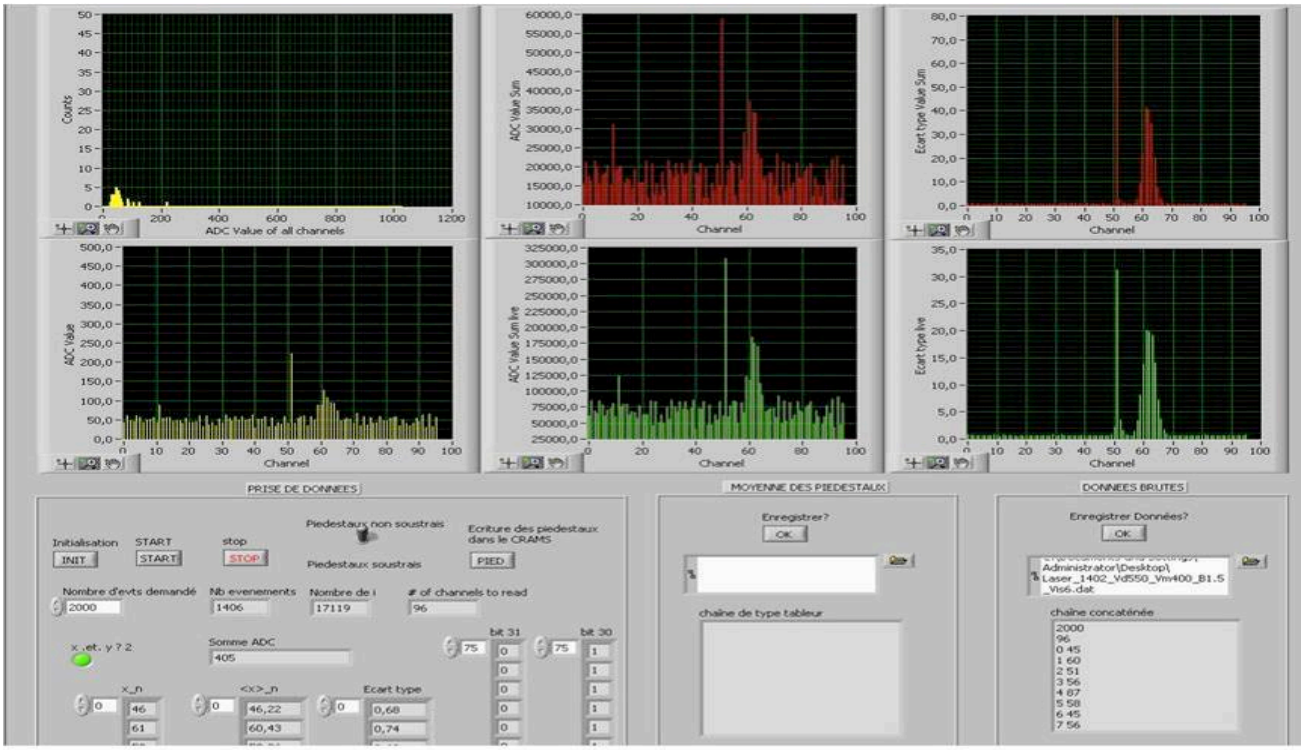

Figure 5-3 : Labview DAQ.

B=0 T

B=1.5 T

5.2.1. Data Analysis

Our main observable is the Lorentz angle as previously discussed. In order to calculate this value, we use the histogram of the average position of the drift signal calculated event-by-event. Two such distributions are shown on Figure 5-4, for 0 T and 1.5 T respectively. As expected, the distribution is much wider for the high field value. The Lorentz angle is then deduced from the differences of the central value of the fitted Gaussians between the 0 T run and the non-zero run using the following formula:

$$\theta_{lorentz} = \arctan\left(\frac{xdrift - x0}{1.88}\right)$$

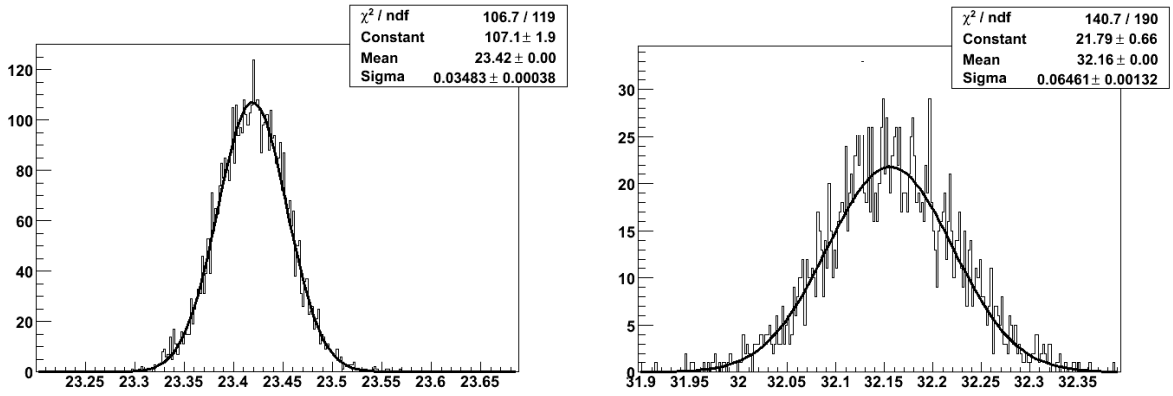

Figure 5-4 : Average position calculated event by event.

5.2.2. Lorentz angle versus magnetic and electric fields

A systematic measurement of the Lorentz angle with respect to the magnetic field was performed using a mesh high voltage of 400V and a drift high voltage of 550V. Each run used 2000 events and only took a few minutes with the DAQ running at 20Hz. Figure 5-5 shows the measured Lorentz angle (black squares) as a function of the B field in Tesla. The corresponding GARFIELD simulation is shown as green triangles and is in perfect agreement with our data.

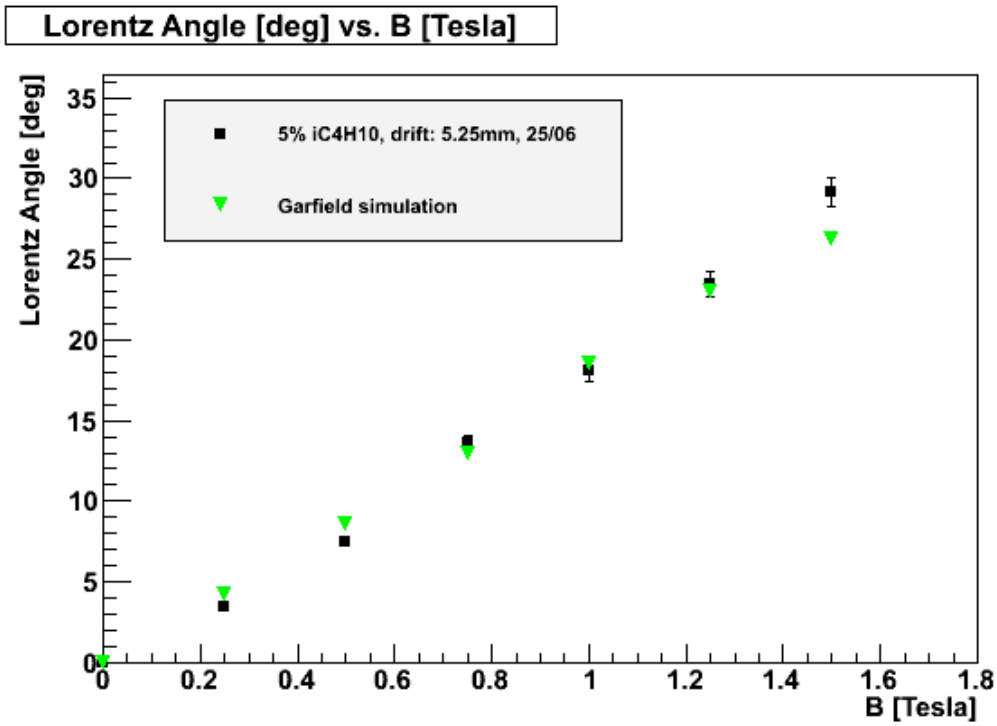

Figure 5-5 : Lorentz angle versus magnetic field.

Using the dipole at maximum magnetic field of 1.5 T, a scan in drift high voltage was performed. Figure 5-6 shows the Lorentz angle as a function of the electric field in the drift region. Black triangles are the data, red squares are the GARFIELD simulations, and both sets are again in excellent agreement. As expected, the Lorentz angle can be decreased to reasonable values around 15-20° using a large drift high voltage.

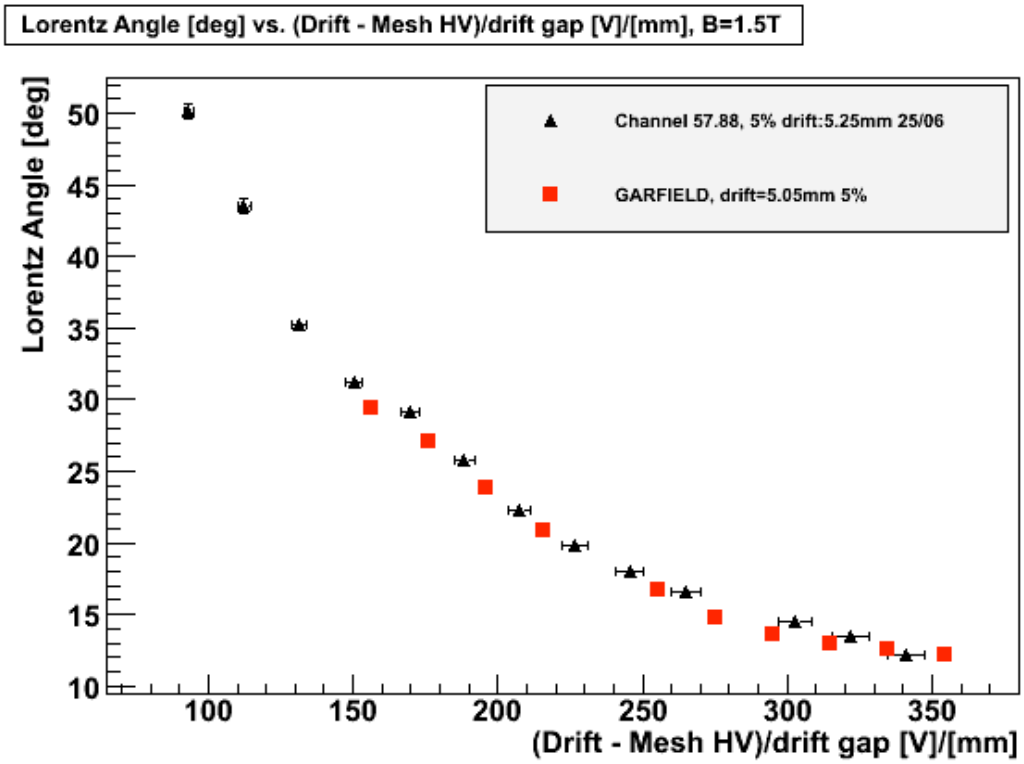

Figure 5-6 : Lorentz angle versus electric field.

This scan was repeated with a gas mixture of 90 % Argon and 10 % iC_4H_{10} and the results are shown on Figure 5-7 using the same units for the axis. The GARFIELD simulation does not reproduce the data as well as for only 5 % iC_4H_{10} but the agreement is still reasonable.

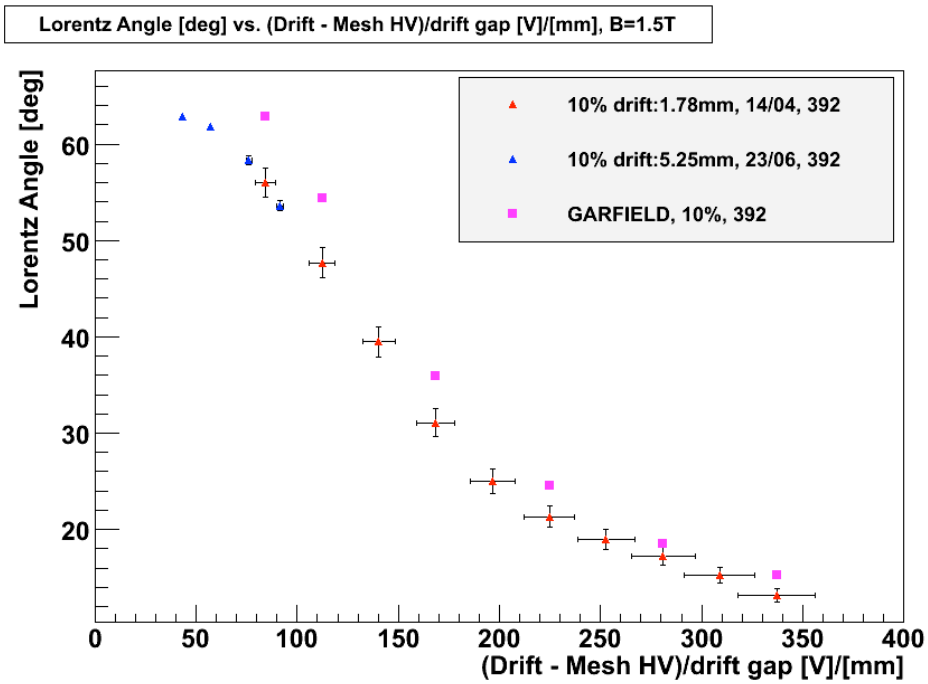

Figure 5-7 : Lorentz angle versus electric field with 10 % iC_4H_{10}.

5.3. Experimental Setup at Jefferson Lab

The tests at Saclay were performed using a small detector in a magnetic field of up to 1.5 T. Also, the detector was built using a thick PCB, which is not the kind of detector planned for the barrel. We decided to bring the test setup to Jefferson Lab in order to perform the same kind of measurement using a much larger detector built from a thin PCB in a realistic magnetic field of up to 4.5 T, provided by the DVCS.

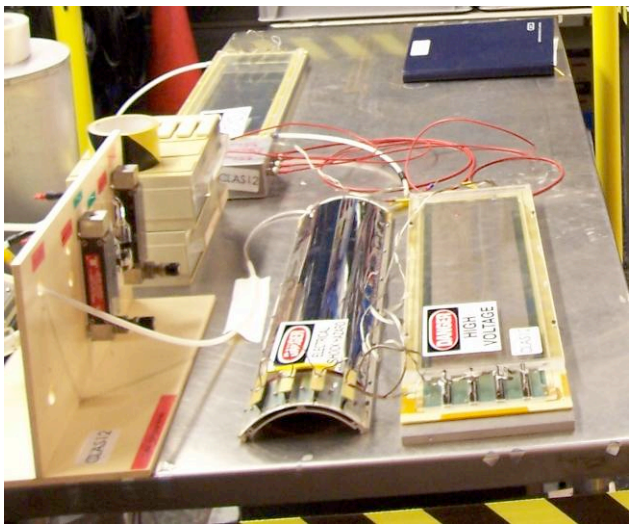

Figure 5-8 : View of the curved and flat detectors which were tested at JLab.

The detector we tested was the second version of the Micromegas thin bulk made at CERN. It is 500 mm long and 115 mm across with 288 strips at a 400 μm pitch. The stainless steel mesh was located at 128 μm from the strips. The drift electrode is an aluminized Mylar foil located at either 3.85 mm from the mesh electrode. The detector was filled with a pre-mixed gas mixture of Argon 90% and iC_4H_{10} 10%. The magnetic field was generated by the supra-conducting DVCS magnet, delivering up to 4.5 T.

The front-end electronics was replaced by AFTER chips this time [10], in order to accommodate the large number of strips. Also, this new electronics has much lower intrinsic noise, by about a factor 5 with respect to Gassiplex. The detector was connected to the electronics card by 4 flexible 80 cm-long circuit boards.

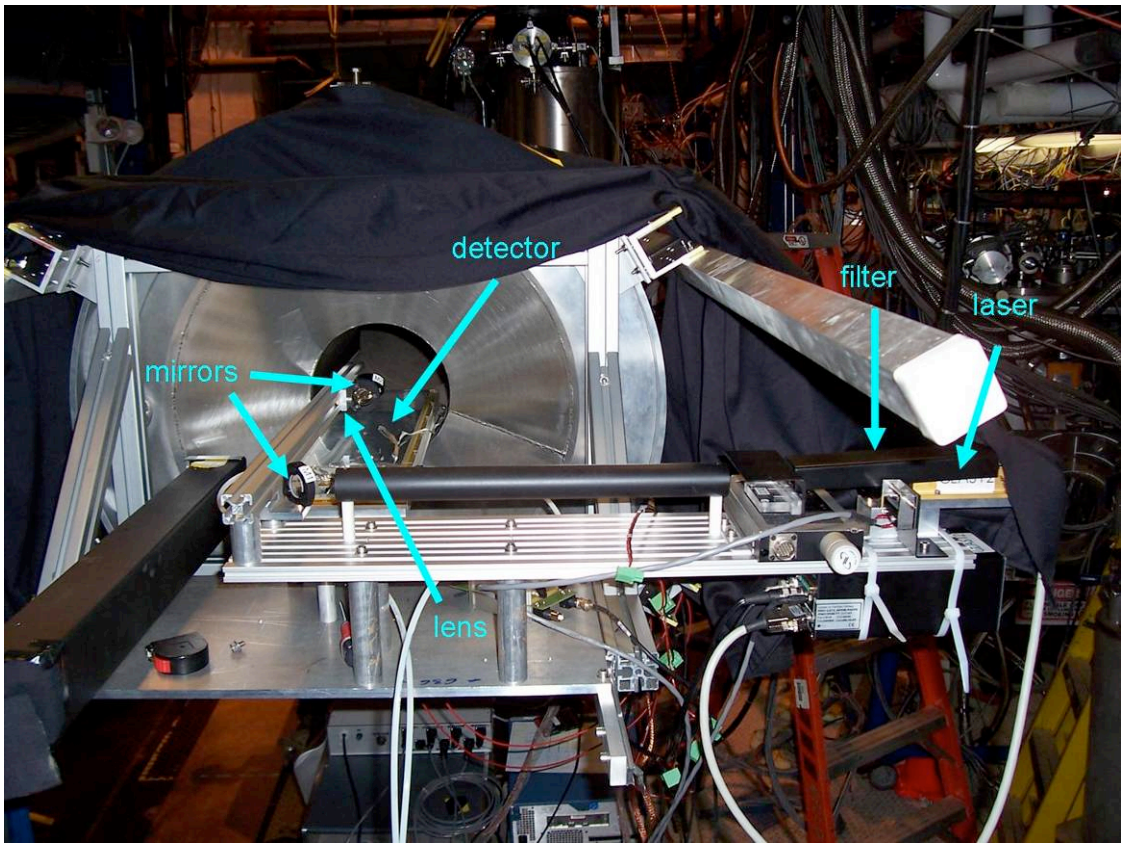

Figure 5-9 : A view of the experimental setup in CLAS.

The optical system had to be customized in order to bring the UV Laser beam inside the solenoid magnet, leaving the Laser itself at very low magnetic field. This was performed using a set of 45° mirrors and a focusing lens close to the detector to keep a small spot on the drift electrode.

The DAQ software we used is the test software from the T2K collaboration which uses the AFTER chips. The output is a binary file which was analyzed offline using a ROOT-based offline analysis software.

DC

5.3.1. Data analysis

The principle of the analysis is the same as for the Saclay tests. Thanks to the AFTER electronics, the full ion signal is pre-amplified, shaped and then digitized as a function of time for each strip. This is especially useful to take care of the pedestal subtraction which can be done with part of the time window, event-by-event. The integrated signal over a certain time window around the pulse gives us the recorded charge.

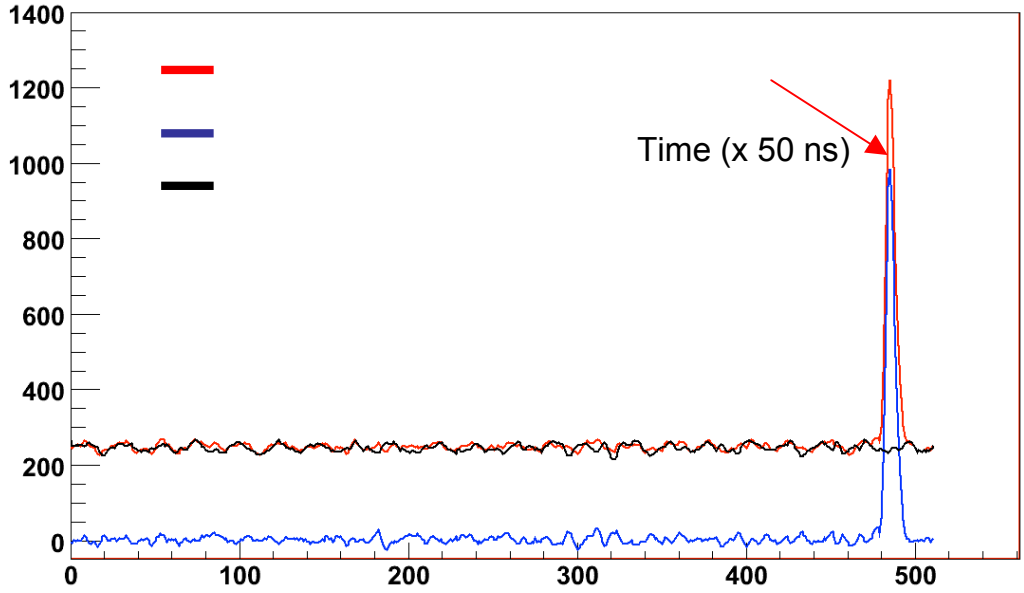

Figure 5-10 : ADC signal of ^{55}Fe on one strip as a function of time.

Once again, we extract the Lorentz angle from the average position of the drift signal calculated event-by-event. During the JLab tests, the mesh signal was fairly weak and for most runs, hardly noticeable. However, we observed another signal almost 20 times smaller than the "main" signal which had exactly the same shape than the drift signal. From its position, we came to the conclusion that it was some cross-talk likely due to the use of 2 flexible PCB cables linking the detector connectors to the electronics (which will not be the case in the final version where we will use only one flexible PCB cable).

B=0 T B=3 T

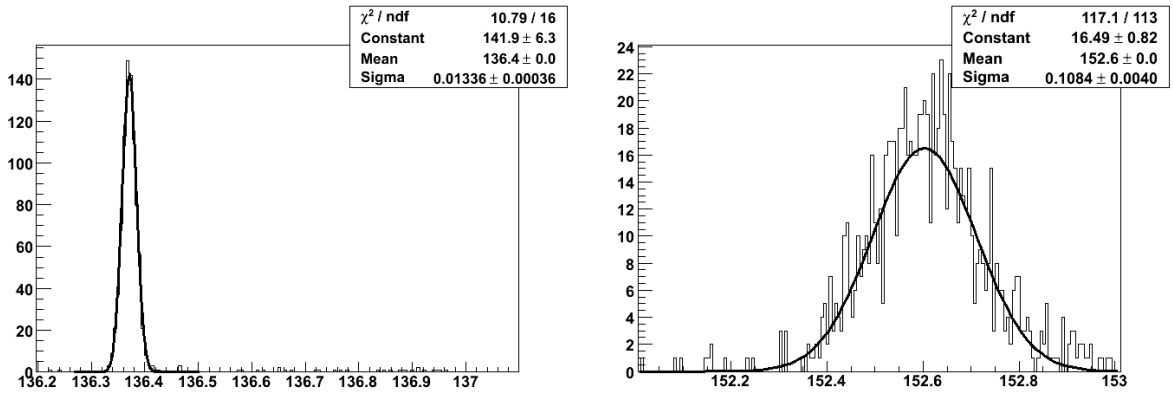

Figure 5-11 : Average position calculated event by event.

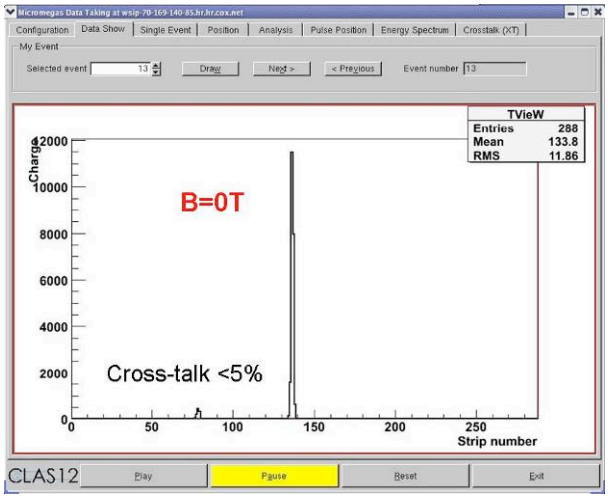

Figure 5-12 : ADC signal by strip. We can see the drift signal for B=0T.

5.3.2. Flex PCB cable tests

The detector is connected to the electronics by the means of flex PCB cables. The electronics noise increases with the distance between the detector and the electronics. Tests have been performed to measure the noise levels as a function of the flex cable length.
To study the noise induced by the flex cable length, we plot the distribution of the pedestal signal for one channel over the 512 time samples (Figure 5-10) and we compare the distribution sigma. As expected, the sigma of the Gaussian increases when we use a longer PCB cable (Figure 5-13), but this increase is not dramatic.

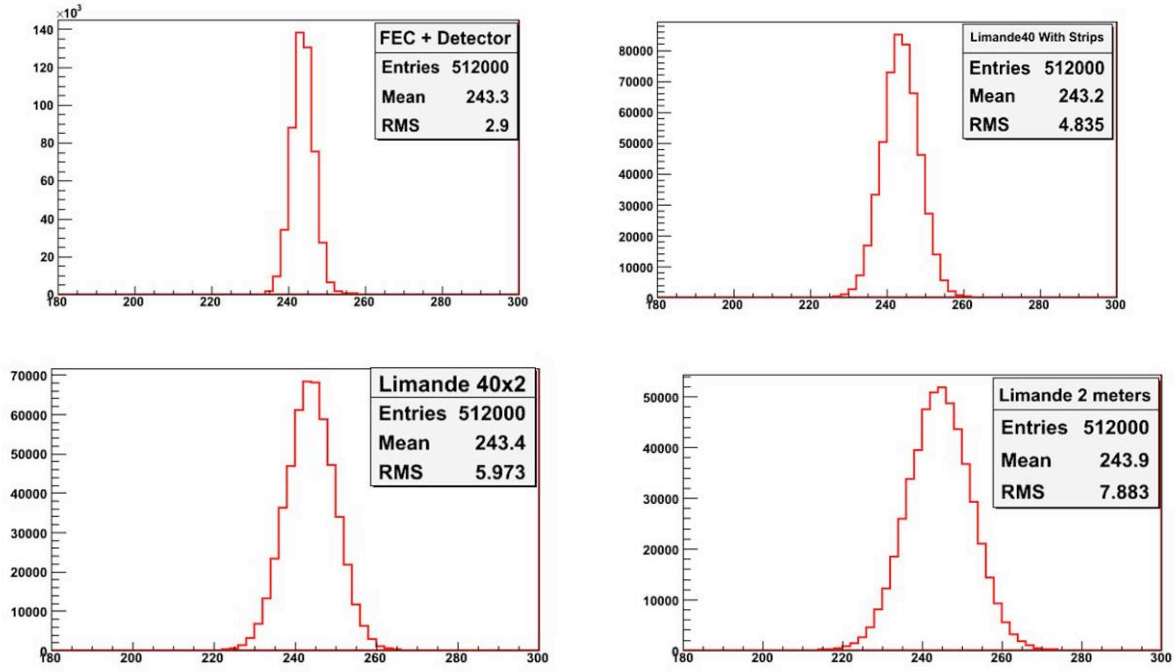

Figure 5-13 : Pedestal signal for one channel with different PCB cables lengths, from top left to bottom right, 0 , 40, 2*40, 200 cm.

Even with a 2 m cable, the noise is lower than 10 ADC channels. Given that the MIP signal is around 100 ADC channels, and also that we didn't optimize the noise reduction (the solenoid around the central tracker will provide an electromagnetic shielding), we see that the cables won't be an obstacle to the data acquisition.
The pedestal RMS can be further reduced by subtracting the coherent noise. The result is shown in Figure 5-14, where a linear behaviour with the flex length is observed. We also see that the noise induced by a 2 meter flex is roughly equivalent to the noise level coming from the detector itself.

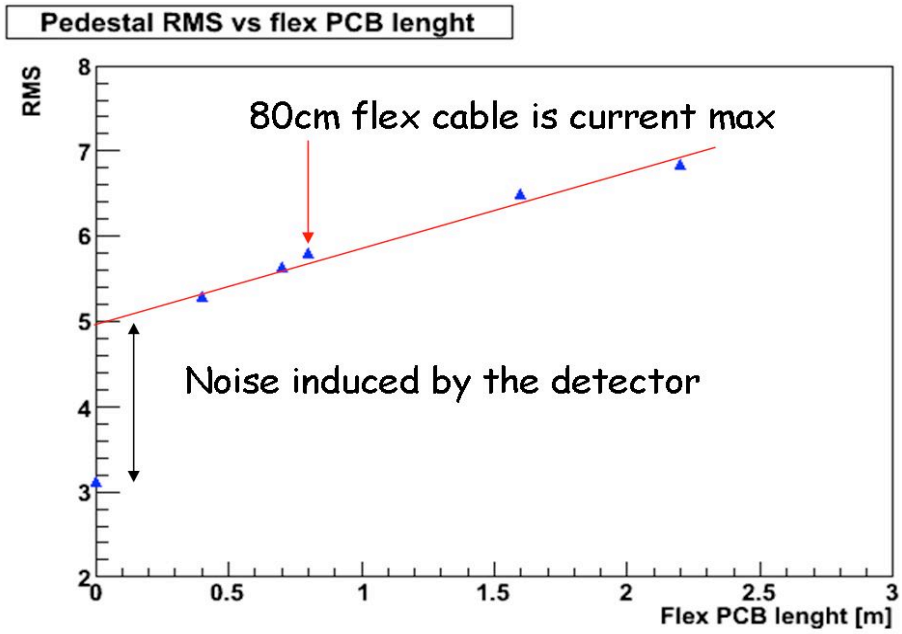

Figure 5-14: pedestal RMS after the coherent noise subtraction, as a function of the flex length.

5.3.3. Results

The measurement of the charge for each strip allowed to reconstruct the average position of the signal for each event, and therefore to estimate the Lorentz angle. Many measurements were performed at 1.5, 3 and 4.5 T, for different values of the drift HV (corresponding to electric fields between 40 and 700V/mm. The results are presented in Figure 5-15, and clearly show the possibility to decrease the Lorentz angle below 20° at 4.5 T, as required by the simulation in order to reach position resolutions of the order 200µm.

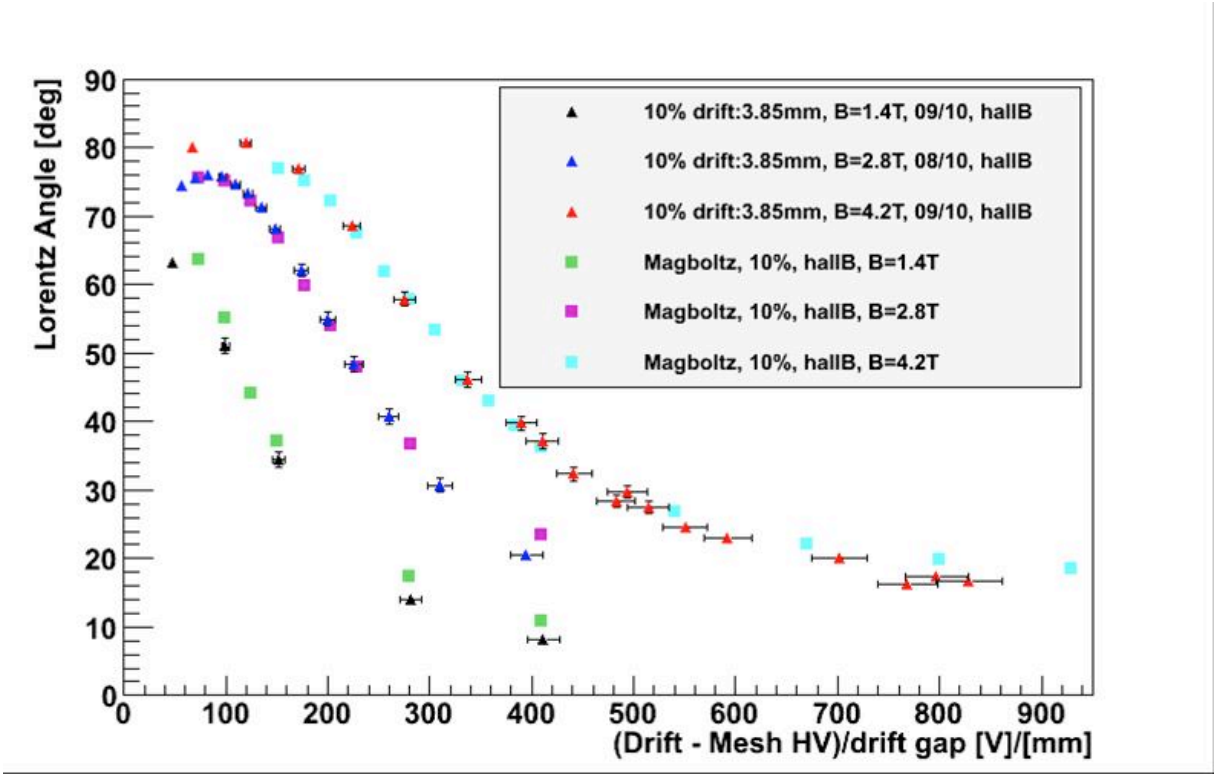

Figure 5-15 : Lorentz angle versus electric field for different magnetic fields.

5.4. Conclusion

The conclusion of the tests performed at Saclay and JLab was twofold: Firstly, we have validated the GARFIELD simulations, especially concerning the behavior of a Micromegas in a transverse magnetic field. Secondly, we have demonstrated that a flexible Micromegas detector of the length required for the central tracker can work in the CLAS environment with the proper electronics.

paddle

80cm flex

AFTER

electronic

6. Efficiency and spatial resolution studies

Trigger Unit

6.1. The cosmic rays test-bench

Cosmic rays are an efficient tool to extract the characteristics of the detectors in terms of spatial resolution and efficiency. We have developed and built a basic equipment, to detect cosmic particles and reconstruct their tracks.

Trigger

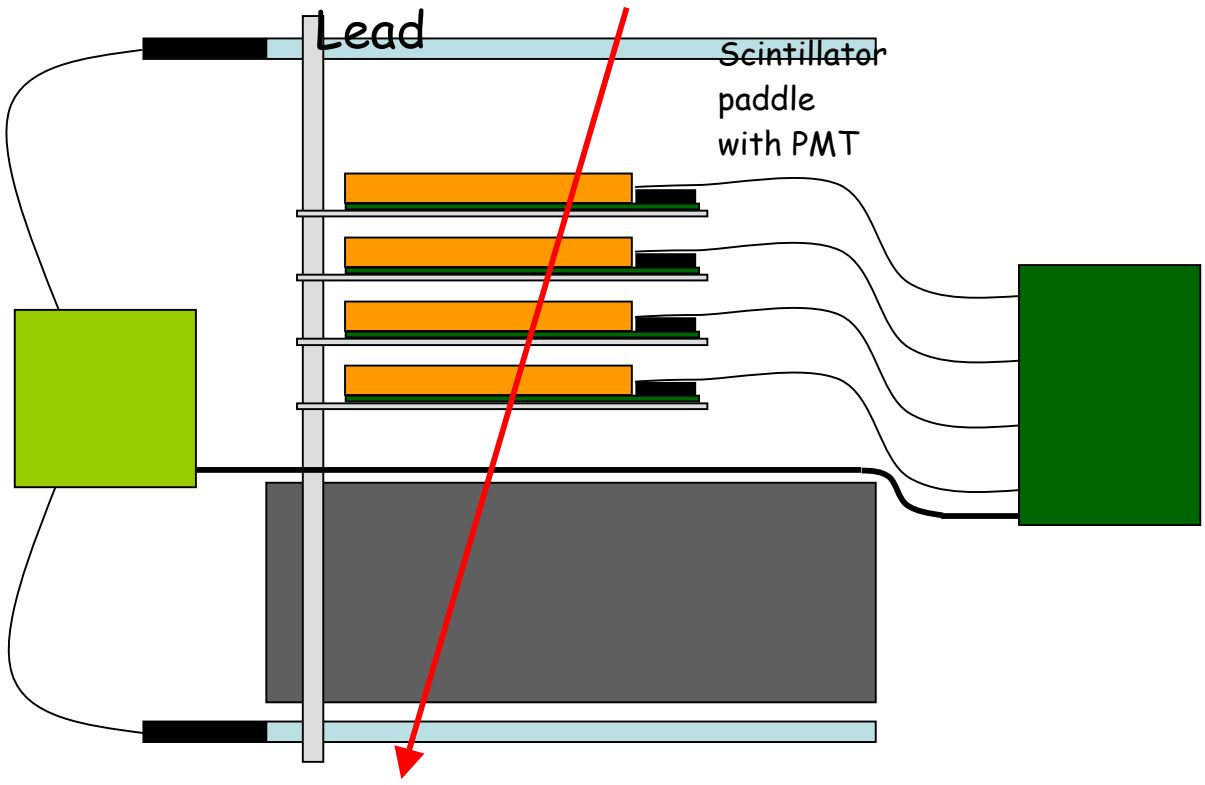

Figure 6-1 : Schematic view of the Saclay cosmic bench.

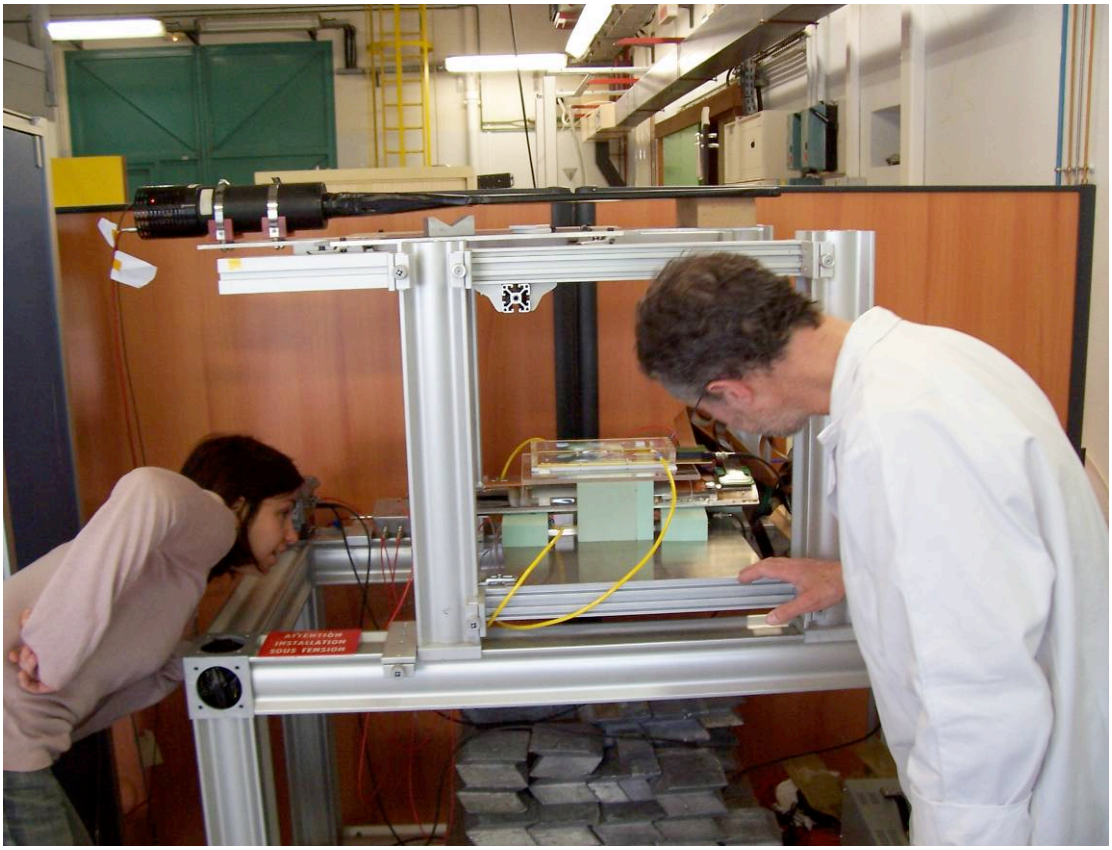

Figure 6-2 : Cosmic rays test-bench.

The device consists in two large scintillator paddles (800 mm x 200 mm x 10 mm) optically coupled to photomultipliers and placed at the top and bottom of the setup. They are used to generate the trigger. Three (sometimes four) detectors are positioned in between the scintillator paddles, having the external detectors to qualify the inner one. Lead bricks are piled up below the detectors just above the stop scintillator to select the most energetic cosmic rays, *i.e.* the minimum ionisation particles (MIPs). A schematic of the cosmic bench is shown on Figure 6-1 and a picture on Figure 6-2.
When a particle crosses the full setup, a trigger is generated from the coincidence of both scintillator paddles. The noise level is low, so the false coincidence probability is negligible.

6.2. Measurement

As for the measurements of the Lorentz angle at Jefferson Lab, we used the test software from the T2K collaboration for the AFTER chips as DAQ software. The raw data consists in a binary file, analyzed using a ROOT-based offline analysis software. The signal is shaped and digitized as a function of time for each strip. After pedestal subtraction, the signal is integrated and ADC counts are yielded (see Figure 6-3). The outputs processed through these data are the hit strips position and the charge.

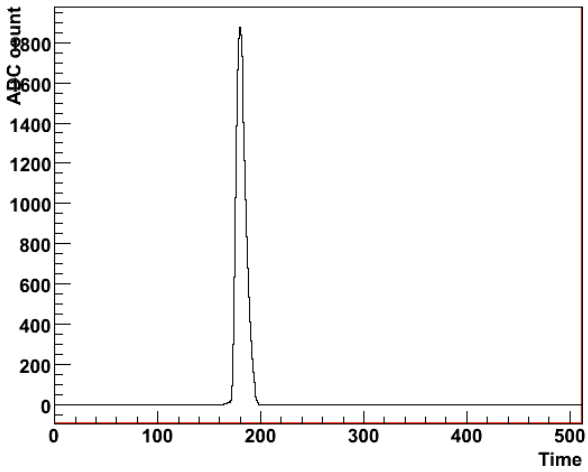

Figure 6-3 : ADC signal of a cosmic particle crossing the detector.

We have used two identical references MM detectors to characterize a third one placed in between them. They had a 400 μm pitch (strips being 300 μm wide). When a coincidence occurs, hits in all three (four) detectors are recorded and their position is calculated. The track can then be reconstructed and used to study the spatial resolution and the efficiency of the detectors. All three (four) detector planes had strips parallel to each other, so only one coordinate of the track was measured. Measurements were performed with thick as well as thin bulk Micromegas as well as flat and curved. The alignment of the three detectors had to be as accurate as possible and was achieved thanks to the standard support plates of the detectors. The situation got more difficult when aligning a curved tile with the two flat reference detectors.

6.3. Analysis

6.3.1. Hit position reconstruction: Spatial resolution

After data selection, the hit position in the detector is calculated using a weighted average over the strip charge. Typical charge distribution from muon hits spread over two to three strips. Due to the acceptance, particles with certain trajectories produce hits in only one or two detectors, such events are rejected. The cluster size (number of hit strips) of three strips is set as maximum. Figure 6-4 displays the evolution of the cluster size with the HV applied on the mesh and it comes out that any event with a cluster size larger than 3 strips can be considered as unreliable.

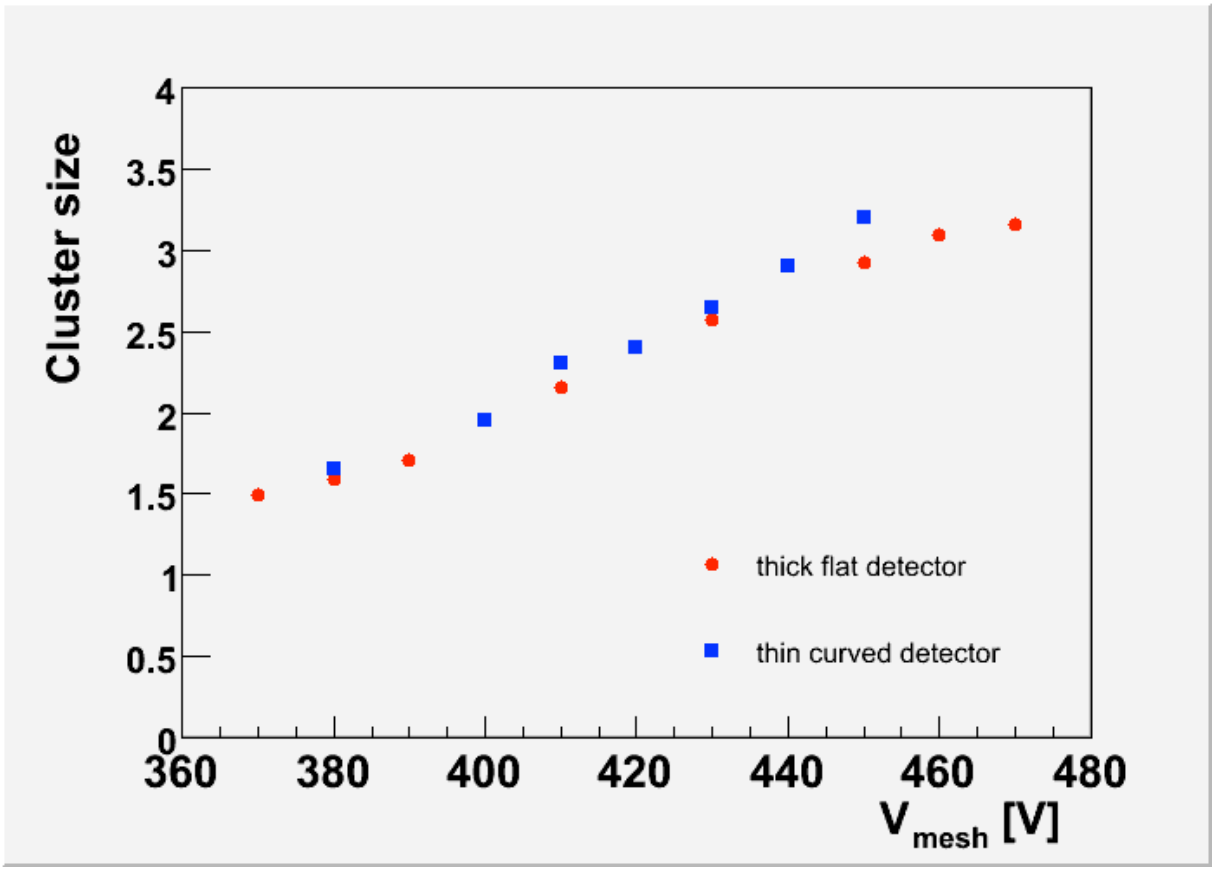

Figure 6-4 : Cluster size vs. mesh HV for a drift HV of 850 V. The pitch is 40 µm. The behaviours for thick flat and thin curved detectors are similar.

The approach followed in order to get an estimate of the detector resolution was to look at the σ of the residual distribution. The spatial resolution has been studied considering the residual between the reconstructed position of interaction in the medium detector and the extrapolated track position using the positions in the other detectors. The distribution of the residual can be fitted with a Gaussian line and an (over)estimate of the spatial resolution extracted. The real spatial resolution is indeed worsened by the misalignment of our detectors and may not be directly extracted using detectors with strips in only one direction.

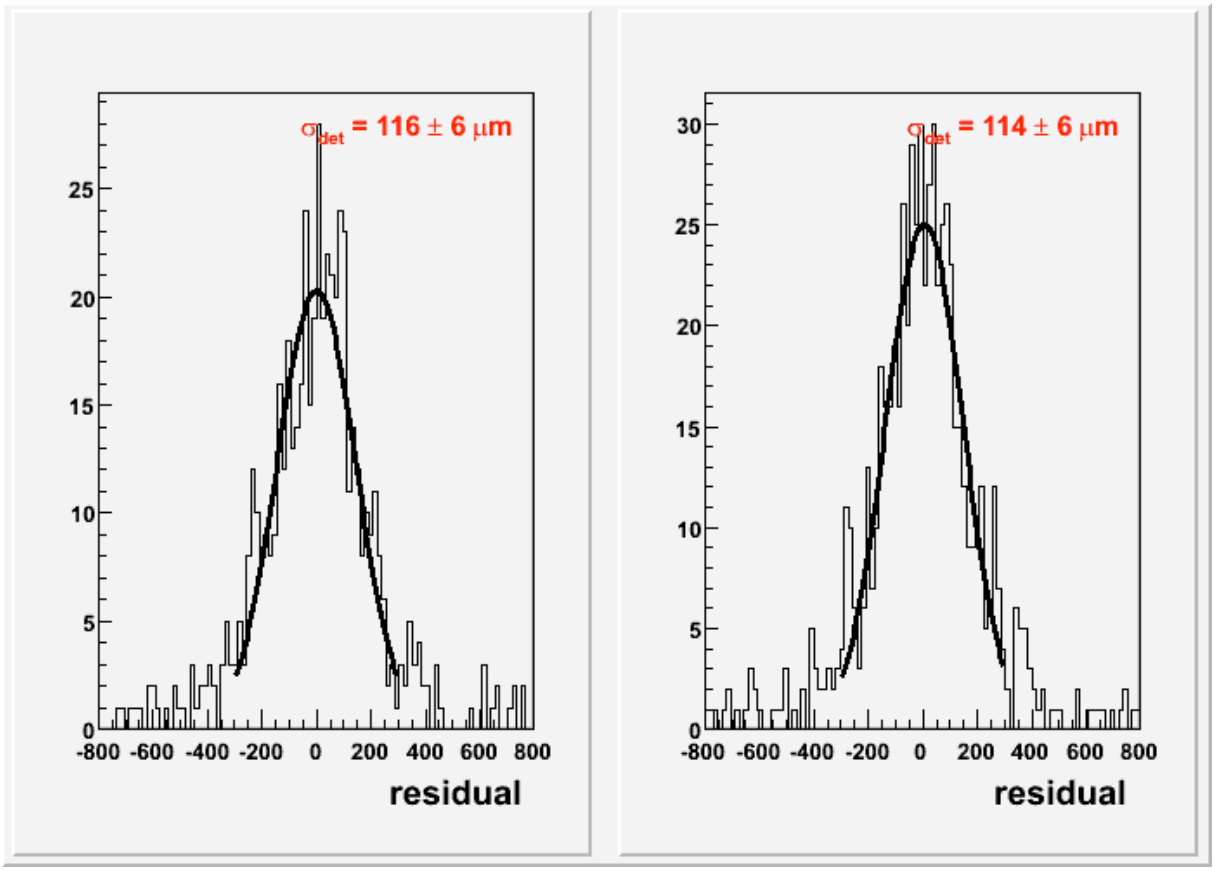

Figure 6-5 : Distribution of the residuals obtained simultaneously in a thick flat detector (left) and a thin flat one (right) using cosmic rays and 2 reference Micromegas detectors. Some misalignments of these reference detectors degrade the spatial resolution, but no differences are observed between thick and thin detectors. This is expected from the cluster size distributions, which are similar for both detectors.

The extracted resolutions are typically of the order of 115 ± 6 μm as displayed on Figure 6-5. Upcoming studies of the gas mixture may also improve the results. Finally, the cosmic ray telescope will be upgraded in the near future with full X and Y tracking capability, allowing one to extract the real position resolution.

6.3.2. Efficiency

To measure the efficiency, the same configuration setup was used. The efficiency of the middle detector is calculated as the ratio between the number of events in the middle detector and the number of events in coincidence in the top and bottom reference detectors. The efficiency has been studied applying increasing HV to the mesh of the detector, with a constant value to the drift electrode HV. The counting rates are calculated from data accumulated over 10-hour runs for each HV setting.

Figure 6-6 shows the resulting efficiency for a thick flat Micromegas and a thin curved one as a function of the mesh HV values. For a drift electrode HV of 850 V, the efficiency plateau is starting around 435 V with a smaller value for the thin curved Micromegas already a 97% can be obtained Further measurements are being performed with different prototypes and also increasing the drift electrode HV value to reach the set point needed in the CLAS12 magnetic environment.

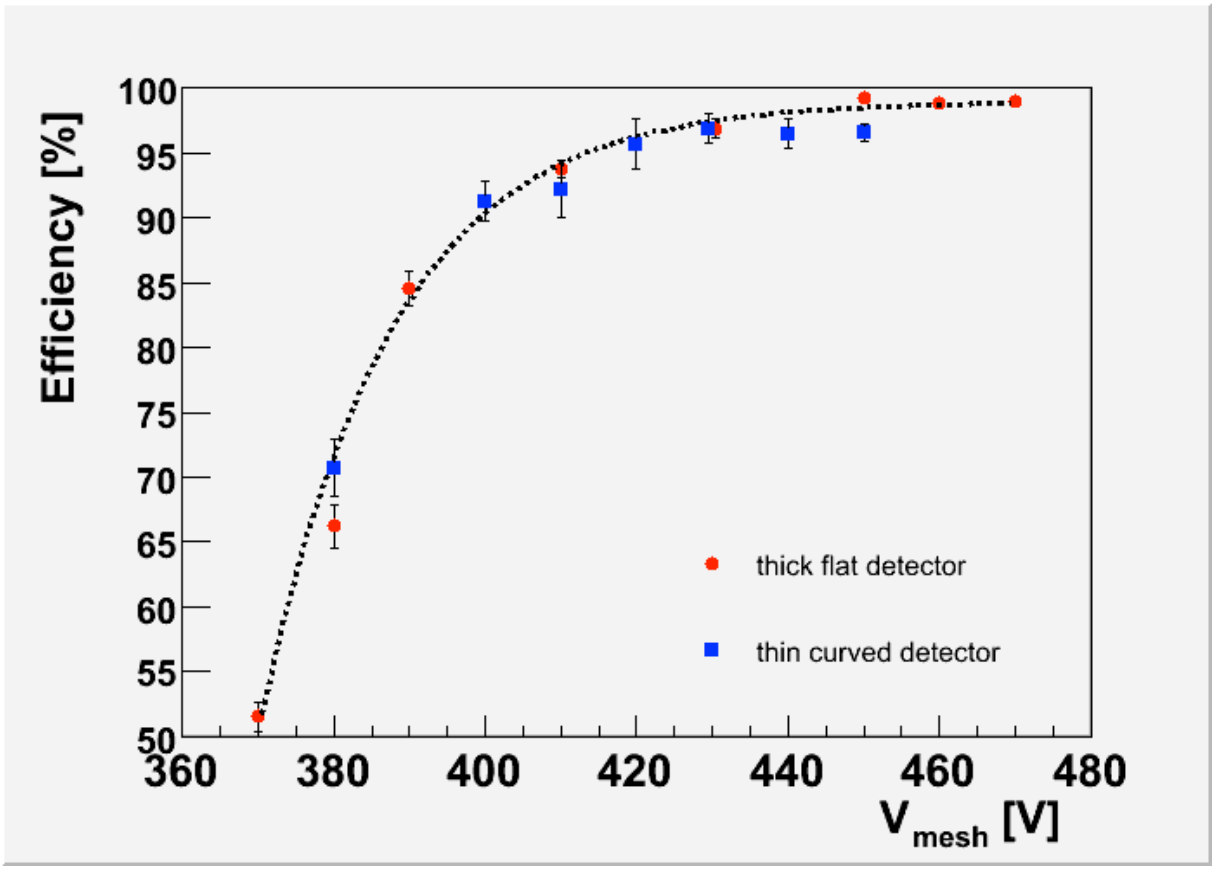

Figure 6-6 : Efficiency as a function of the high voltage applied on the mesh for a set value of 850 V applied to the drift electrode.

The efficiency to MIPs was also measured as a function of the drift electric field for a mesh HV of 420V. We observed a gain reduction of around 50% due to transparency reduction, going from Ed=1 kV/cm to 6 kV/cm. The resulting inefficiency was at most of a few %, probably limited by the focusing effect of the high drift field. Note that the magnetic field will partly compensate this effect and spread the signals on the pads. These considerations need to be further studied and tested.

6.4. Conclusion

Bulk Micromegas detectors were used in a cosmic bench in order to measure the spatial resolution and the efficiency for flat and curved detectors. Results show that the detector is within the specifications in terms of noise, efficiency and resolution. Further studies will be performed to study the effect of different gas mixtures on these parameters, as well as define nominal running conditions for efficient tracking.

Si layers

7. Tracking simulation (Gemc-Socrat)

7.1. Barrel Tracker

Twin µm layers

7.1.1. Design and implementation in Gemc/Socrat

Previous simulations [11] already showed that the best possible design for the Barrel Tracker would be to use a combination of Silicon and Micromegas. Indeed, Silicon alone suffer from a poor resolution in the polar angle θ, and the Micromegas alone do not meet the requirements in terms of φ resolution, as illustrated in Fig.7.1. Because of this, we directly implemented in Gemc a mixed setup, consisting of 2 double layers of Silicon (identical to the first layers of the original BST design) and 3 double layers of Micromegas, as shown in Fig.7.2. A double layer is made with 3 cylindrical detectors, each of them covering around 120° in azimuth. The characteristics of these layers are summarized in Table 7.1. The total number of strips is approximately 21,000, and the total radiation length is 0.25% per layer, e.g. 20% less than a 300 microns Silicon wafer.

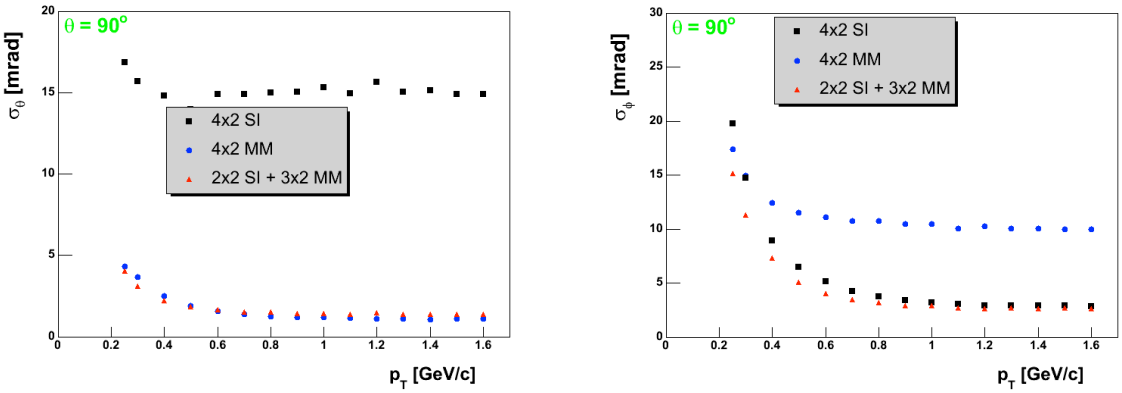

Figure 7-1 : Simplified simulations of the θ (left) and φ (right) resolutions for different Barrel setups.

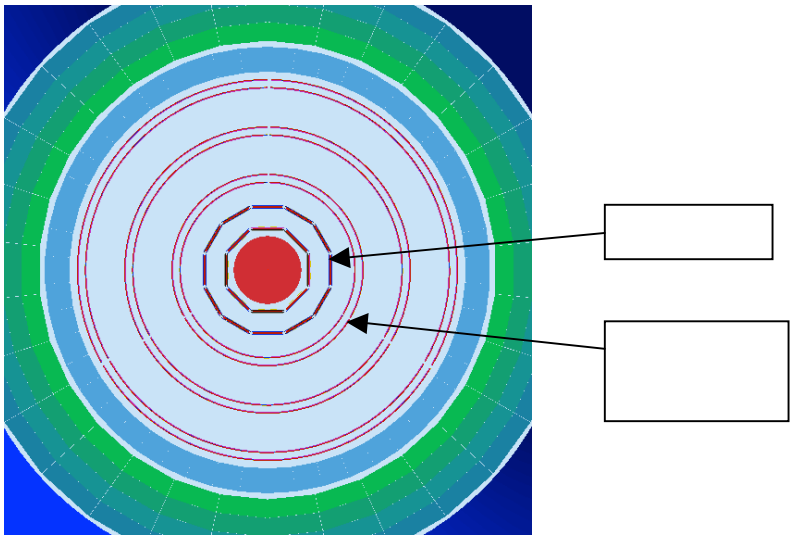

Figure 7-2 : Gemc display of the mixed Barrel Tracker, with 2 inner double layers of Silicon followed by 3 double layers of cylindrical Micromegas.

Layer	1X	1Y	2X	2Y	3X	3Y
Number of strips	694x3	852x3	1110x3	1277x3	1525x3	1696x3
Radius (mm)	110	120	170	180	230	240
Length (mm)	255.6	255.6	383.2	383.2	509	509
Pitch (microns)	300	300	300	300	300	300

Table 4 : Characteristics of each BMT layer. Each layer is build with 3 tiles, thus multiplying by 3 the number of strips.

A digitization routine has been plugged in Gemc, and the same design has been implemented in the reconstruction software, Socrat, to study the performance of the Barrel Tracker.

7.1.2. Tracking performance

- Efficiency

The acceptance efficiency is shown in Figure 7-3. Even if 5 measurements are theoretically enough to reconstruct a track, we require measurements in 7 layers out of 10, mainly to get a better rejection of fake tracks. We see that, even with relatively large dead zones (10 mm around each detector tile), the overall efficiency is 92.5%. This could be increased above 95% by using a 6 mm dead zone, as illustrated in Fig 7-4 (left). Thanks to the redundancy of this tracker, the inefficiency of the Micromegas only has a small impact on the overall efficiency, as shown in Figure 7-4 (right).

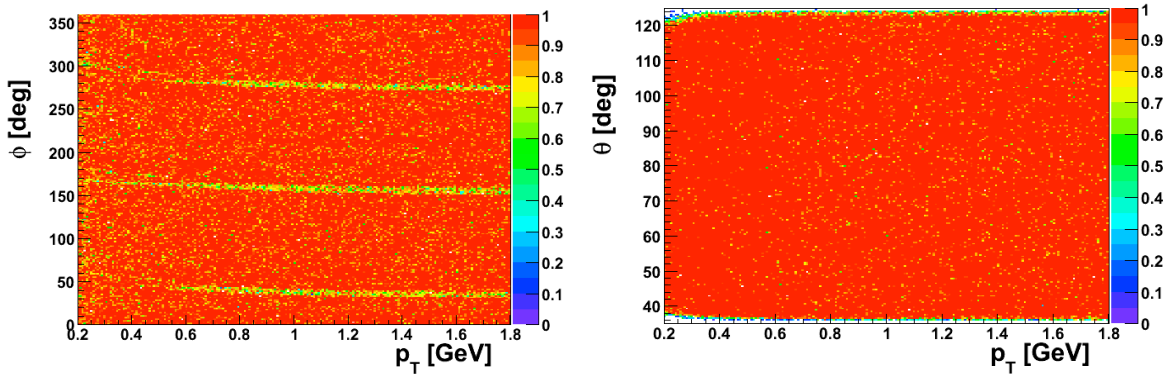

Figure 7-3: Acceptance efficiency of the Barrel tracker, in (p_T,φ) (left) and (p_T,θ) (right), requiring 7 out of 10 layers. The separations between the 3 tiles of the MM are visible on the left plot.

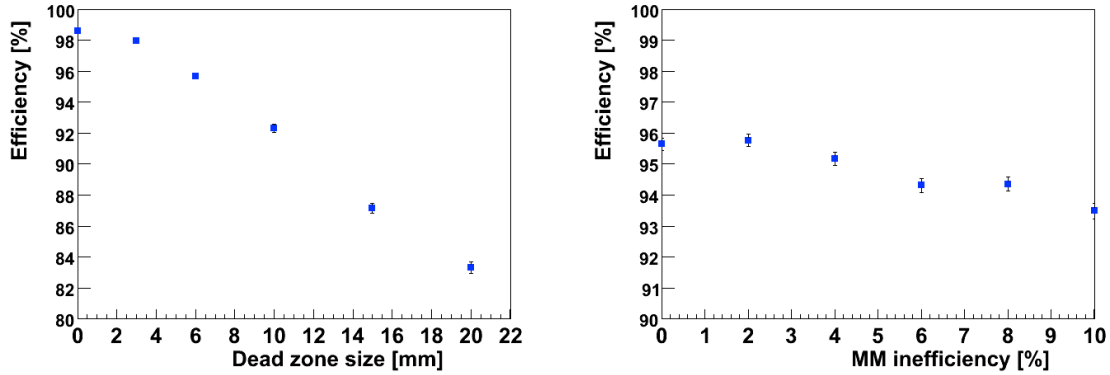

Figure 7-4: variation of the acceptance efficiency with the size of the MM dead zones (left) and the MM inefficiency (right). On the right plot, a dead zone size of 6 mm was assumed.

- Tracking performance and comparison with the BST

Once a track has been found, the Kalman Filter algorithm is used to fit its parameters. Figure 7-5 shows a comparison on the p_T and θ resolutions using the BST or the BSMT. As expected by earlier simulations, the presence of the Micromegas does not deteriorate the p_T resolution, but improve by a large factor the θ resolution, due to the strips at 90° (Y detectors).

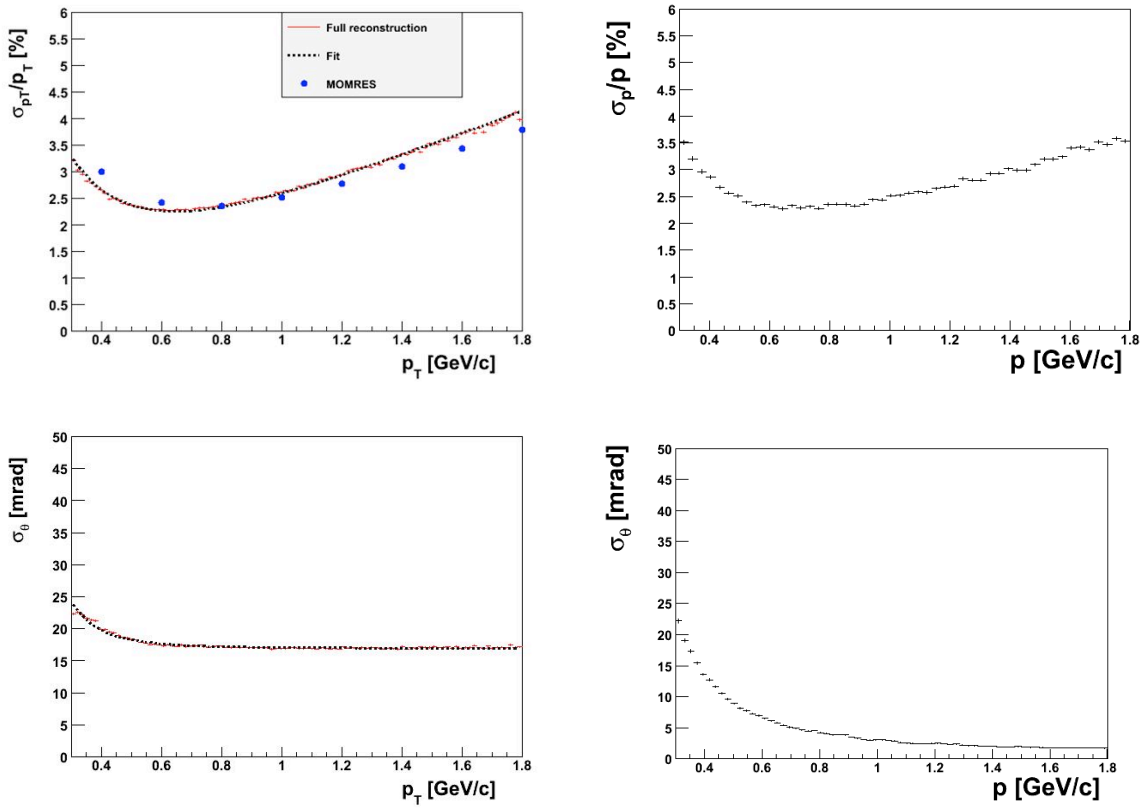

Figure 7-5: (top): p_T resolutions obtained with the BMT (left) and the BSMT (right); (bottom): φ resolutions obtained with the BMT (left) and the BSMT (right).

- Background rate

The background rate has been estimated in Gemc by generating events at the full CLAS12 luminosity that approximately corresponds to 62,500 beam electrons for a 132 ns time window. The results are detailed in Table 5. A significantly smaller rate is obtained for the Micromegas that appear to be almost transparent for the photons.

Si	Layer 1	Layer 2	Layer 3	Layer 4
e-/e+	3.9	3.7	4.3	4.3
photon	30.5	22.0	25.7	20.0
hadron	1.6	1.3	1.7	1.5
total	36.2	27.0	31.9	26.0

MM	Layer 1	Layer 2	Layer 3	Layer 4	Layer 5	Layer 6
e-/e+	1.27	2.73	1.14	2.92	1.70	3.68
photon	0.08	0.03	0.07	0.06	0.09	0.08
hadron	0.96	0.95	1.13	1.11	0.91	0.84
total	2.40	3.80	2.40	4.15	2.77	4.66

Table 5 : Background rates seen by the 4 Silicon layers (top) and the 6 Micromegas (bottom), in MHz**.**

7.2. Forward Micromegas Tracker (FMT)

7.2.1. Design and and implementation In Gemc/Socrat

As discussed in section 2.3, the FMT consists of 3 doubles layers divided in 6 sectors. Each sector is a piece of disk, with strips parallel to its edge. This design is therefore close to the design of the FST, having the advantage that all the readout electronics is all around the detectors, thus introducing no additional material in the acceptance. As a conservative estimate, we took a 10 mm dead zone around each sector of the FMT. This design has been implemented in the CLAS12 Geant4 package, Gemc, as illustrated in Figure 7-6.

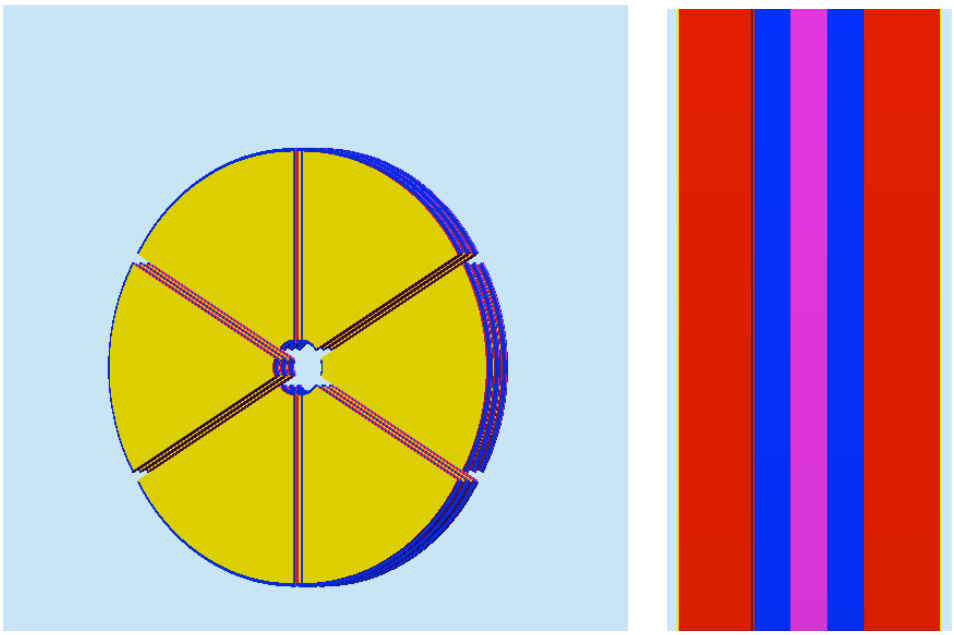

Figure 7-6 : (left) Gemc view of the 3 double layers of the FMT; (right): slice view of a double layer, showing its different elements: the support structure (pink), the PCB (blue), the gas (red); the micromesh, strips and drift electrode are too thin, and hardly visible.

As for the Barrel Tracker, the corresponding digitization routine has been plugged in Gemc and in Socrat.

7.2.2. Tracking performance and comparison with the FST

- **Efficiency**

The acceptance of the FMT and the FST are shown on Fig.7.4 (left) for electrons, as a function of their azimuthal and polar angles. The integrated efficiency is 79.7% (resp. 83.3%) for the FMT (resp. FST), and we see clearly that the size of the FMT dead zones is largely responsible for the difference. However, it is important to note that the Forward Tracker is not used as a standalone tracker, but in combination with the Drift Chambers. So what really matters is the track finding efficiency of the whole setup (Forward + DC). As the DC are made with 6 sectors, it is easy to "hide" most of the FMT dead zones in the shadow of the DC dead zones. Therefore, the track finding efficiency of DC+FMT is 71.2%, to be compared with 63.0% for DC+FST.

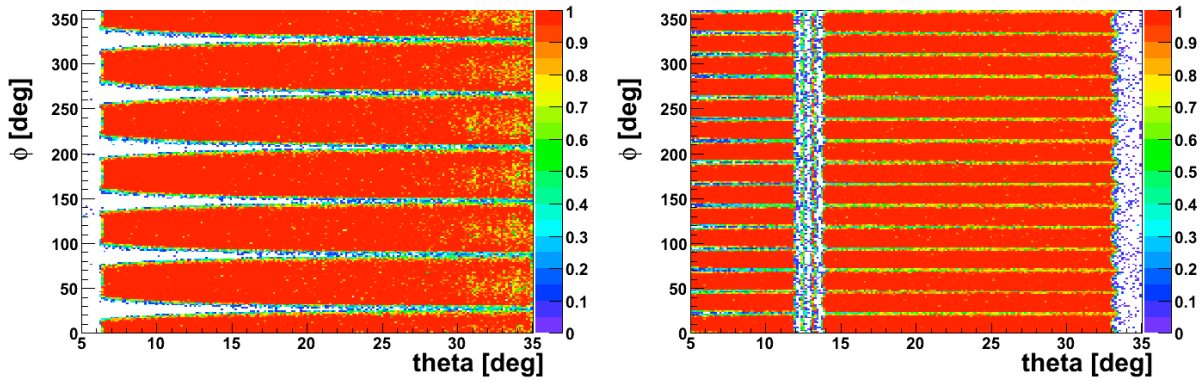

Figure 7-7 : Acceptance of the FMT alone (left) and the FST alone (right)

- **Resolution**

Once the track has been found, it is fitted using the Kalman Filter of the Socrat reconstruction code. To estimate the performance of the Forward Tracker, we use only tracks that can be matched with the DC candidates. The corresponding resolutions for electrons at 15° are then compared with the FST, and are shown on Figure 7-8. We see that both trackers have similar performance, and this means in particular that the large improvement of the vertex determination allowed by the combination DC+FST can also be achieved with the FMT.

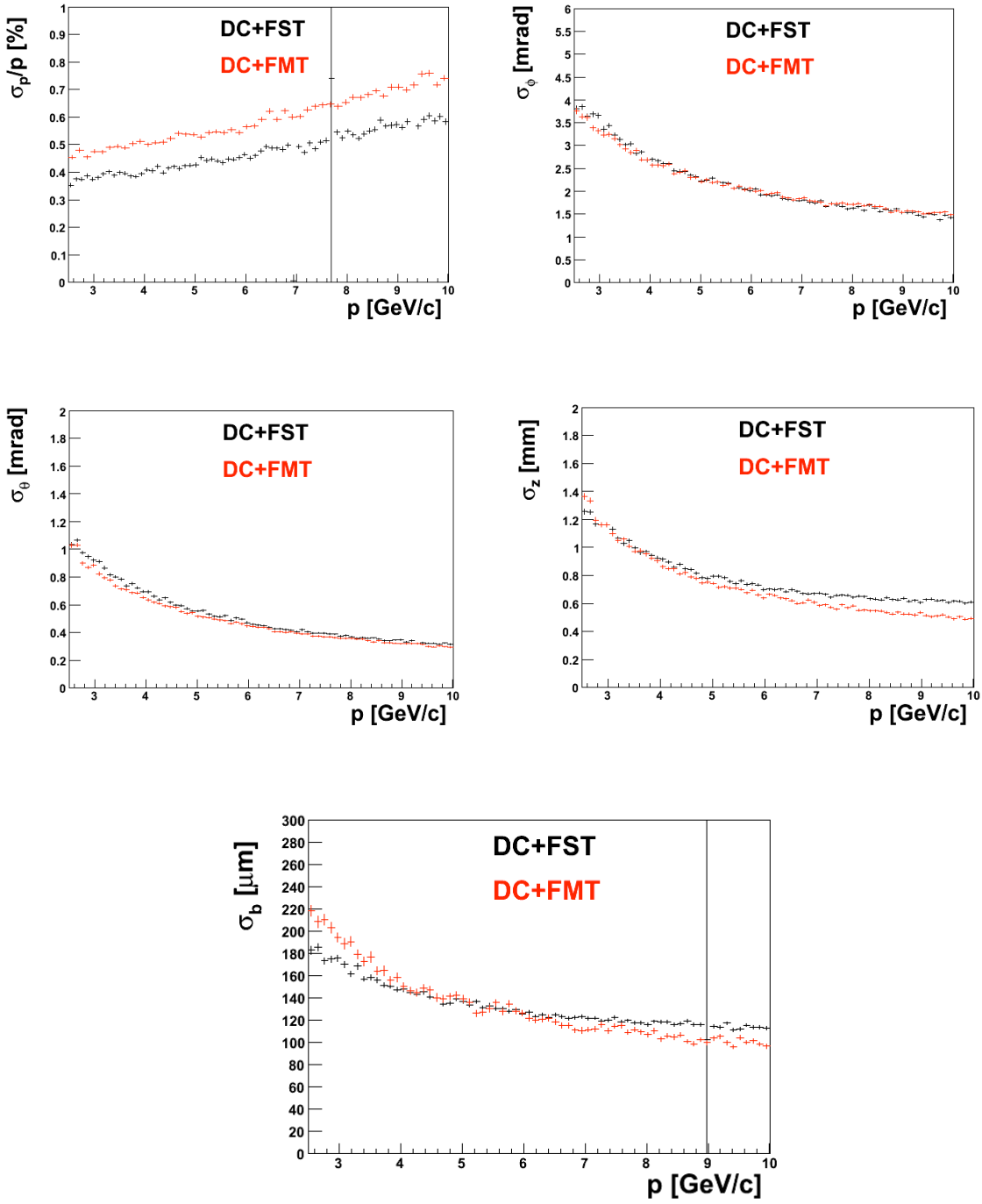

Figure 7-8 : Resolutions in momentum, azimuth and polar angle, longitudinal and transverse position of the vertex, for 15° electrons, using the DC+FST or the DC+FMT.

- **Background rate**

As for the Barrel part, the background rate has been estimated in Gemc by generating events at the full CLAS12 luminosity. The results are detailed in Table 6, and compared to the rates obtained in the FST.

We should first note that these rates correspond to the number of hits seen by the detector, this explains why the hadron rate is different in the FMT and in the FST. As for the Barrel tracker,

we also see that the total rate is significantly smaller for the FMT, again because the Micromegas are almost transparent for the photons.
In terms of number of hits per event, these rates are equivalent to approximately 2 hits per layer, if we assume a very conservative 132 ns time window, i.e. the same as for the FST. It has already been proved that the rate seen by the FST does not degrade the tracking performance, and in particular the matching of track segments with the DC. This conclusion remains a fortiori true for the FMT.

	Layer 1	Layer 2	Layer 3	Layer 4	Layer 5	Layer 6
e-/e+	8.9 (8.1)	6.4 (9.8)	6.1 (9.3)	7.3 (9.5)	6.3 (8.5)	6.2 (8.7)
photon	2.3 (17.2)	0.2 (13.7)	0.1 (11.9)	0.1 (10.9)	0.1 (9.2)	0.1 (7.9)
hadron	2.9 (0.5)	2.2 (0.6)	2.6 (0.7)	2.1 (0.6)	2.4 (0.5)	2.1 (0.5)
total	14.2 (25.9)	8.8 (24.1)	8.8 (21.9)	9.4 (21.1)	8.9 (18.3)	8.4 (17.2)

Table 6 : Background rates seen by the 6 layers of the FMT, in MHz. In parentheses are the rates estimated in the same conditions for the FST.

8. 8. Definition of a Front End Electronics

8.1. Introduction

This document is a first tentative definition of what could be the electronics for a Micromegas tracker for CLAS12. In this document, only the barrel cylindrical part has been studied. This should be revised by taking into account the specific needs for the forward part.

The architecture DAQ system is not studied in this document. Only the data flows in the front-end part of the electronics are studied.

8.2. Requirements from physics

The Overall Tracking detector is made of **3** doublets of each two Micromegas views (X and Y) for a total of **6 views**.

The total number of channels is N_{tot}**=10000** corresponding to N_{ch}**=1666** strip/view.

The overall physics events rate foreseen is ***PR***=20 MHz. Assuming a multiplicity of ***Mult*** = **4** strips/event per view, and a 100% efficiency for each view, we obtain a rate of:

$$R = PR \cdot Mult / Nch = 48 \text{ kHz/ strip}$$

The good events are validated by a L_1 trigger, build from data from other detectors and arriving to the tracker after a fix latency of maximum $L_1 = 4.5\ \mu s$.

At the beginning of the detector operation, it is assumed that the L1 trigger rate will be 10 kHz but will be upgrade to $F_{trig1} = 20$ **kHz**. We are going to use this last value for the following calculations.

8.2.1. Trigger acceptance Window

A hit detected by a view is considered to match with a trigger if its time is within a ***L1W*** window surrounding the (L_1 time – L_1 latency).

The probability to have a ghost hit on a strip during ***L1W*** is $R \cdot L_1W$

The mean number of ghost hits for a view is:

$$Nghost = R \cdot L_1W \cdot Nch$$

so that $$L_1W = Nghost / (R\ Nch) = Nghost \cdot 12.5ns$$

A good tracking capability has been demonstrated by simulation for ***Nghost = 8***, giving thus a L1 acceptance window:

$\underline{L_1W = 100\text{ns}}$

To achieve à 99.9% efficiency in this window, the peak-to-peak precision of the timing of each hit must be smaller than L_1W.
Assuming a Gaussian distribution for the timing error, this means a standard deviation of the timing smaller than:

$$\underline{\sigma_T = L_1W / 6.6 = 15 \text{ ns rms}}$$

For reference, a timing precision better than 9 ns are achieved routinely with the large Micromegas detectors of the COMPASS experiment [7].

8.2.2. Detector signal, Dynamic range

The duration of the signal delivered by the Micromegas detector depends on the gaz used and on its amplification gap. As a starting point we can use the same parameters as the one used for the design of the SFE16 electronics [12]:

Duration of the current pulse $\underline{d = 100 \text{ ns}}$

Nearly square shaped (80% due to ion current).

Mean Charge delivered for a minimum ionizing particle:

$$MIP = mip \cdot G$$

Where $mip \sim 20$ is the average number of electrons created in the conversion region (depend on gaz and on the width of the conversion gap).

G is the detector gain in the range of 5000 to 20000. Its setting is a trade-off between the S/N ratio and the spark rate.

$$\underline{100\text{ke-} < \mathbf{MIP} < 400\text{ke-}}$$

or $\underline{16\text{fC} < \mathbf{MIP} < 64\text{ fC}}$

It has been shown in [13] that setting a detection threshold to 0.1 ***MIP***, ensure a detection efficiency larger than 99% and allows to use center of gravity calculations to improve the position resolution. So that the detection threshold will be set

$$\underline{10\text{ke-} < Th < 40\text{ke-}} \quad \text{depending on } G.$$

To avoid noise triggering, the threshold must be set at a level larger than 6 times the rms value of the equivalent noise charge (***ENC***) above the baseline. This gives the maximum acceptable value for the ***ENC***.

$$\underline{1660 < \max ENC < 6660\text{ e-}} \text{ depending on } G$$

This implies than the MIP signal over noise = 60

The maximum charge to treat, corresponding to the highest end of the charge MIP charge distribution, is evaluated to

$$\underline{Q_{MAX} = 10 * MIP} \text{ (160 fC to 640fC depending on } G\text{)}$$

The MIP charge distribution follows a distribution resulting of a convolution of the primary electrons Landau distribution and of the Polya multiplication process distribution.

The total dynamic range to treat for a fixed gain of the detector is:

$$D_R = Q_{MAX} / ENC = 10 * MIP / (MIP / 60)$$

$D_R = 600$ corresponding to **9-10 bit** for a given G

2 bits more are required if the front-end has to treat the signal whatever G is.
This is not necessary, in case of the use of a **variable gain front-end** which can be configured to cover 4 ranges of operation (for example 160fC, 320fC, 640fC, plus a 80fC to make the chip usable for silicon detectors)

8.2.3. . Channel occupancy

For high rates, the discrimination efficiency is limited by channel occupancy. For a shaped signal duration t_{occ}, the corresponding inefficiency is given at first order by:

$$I_{OCC} = t_{occ} * R \text{ (for small } I_{OCC})$$

Keeping the inefficiency due to occupancy I_{OCC}<1.2% implies that

$$t_{occ} < I_{OCC} / R \Rightarrow t_{occ} < 0.012 / 48E3 \Rightarrow t_{occ} < 250ns$$

The pile-up events could be eventually recovered in the case of the knowledge of the signal shape.

8.2.4. . Analogue filtering

The filtering (analogue or digital) requirements are set by 3 constraints:

- Minimize discriminator channel occupancy (increase linearly with the peaking time, decrease with the order of the filter)
- Minimize noise (decrease as the square root of the filter peaking time)
- Minimize ballistic deficit (peak time or equivalent must be larger than 0.8 time the physical signal duration)

As the detector and the rates of this detector are very similar to those of COMPASS, the shaping requirements are nearly the same for this electronics to those used to define the front-end electronics for COMPASS [12]

To ensure t_{occ}< 250ns with a low ballistic deficit, a high order filter with a peak time (t_p) smaller than 100ns must be used [12].

Fig 8.1, Eq 1 and Table 7, extracted from measurements reported in [10], are showing the dependency of the measured Equivalent Noise Charge (***ENC***) for the AFTER chip (recently developed by Irfu for the Micromegas of the T2K TPC) with both the filter peaking time and input capacitance.

$$ENC^2 = \frac{\alpha^2 (I_{csa}) \cdot (C_0 + C_{in})^2}{t_p} + \gamma^2 \cdot (C_0 + C_{in})^2 + \beta^2 . t_p + D^2 \qquad (1)$$

In (1), α stands for the series noise contribution (depending on the input transistor bias current), C_0 is the intrinsic input capacitor of the preamplifier, C_{in} is the added capacitor at the preamplifier input, t_p is the peaking time of the shaped signal, γ stands for the 1/f noise contribution, β stands for the parallel noise contribution and D is the second stage noise contribution.

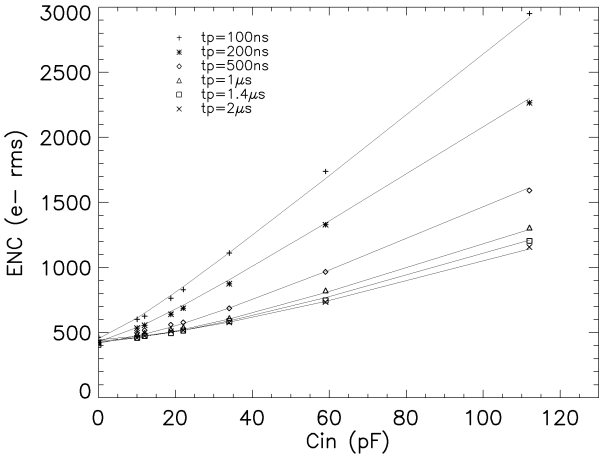

Figure 8-1: ENC versus input capacitance for different peaking times (120 fC range, I_{CSA}=800 µA). Symbols represent measurements, while lines represent fit results.

Parameter	120 fC	240 fC	360 fC	600 fC	Unit
α(400 µA)	246	250	253	254	$e\text{-}.ns^{1/2}.pF^{-1}$
α(800 µA)	197	198	198	194	$e\text{-}.ns^{1/2}.pF^{-1}$
γ(400 µA)	*6.6*	*6.6*	*6.9*	*8*	$e\text{-}.pF^{-1}$
γ(800 µA)	6.66	6.9	7.5	8.6	$e\text{-}.pF^{-1}$
β	0	0	0	0	$e\text{-}.ns^{-1/2}.pF^{-1}$
C_0	10	10	10	10	*pF*
D	385	730	1070	1760	*e-*

Table 7 : Extracted noise parameters (Quadratic expression).

In CLAS12, it is foreseen to move away the front-end electronics outside the detector acceptance through long flexes. For one strip, the expected capacitance of the detector including the flex connexion is estimated to 60-80pF. As shown on Fig.8.1, for this range of capacitances (for which the AFTER chip has not been optimized), and using a shaper peak time t_p =100ns, an ***ENC*** in the order of 2000 e- is measured. This must be cross-checked with measurements performed on Micromegas detectors connected to AFTER chips via long flexes.

For comparison, in the same conditions, a slightly smaller ENC (1800 e-) was measured for the SFE16 chip [12].

It looks like hard to meet exactly the ***ENC*** (1660e-) requirements for low (5000) detector gain operation. It is possible at slightly higher Gain (***G***> 6000) or if a higher occupancy is

acceptable. In this case, a shaper with 200ns peaking time permits to meet the requirement, but with an occupancy increase of ~ 80% (2%).

8.3. Common features to all FE solutions

8.3.1. Introduction: technologies, package, modularity

a) Technology Choice

For the choice of technologies, three options are possible, from the most to the less conservative:

- use an existing chip.

- use of a well known technology (AMS CMOS 0.35µm)
  - ++ faster design and low risk as the front-end part almost already exist,
  - ++ lower cost of development.
  - -- but moderate radiation hardness.

- use of a "new technology" (CMOS 130-180 nm range) :
  - ++ possible high radiation hardness (required ?).
  - ++ interest for the group to migrate to more modern technology.
  - ++ long term availability.
  - ?? better noise/power consumption FOM (?)
  - – more risks and longer development
  - -? Cost for prototyping.

b) Packaging, modularity

To make the manipulation, the test, we would prefer to use a packaged chip. To keep test operations simple, BGA should be avoided. The preferred packages are **QFP or QFN**.

To keep the package size reasonable, the ideal modularity is N_{CC} comprised between **32 and 64 channels / chip.** For the following calculation, we will take N_{CC}=64 as a worst case.

8.3.2. Power Consumption

The target power consumption is less than 5mW/ch.

8.3.3. Very Front-end part

For all the proposed architecture, the very front-end par could be the same. It is derived from those of the AFTER chip seen on Fig 8.2. It includes:

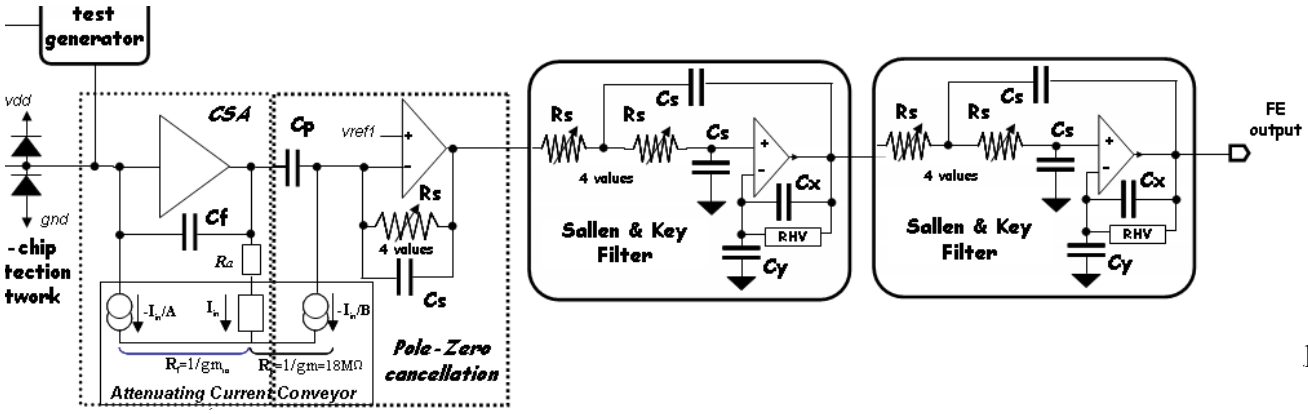

king

a) Test system

To reduce the need for external components, it is highly desirable to integrate all the test system inside the chip (including DAC, chopper and pulsing capacitor).

b) Input protections

The internal protection will be designed to reduce the need (or at least the size) of external protection. This is only possible if we assume that the mesh high voltage will never be continuously short-circuited to an anode strip.

c) Integral Non Linearity

For 0-2 MIP range: INL < 2%
For 2-10 MIP range: INL <5%

Figure 8-2 : Architecture of the front-end part of the channel.

8.3.4. Chip configuration & Control

The various chip parameters will be programmable through a serial slow control link. This can be the same link, SPI like, as the one used for AFTER or eventually I2C or JTAG.

8.4. Possible solutions for the Front-end part of the data acquisition

All the proposed solutions are deadtime free or are minimizing deadtime.

8.4.1. TDC based solution

a) Description and scaling

This solution is derived from the ones selected for the Micromegas tracker of COMPASS. It consists to integrates on a same chip a deadtime free TDC together with the Ampli-Shaper-Discriminator (ASD) front-end part.

- At the shaper output, the signal is compared to a threshold by a discriminator.
- An on-chip TDC, timestamps both the leading and trailing edges of the discriminator output pulse for each channel.
- These timestamps are stored in a hit buffer (double port RAM).
- They are moved in a readout buffer only if their timing is within a given ***W2*** around the L1 Trigger + Latency.
- The readout buffer (mainly a dual port FIFO) is used as a derandomizer.

Figure 8-3 gives for reference the architecture of the F1 TDC used in COMPASS which can be used as a starting point for the design.

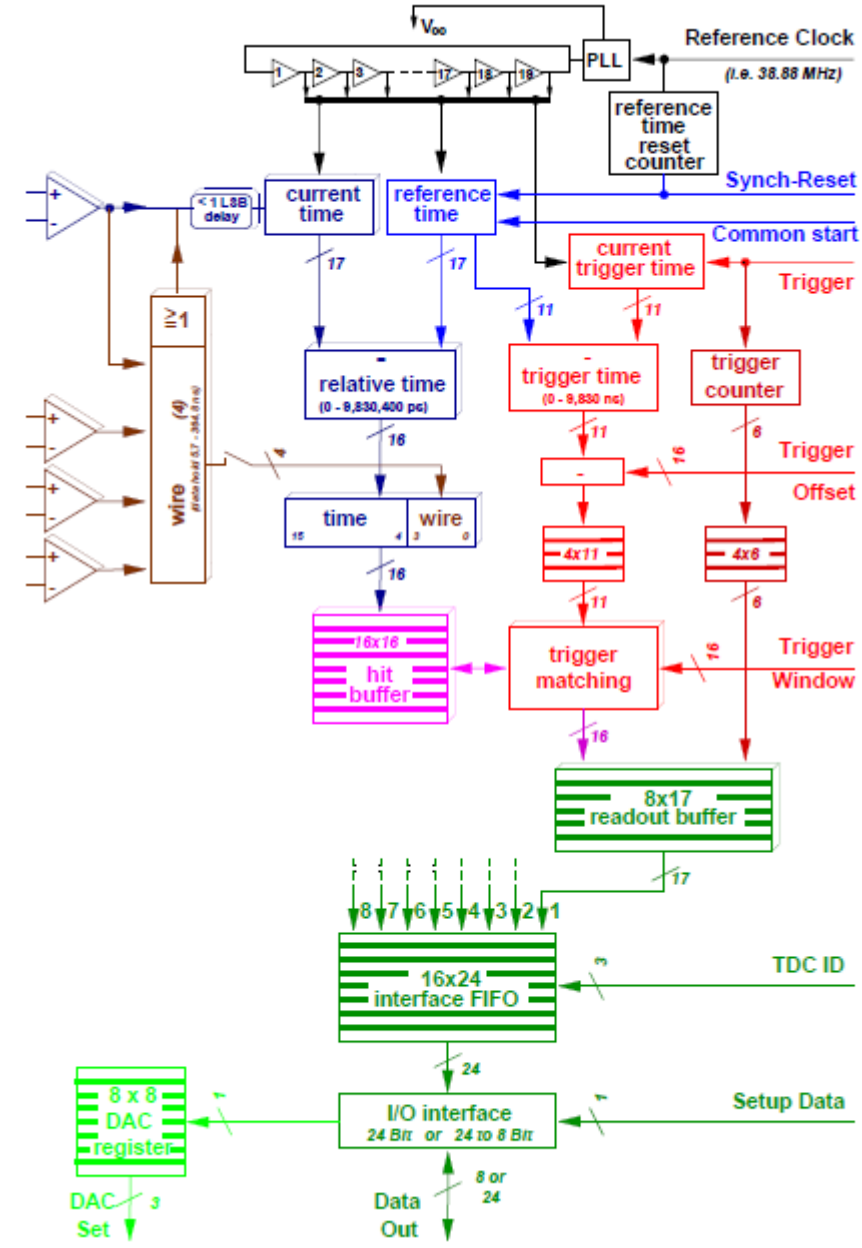

Figure 8-3 : Architecture of the F1-TDC.

The ***W2*** window has to be larger than the L_1W to take into account the timewalk effect due to the leading edge discrimination. ***W2*** ~ 2. ***tocc*** is a conservative value ensuring to catch the both edges.

The TOT (trailing-leading edge timing difference) is increasing [12], following a logarithmic law with the signal charge. The TOT can be used (it can be off-line) to perform a timewalk correction (down to 7ns resolution are obtained in COMPASS after correction), compatible with the required ***L1W*** acceptance window < 100ns.

The same TOT information is usable to perform centroid position calculation.

The TDC time step of 2 ns (0.6ns rms statistical error) seems to be sufficient and is easily achievable using combination of DLL techniques [14] and moderate clock speed counters.

The TDC depth must be several times larger than the L1 trigger latency of 5µs.
A depth of 14 bits (10 from a counter and 4 from the DLL) permits to cover a range of 32 µs.

The hit buffer and read buffer length have to be defined.

b) Data throughput

For each hit on a channel, ***B* = 6 Bytes** are required corresponding to 3 * 16 bits (16 bits of event identifier + 2* 16 bits for the leading and trailing edge timings).

For a given channel, assuming no noise hit, the rate of ghost hits inside the W2 window is:

***Nghost2/ Channel* = *R*.W_2** = *47 kHz . 1µs (**W2**= 1µs is very conservative)*
***Nghost2/Channel* = 0.05**
Nghost2/Chip* = N_{CC}*0.05 = 3.2 for a 64 channel chip.

The number of "real" hit inside the same ***W2*** (assuming a 100% efficiency of each view):

***Nhit2/ Channel* = *Mult* / *Nch*= 4/1666=2.4e-3**
***Nhit2/ Chip* = N_{CC} * 2.4e-3= 0.15**

The data throughput is then dominated by the ghost hits. It will be:

DT/Chip* = *B* * F_{trig1}* (Nghost/Chip+Nhit2/Chip)* =6 * 20E3*3.35 =402 *kByte/s

***DT/View* = 10.5 MByte/s**
***DT/Tracker* = 62.8 MByte/s**

The data flow can be reduced by a factor of 10 if an on-line timewalk correction is performed and if the corrected data are filtered by the L1W window.

c) Advantages and drawbacks of this solution

Advantages:

- Simple and proven architecture.
- Can deal with very large amplitude signals (they are clipped before the discriminator).

Drawbacks:

- The rate of false hits due to noise is **very** sensitive to common mode noises and parasitic signals, especially if the threshold is set to a low value. Moreover, the time distribution produced in this case does not follow any more a Poisson Law so that the buffers can loose a part of their ability to smooth the data flow. As the FE electronics is connected by long flexes to the detector, our electronics is potentially sensitive to this common mode effects. AS we experienced it with the COMPASS/Micromegas detectors, if this solution is chosen the grounding of the electronics + detector is particularly critical.

- The access of the charge spectrum is not immediate. The TOT <-> Charge transfer function must be calibrated.

a3

Ts=1/Fs

a2

8.4.2. Full Sampling solution

a1

a) Description and scaling

Δt= Ts.(a2-a1)/(a3-a1)

This second solution is based on the philosophy used in the APV-25 [15] chip.

Δt

It has been demonstrated that an accurate timing of pulses can be extracted using sampling of the shaper output signal [16]. For this purpose, at least 3 analogue samples are required (for example: 1 sample on the baseline + 2 samples in the leading edge, as shown on fig. 8.4), which means that the sampling period must be smaller than the half of the peaking time. For t_p=100ns, a sampling frequency of 20 MHz<***Fs***<40 MHz seems well adapted. Several algorithms can be used to extract the timing with a precision better than the sampling period, as the use of FIR filters or linear interpolation as shown on fig. 8.4. They can be used in or off-line depending on their complexity. The extraction of the charge is straightforward. Several methods may be used for this purpose: interpolation, FIR digital filter, largest sample.

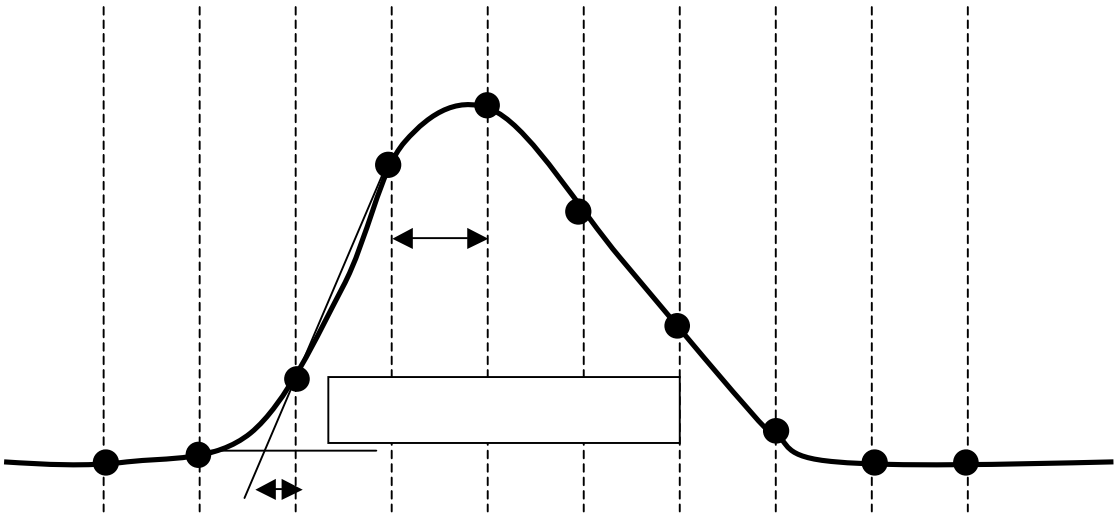

Figure 8-4 : Extracting time using sampling.

The front-end part of the chip is followed by an analogue pipeline made of switched capacitors (SCA). The output of the shaper is **continuously** sampled at a rate of F_S and stored in the pipeline. Useful data are marked if a L1 trigger arrives after the programmable latency ***L1***, and held in the pipeline until such a time that they can be read out. A FIFO holds the addresses of pipeline columns holding marked data. For each L1, a group of N_{cell} (typically 3-4) samples (columns) are marked and hold. Other data (which is not considered useful) is overwritten after a given time **> *L1*.**

. **For all the channels**, the analogue cells, which addresses are stored in the FIFO are read and sent to an (external) ADC through an analogue multiplexer (20 MHz).

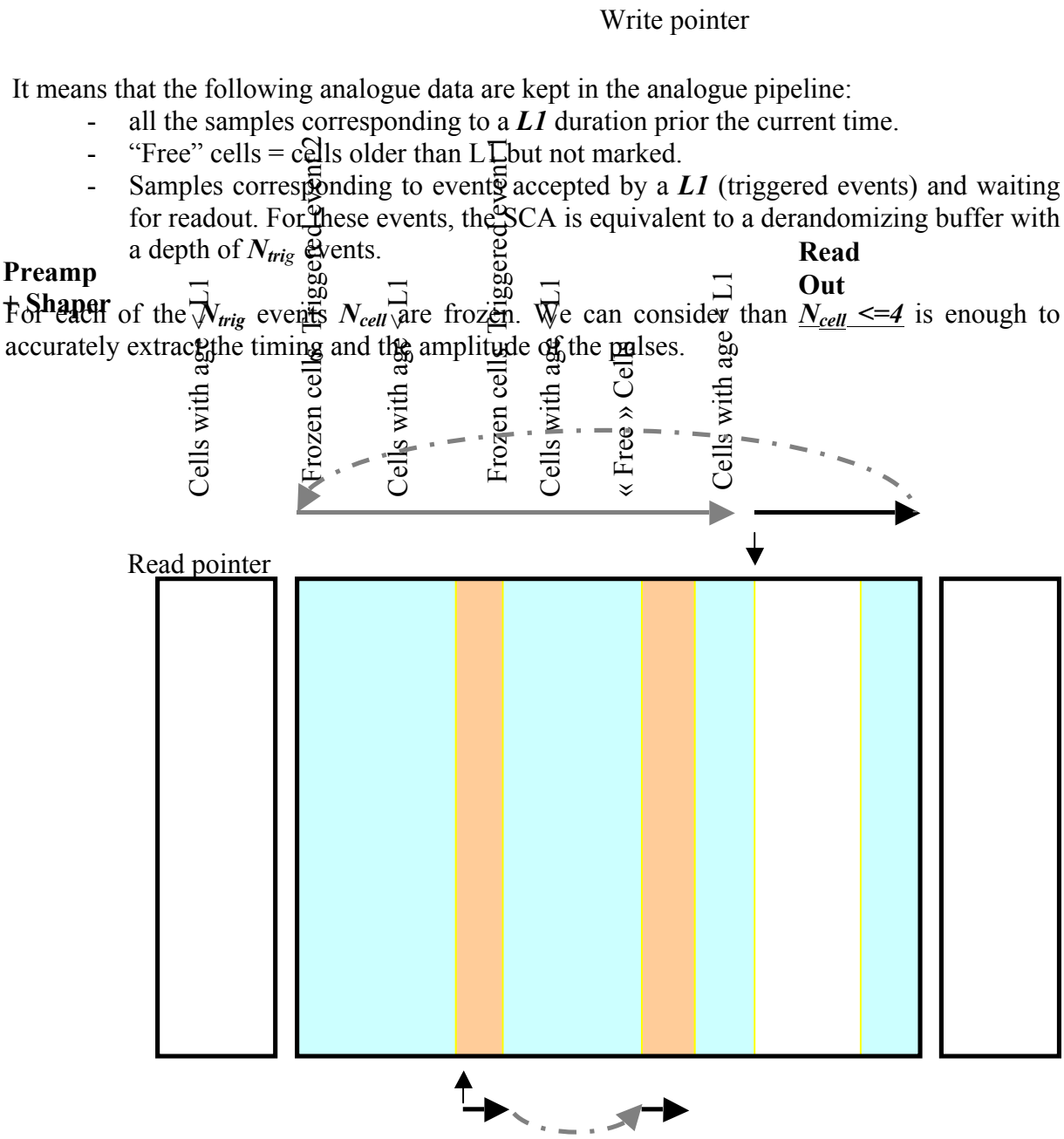

It means that the following analogue data are kept in the analogue pipeline:

- all the samples corresponding to a ***L1*** duration prior the current time.
- "Free" cells = cells older than L1 but not marked.
- Samples corresponding to events accepted by a ***L1*** (triggered events) and waiting for readout. For these events, the SCA is equivalent to a derandomizing buffer with a depth of N_{trig} events.

For each of the N_{trig} events N_{cell} are frozen. We can consider than $N_{cell} <= 4$ is enough to accurately extract the timing and the amplitude of the pulses.

Figure 8-5 : SCA chip with simultaneous RW operation with 2 trigger events stored (one being read).

The main difference with the AFTER chip [10] consists in that the data is still written in the SCA during readout.

Considering that 4 cells are read for each event and a readout frequency of 20 MHz:

For a 64 channel chip, the readout time is

$$t_{read} = 64 * 50ns * 4 = 12.8\ \mu s$$

For a 128 channel chip, like the APV, it is 25.6µs, 12.8µs if the read clock frequency is 40 MHz (possible with APV).

The Figure 8-6 gives the deadtime as the function of the number of triggered events which can be stored in the SCA (N_{trig}) for various values of the buffer occupancy (product Trigger rate * time required for read-out ($F_{trig} \times T_{read}$)).

For $F_{trig1} = 20$ kHz and $t_{read} = 12.5\mu s \Rightarrow F_{trig} * t_{read} = 25*10^{-2}$.

In this case, the deadtime is lower than 1e-3 if the number of buffered triggered event N_{trig} is larger than 4. It is still true for t_{read}= 25 µs and N_{trig} > 6.

To keep some margin we will conservatively take N_{Trig} **=9.**

The minimum SCA length can be calculated :

$Depth_{SCA} = L1 * Fs + Ncell * N_{trig}$ = 5µs * 25 MHz + 9 triggers * 4 cells =**161 cells**

Few extra cells may be required to give some extra margin of operation.

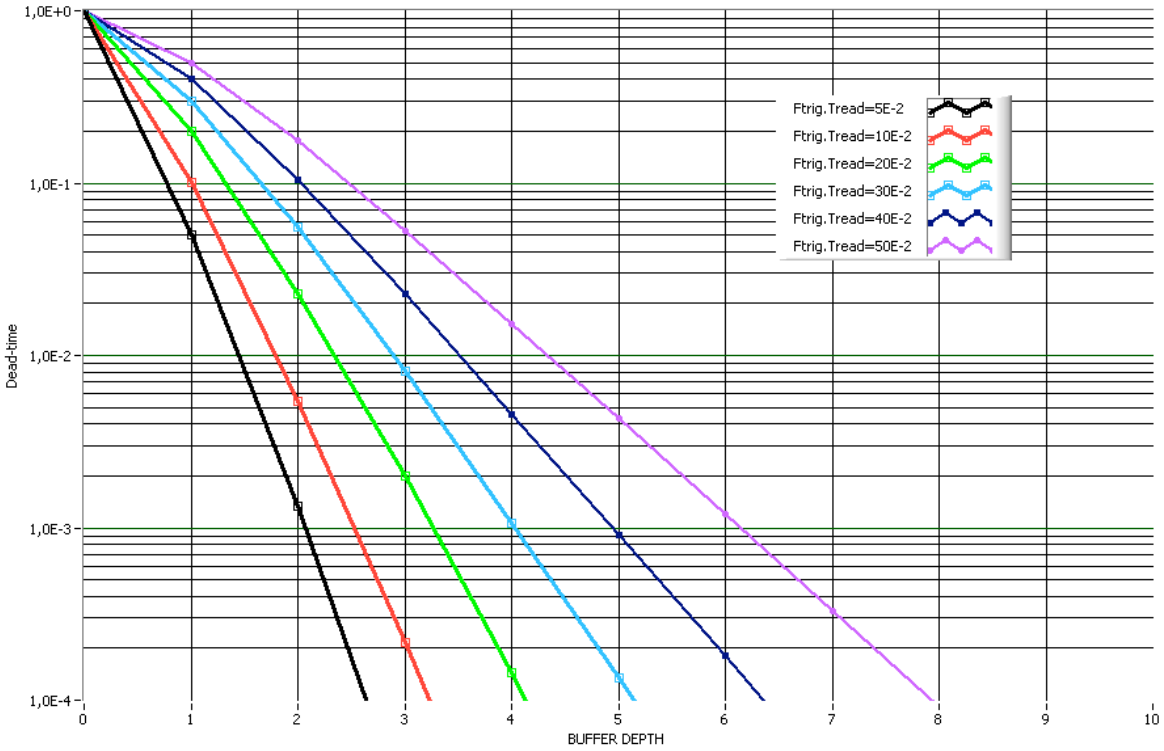

Figure 8-6 : Dead time as a function of buffer depth for various buffer occupancies.

b) Data throughput and related DAQ architecture

For each trigger, 4 cells are read and digitized for all the tracker channels. Considering ***Bs***= 2 Bytes are required to code each sample, the front-end data throughput is:

$DT_{FE} = F_{trig1} * N_{tot} * N_{cell} * Bs$ = 20E3 * 10E3 * 4 * 2Bytes = 1600 MByte/s

This huge amount of data must be reduced as soon as possible in the DAQ chain.
For this purpose, a first zero-supress operation can be performed as it is done for the electronics used for the GEM of COMPASS. At first, the common noise/baseline is extracted from all the channels of a chip. In COMPASS this is achieved using the median value for each sample on a chip. Then this common mode is subtracted for each sample and the result is compared to a threshold.

In this case, the number of ghost hits/ channel is defined by the W_3 window corresponding to the 4 samples:

$$Nghost3/\ Channel = R.W_3 = 47kHz * 4 * 50\ ns = 9.4E\text{-}3$$

The number of real hits is the same as the one for the TDC solution ***Nhit / Channel = 2.4e-3***.

With ***B2*** is the number of bits required for each hit on a strip:
Using 2 Bytes to encode a channel number, 2 Bytes for a trigger number and Ncell * 1 Bytes for the samples.
***B2* = 8 Bytes if 4 samples are kept for each event**

The amount of data for the wholetracker after zero-supress produced by each trigger is then:

$$N_{tot} * (Nghost3/\ Channel + Nhit / Channel) * B2 = 10E3 * (9.4e\text{-}3 + 2.4e\text{-}3) * 8\ Bytes = 950\ Byte.$$

This corresponds to a total data rate of ***950 Byte* 20 kHz = 19 MByte/s***

This rate can be quite easily reduced on-line by a factor of :
* ~ 2-3, if a simple algorithm is used to check if the second (or third sample) is not in the falling edge of the signal.

c) Is it possible to use the APV chip itself ?

- **For**
- Already existing chip. Proven architecture with GEM and RICH in COMPASS
- SCA length write, readout frequencies compatible with our requirements
- **Against**
- Limited availability.
- Not designed for large capacitance detectors: noise estimated to more than 2000 electrons (measure in progress).
- Only CR-RC shaping => large Tocc. For a 100ns peaking time, Tocc is nearly 1 µs:
    - 5% occupancy (which can be partially recovered by digital treatment on the samples).
- Limited dynamic range (to be studied).
- 128 channels / chip.

d) Advantages and drawbacks of this solution

Advantages:

- Proven architecture.
- The effect of baseline fluctuation due to parasitic signals and common mode noises can be strongly reduced by the common mode subtraction before zero-subtraction. This makes this architecture more robust.

Drawbacks:

Counter (Common to all channels)

Clock

Thres

- First zero-suppress stage absolutely required near the front-end chip to reduce the data flow.

discriminator

- Need for high-frequency ADCs at the front-end level.

synchro nizer

stop

8.4.3. Time Stamping & Sampling solution

Very Front-end

This solution is a mixture of solutions 1 & 2.

SCA manager

As shown on Fig. 8.7, each acquisition channel is composed of:

- a front-end preamplifier + shaping amplifiers.
- a discriminator.
- a mixed-mode analogue-digital buffer, with a depth of D_{MM} cells. Each cell of this buffer is made of a :
  - * digital memory to store a time stamp (N_{TS} bits).
  - * an analogue memory (made with a switched capacitor array)of N_{cells} to catch the waveform of the analogue signal over a window.

Depth=B

Depth=B

Buffer Manager

In each chip, a counter sequenced by the clock gives the coarse timestamp. The counters of all the chips are started by a common signal to synchronise all the counters.

Mixed-mode buffer

Time Stamp Memories

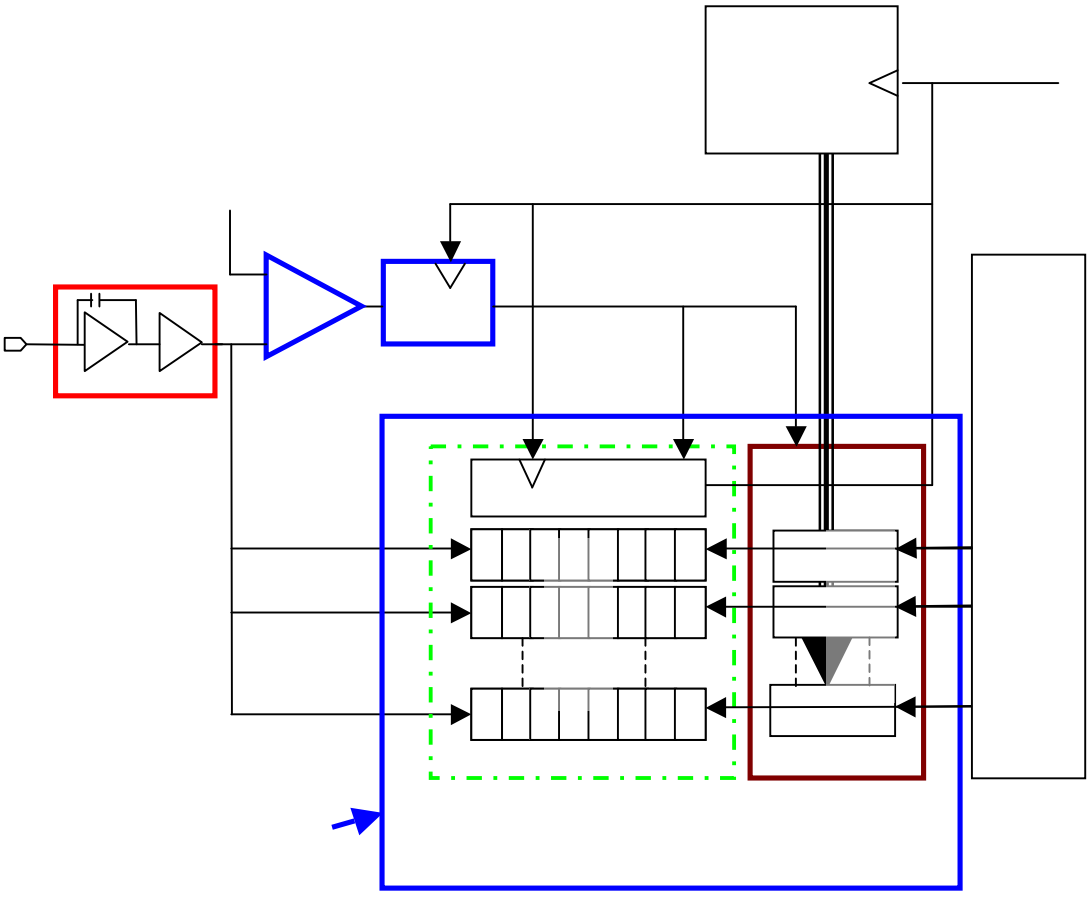

Figure 8.7: Time stamping + analogue memory solution. Schematic for one channel.

For each channel, the output of the shaping amplifier is sent both to a discriminator and to the analogue memory. The analogue signal is continuously sampled in the SCA part of the mixed mode buffer current cell at the F_{ck} clock rate. When the discriminator cross the threshold, its output, synchronised by the clock:

- store the timestamp, in the digital part of the current cell of the mixed mode buffer.
- stop the sampling in the current SCA and freeze its state.
- increment the mixed mode buffer pointer => start the analogue sampling in the next SCA.

Each cell of the mixed mode buffer contains then a coarse timestamp and a waveform from which the precise timing and the amplitude of the signal can be extracted online in an FPGA or offline.

Two solutions for the readout are conceivable. The first would consist in reading all the hits, the second one consist in reading only the events with timestamp within a window around the trigger. For both solutions the analogue data of all the channels of a chip are multiplexed towards an external ADC channel whereas the digital data (channel number + coarse time stamp) is multiplexed through a digital bus towards a FPGA. For the following data flow estimations, we have considered that N_{cells}= 4 samples are read back for each event and we have assumed that all the digital data is transferred during the time required to digitize the N_{cells} samples.

a) Triggerless front-end chip

In this case, for one chip (with 64 channels), the number of samples to be converted per second is given by:

$R * N_{CC} * N_{cells}$ = 48E3 * 64 * 4 = 12.28 MSample/S which is achievable with modern ADCs. It can be divided by using more than one ADC for one front-end chip.

A mixed-mode buffer cell is released only after readout. The mixed-mode buffer is used to derandomize the data rate. So that, a monte-carlo simulation of the deadtime is required to define the length of the mixed-mode buffers as a function of the ADC frequency.

In this architecture, a FPGA first gathers both the digital information (coarse timestamp + channel number) and the digitized waveform samples. This FPGA must then filter the data using the L1 trigger and the coarse timestamp to reduce the data flow. Data flow calculations have still to be done in this case.

This solution clearly minimize the work on the front-end ASIC to increase the one required on the following FPGA.

b) Selective readout

Like in the solution 1 (TDC), when a trigger occurs, the event is moved inside a readout buffer, only if its raw timestamp is within a given ***W3*** window around the L1 Trigger + Latency, otherwise its corresponding cell in the mixed mode buffer is released. In this solution, the digital part of the chip architecture is very similar to the one of the standard multihit TDC, excepted that the analogue data have also to be multiplexed towards the ADC.

The ***W3*** window is much smaller than the ***W2*** window used for the TDC solution. The ***W3*** window size is set by the time walk effect on the leading edge of the signal. ***W3*** = 2 * t_p ensures that all the signals corresponding to the trigger are in the window with a wide margin of security.

Assuming a 64 channel chip and ***W3***= 200 ns, we can perform rate calculations similar to those made for the TDC solution.

For a given channel, assuming no noise hit, the rate of ghost hits inside the ***W3*** window is:

Nghost3/ Channel = ***R***.W_3 = *47 kHz . 200ns*
Nghost3/Channel = 0.01
Nghost3/Chip = N_{CC}***0.01 = 0.64** for a 64-channel chip.

The number of "real" hit inside the same ***W3 window*** (assuming a 100% efficiency of each view) is the same as for the TDC solution:

Nhit3/ Channel = ***Mult*** / ***Nch*****= 4/1666=2.4e-3**
Nhit3/ Chip = N_{CC} *** 2.4e-3= 0.15**

The average digitizing rate required to convert the read analogue samples of a front-end chip is:

Ncells * F_{trig1}* (Nghost3/Chip + Nhit2/Chip) = 4 * 20E3 * (0.64+0.15) =64 kSample/s

This rate is very small for modern ADC. More probably, we will use MSample/s range ADC to decrease the size of the derandomizing mixed mode buffers of the ASIC. We can also imagine to multiplex the outputs of several Front-end chips to a single faster ADC. Simulations have still to be performed to size properly these buffers to limit the deadtime.

Assuming that a hit on a strip is encoded using ***B*** = 8 Bytes:
2 Bytes for the coarse timestamp
2 Bytes for a channel number
4 Bytes corresponding to the 4 digitized analogue samples
the digital data throughput can be calculated:

DT/Chip = B * F_{trig1}* (Nghost3/Chip+Nhit2/Chip)* =8 * 20E3*(0.64+0.15) =128 *kByte/s

DT/View **= 3.3 MByte/s**
DT/Tracker **= 19.8 MByte/s for the whole tracker**

c) Advantages and drawbacks of these solutions

Solution 3a)

Advantages:
- Low frequency common mode noise can be subtracted (baseline subtraction).
- Direct access to signal shape and amplitude.
- Good ghost rejection because of the signal shape knowledge.

Drawbacks:

- Requirement for a complex FPGA design
- No rejection of the high frequency common mode noise or parasitic signals.
- High rate between the ASIC and the FPGA:
    - Source of noise.
    - Possible bottleneck if the rate of ghost or noise increase (the margin is quite small).

Solution 3b)

Advantages:

- Low frequency common mode noise can be subtracted (baseline subtraction).
- Direct access to signal shape and amplitude.
- Good ghost hit rejection because of the signal shape knowledge.
- Low rate between ASIC and FPGA. There is some margin to increase the number of samples for better noise rejection and/or for the trigger rate.
- Relatively low digital output data flow.
- Innovative solutions. Possible reuse for other detectors.
- L1 trigger can eventually be distributed as a time stamp and not as a “real time” critical timing signal.

Drawbacks:

- Complex and innovative chip architecture.

No rejection of the high frequency common mode noise or parasitic signals.

9. Schedule and Resources

The Micromegas tracker Project, as its R&D phase is declining, reaches another step which is starting in 2009 and planned to end in 2014 with the tracker fully operational .

9.1. Schedule of the Project

	2009	**2010**	**2011**	**2012**	**2013**	**2014**
Goals	ResistR&D Tests in beam ASIC design *Drawings (interface def.)*	Resist Segmentation ASIC design DAQ proposal *Drawings + Calculations*	1 XY Detector ASIC design Slow Control	**Detector Production** **ASIC Production** *Detailed drawings* 2nd DAQ proposal Slow Control		
Steps		**PDR**	**ASIC Prod.** **FDR**		**Integration**	**Test1 Integration Test2**

9.2. Human Resources

The following table is defined in men per year:

	2009	2010	2011	2012	2013
Detectors					
Engineer	1	1 (PL)	1	1	1
		0.2 (Quality)	0.2	0.5	0.5
				0.5	0.5
Technician.	2	0.8 (Mech.)	0.8	2	2
		0.8 (Measur.)	0.8	1	1
Electronics					
Engineer	1	1	1	1	1
Technician		1	1	1.5	1.5
Design/Calculations					
Engineer	0.5	0.5	1	0.5	
Technician	0.5	0.5	0.5	1	1
Slow Control					
Engineer	0.2	0.2	0.5	0.5	1
Technician				1	2
DAQ					
Engineer		0.2	0.5	1	1
Technician					
TOTAL					
Engineer	**2.7**	**3.1**	**4.2**	**5**	**5**
Technician	**2.5**	**3.1**	**3.1**	**6.5**	**7.5**

The physicists of the Saclay/SPhN team will also contribute all along the project as they have already done during the R&D phase. 2014 being dedicated to installation finalization, tests and commissioning, the required manpower will be established later.

9.3. Expected Cost of the Project

- The tracker consists of a barrel tracker of 3x2 cylindrical layers (X and Y) of about 3 m^2 costing 60 k€ and a forward detector of 3x2 disks, 1.5 m^2, costing 30 k€.
-
- **Tracker:** **90 k€**
- **Mechanics:** **100 k€**
- **Gas system:** **40 k€**
- **Electronics connectors (30 k channels):** **60 k€**
- **Electronics (30 k channels,** 4 €/channel**):** **120 k€**
- **DAQ:** **10 k€**
- **Integration** (slow control included)**:** **120 k€**

TOTAL **540 k€ (715 k$)**

References

[1] B.A. Mecking et al., Nucl. Instrum. Methods A 503 (2003), 513

[2] CLAS12 Technical Design Report, Jefferson Lab, 2008, 101

[3] Y. Giomataris et al., Nucl. Instrum. Methods A 376 (1996), 29

[4] C. Bernet et al., Nucl. Instrum. Methods A 536 (2005), 61

[5] Y. Giomataris et al., Nucl.Instrum.Meth.A560 (2006), 405

[6] A. Delbart et al., ”Production process of a ”bulk” micromegas for the T2K-TPC”, CEA-Saclay/DAPNIA/T2K-TPC internal note EDMS6234, 12/16/2005

[7] D. Thers et al., Nucl.Instrum.Meth.A469 (2001),133

[8] R. Veenhof, http://garfield.web.cern.ch/garfield/

[9] P. Colas et al., Nucl. Instrum. Methods A 478 (2002), 215

[10] P. Baron et al., IEEE Trans.Nucl.Sci.55 (2008)1744.

[11]: S. Procureur, CLAS-note 2007-004

[12] E. Delagnes et al., IEEE Trans. Nucl. Sci.47, No. 4 (2000), 1447.

[13] D. Thers PHD Thesis, Université Blaise Pascal, Clermont-Ferrand (2000).

[14] For example:
http://irfu.cea.fr/Phocea/file.php?class=cours&file=/delagne/Timing_Porquerolles_0.5.pdf

[15] M.J. French et al., Nucl. Instrum. Meth. A466 (2001) 359

[16] Ph. Abbon et al., Nucl.Instrum.Meth.A589 (2008),362.

Table index

Figure index